Development and characterization of metallo-dielectric hybrid nanomaterials

2016

Development and characterization of metallo-dielectric hybrid nanomaterials

BOSTON UNIVERSITY

GRADUATE SCHOOL OF ARTS AND SCIENCES

Dissertation

DEVELOPMENT AND CHARACTERIZATION OF METALLO-DIELECTRIC HYBRID NANOMATERIALS

by

YAN HONG

B.S., Beihang University, 2010

Submitted in partial fulfillment of the

requirements for the degree of

Doctor of Philosophy

2016

Approved by

First Reader ______________________________
Björn M Reinhard, Ph.D.
Associate Professor of Chemistry

Second Reader ______________________________
Lawrence Ziegler, Ph.D.
Professor of Chemistry

ACKNOWLEDGMENTS

I will attribute the greatest thanks to my academic advisor, Björn M Reinhard, who has been always supporting and helpful within my PhD research. He is a wise mentor, as well as a friend with comprehensive knowledge and appealing enthusiasm over science. It is of pleasure to be his student exploring the realm of unknown and surprise. Also I will thank my DAC members, Professor Lawrence Ziegler, Professor John Straub, Professor Shyamsunder Erramilli, and Professor Keith Brown. Their patient guidance to my academic career is sincerely appreciated.

For my love Tan Li, I am always grateful for her warm and comforting effort over our long distance relationship. I'm so lucky to have her companion with my soul during my PhD study. My parents are supportive as they always were. They told me they are proud of their son being devoted to scientific research. And I'm proud to be their son.

My dear friends, colleagues and labmates, please take my sincere gratitude for all of you. You helped in many ways dealing with obstacles in research and life. I do believe the pursuit of science is equivalent to the pursuit of happiness. Science is cruel sometimes. While you, my fellows, are constantly bringing happiness to me. You deserve the special acknowledgement in this dissertation.

DEVELOPMENT AND CHARACTERIZATION OF METALLO-DIELECTRIC HYBRID NANOMATERIALS

Yan Hong

Boston University Graduate School of Arts and Sciences, 2016

Major Professor: Björn M Reinhard, Associate Professor of Chemistry

ABSTRACT

The rational combination of dielectric and metallic nano particles brings novel optical properties to conventional subwavelength structures. This thesis introduces the optoplasmonic geometries demonstrating versatile ability in both far and near field modification within nano scale. Template-assisted self-assembly approaches are applied creating nano entities with titanium dioxide and gold nano spheres. A top-bottom mono hybrid unit and interdigitated array are developed. With the examination of the elastic and inelastic response of these hybrid materials, physical models are simulated to depict the scenario of varied geometry and combination of nano particles. In contrast to solely metal or dielectric particle arrays, this type of artificial material not only enhances the near electric field intensity within the metal nano cluster hot spots, but also expands the overall volume of enhanced electric field. Further study reveals that the additional enhancement and redistribution of near field are derived from the coupling between the nano gold cluster plasmon resonance and the in-plane diffractive mode of the dielectric array. The redirected emission profile of the fluorescent dyes within the hybrid array is explored.

TABLE OF CONTENTS

LIST OF FIGURES

LIST OF ABBREVIATIONS

BU	Boston University
DF	Dark Field
E-field	Electric Field
ELISA	Enzyme-Linked Immunosorbent assay
ELISpot	Enzyme-Linked ImmunoSpot
FDTD	Finite-Difference Time Domain
ISO	International Standards Organization
NCA	Nano Cluster Array
NP	Nano Particle
PCR	Polymerase Chain Reaction
PMMA	Poly(methyl methacrylate)
SLR	Surface Lattice Resonance
SPP	Surface Plasmon Polariton

CHAPTER 1 INTRODUCTION

1.1 Noble metal nano particle materials

Noble metal particles with subwavelength dimensions sustain collective oscillations of conduction electrons that are known as localized surface plasmonic resonances. This terminology is similar to the concept of the 'surface plasmon polariton'(SPP), which is a two-dimensional electromagnetic wave propagating at the flat interface between a conductor and a dielectric.[1] However, the electron oscillations in metal nanoparticles are 'localized' instead of propagating.

If we start with the optical properties of metal, the physical model can be approximately described by the classic Drude model, which gives the dielectric function of the metal as:

$$\varepsilon_{Drude} = 1 - \frac{\omega_p^2}{\omega^2 + i\gamma\omega}$$

Where ω is the angular frequency of the excitation source, γ is the electron collision frequency in the bulk, and ω_p is the bulk plasma frequency of the free electrons that is determined by the density of free electrons n in the metal and the effective mass m_e of the electrons as:

$$\omega_p = \sqrt{\frac{ne^2}{\varepsilon_0 m_e}}$$

Based on this model, we can derive more practical system by taking real metal properties into account. For noble metal, bound electrons will contribute to the dielectric function in high frequency region due to inter-band transitions. A term ε_∞ is added to the Drude model formula giving a more accurate description of the dielectric function of a metal:

$$\varepsilon = \varepsilon_\infty - \frac{\omega_p^2}{\omega^2 + i\gamma\omega}$$

When illuminated by external light, the oscillation of conduction electrons will be confined to metal nanoparticles, from which the ‘localized’ surface plasmon derive. Because of the tiny size (< 100 nm) of nanoparticle compared with excitation wavelength, the oscillation is predominantly dipolar. The Clausius-Mossotti relation provides then the dipolar polarizability α as:

$$\alpha = (1+\kappa)\varepsilon_0 V \frac{(\varepsilon - \varepsilon_m)}{(\varepsilon + \kappa\varepsilon_m)}$$

Where V is the volume of the nanoparticle and ε_m is the medium dielectric constant. κ is a shape factor that is subject the geometry of the surface. For spheres, $\kappa = 2$, which means α will reach a maximum when $\varepsilon = -2\,\varepsilon_m$. In dielectric media ε_m is a positive constant. Importantly, noble metal nanoparticles such as gold or silver ones, have a negative real part of dielectric constant $\varepsilon(\omega) = \varepsilon_1(\omega) + i\varepsilon_2(\omega)$ in the visible spectrum region and, therefore, satisfy the polarizability resonance condition. This resonance is the intrinsic source for the unique optical and near-field behavior of noble metal nanoparticles.

For optical properties, Mie theory resolves the solution for the scattering cross section of a spherical particle:

$$\sigma_{scat} = \frac{32\pi^4 \epsilon_m^2 V^2}{\lambda^4} \frac{(\varepsilon_1 - \varepsilon_m)^2 + (\varepsilon_2)^2}{(\varepsilon_1 + 2\varepsilon_m)^2 + (\varepsilon_2)^2}$$

Where λ is wavelength of light.[1-2] This formula offers an expression that the scattering resonance depends on frequency of incident and the size of particle.

Important for near field properties, the surface plasmon resonance can enhance the incident electric field intensity E_0 and induce strong electric field intensities on the surface of nanoparticles. The dipolar limit gives the surface electric field of a metal nanoparticle as:[3]

$$E_{surface} = \frac{(1+\kappa)\varepsilon_m}{(\varepsilon + \kappa\varepsilon_m)} E_0$$

Thus a drastically increased near field intensity will occur at the resonance condition $\varepsilon = -\kappa\varepsilon_m$.

However, individual metal nanoparticle suffers from ohmic loss due to electron damping, which contributes to the imaginary part of dielectric function. Especially when nano particle size increases, the non-radiative loss, also known as absorption of the particle, will reduce the radiative performance and generate heat.[4-5]

Metal nano particle with varied shapes were synthesized and investigated demonstrating promising potential application. Additional features, such as multiple resonance modes, anisotropic scattering and escalated near electric field enhancement were introduced to conventional plasmonic units. [6-9]

If we scale the vision up by thinking of plasmonic complexes with multiple numbers of nanoparticles (so called plasmonic molecules), the subject will be even more sophisticated and interesting. Starting with a plasmonic dimer, discrete dipole approximation and coupled dipole approximation were made to approach a reliable model of plasmonic dimer.[10] A basic model was built to view the dimer plasmon as bonding and antibonding linear combinations of individual nanosphere plasmons.[11]

Subsequent studies investigated their near and far field behavior as a function of the nanoparticle separation [3, 12] or shape of the units that compose the dimer.[13-14]

Instead of manipulating the geometry of individual plasmonic components, assembling nanoparticles into clusters and arrays brings more degrees of freedom in constructing functional nano devices. A group of intriguing features are introduced by applying designed combination of plasmonic components.

Researchers are now able to utilize various types of materials to build up structures with intricate and varied geometries. The coupling between two close-packed plasmonic units sustains strong red shift of localized surface plasmon resonance.[15] In comparison of individual particle, the plasmonic clusters enables tuning the frequency of plasmonic resonance in a much broader range in spectrum without additional dissipative loss in the lower energy side.[14, 16] These features enable the engineering on plasmonic clusters for multiple applications.

Plasmonic units can act as dipole antenna with tunable resonances, resulting in far- and near-field properties manipulated simultaneously. The interaction through near or far field within clusters or arrays of these particles generates far field scattering with unique behaviors that cannot be observed in conventional plasmonic particles. For example, by engineering the phase shift within the gold-silver nano antenna, an energy dependent photon-sorting is achieved resulting in color routing.[17] Nano devices that gear the polarization,[18] photon absorption[19] have been fabricated.

Due to the surface charge distribution in cavities within plasmonic clusters, areas of with local high electric field strengths , also known as ‘hot spot’, can be created.[20] A dramatic enhancement of local electric field is observed in the proximity of the nano metal particle dimer can reach a magnitude of 10^4. Furthermore, clusters made of multiple number of metal nano particles will create more hot spots and even high degree of electric field enhancement. Such phenomenon is now widely utilized [21-23] because of its great potential in molecular sensing via either refractive index[24-25] or surface enhanced Raman spectroscopy.[26-28]

A system comprising both a plasmonic antenna and a quantum emitter is commonly referred to as a superemitter, which demonstrates boosted radiative rates compared with emitters in free space.[29] This phenomenon, the enhanced fluorescent intensity generally results from a two-step mechanism. In the first excitation step, the electric field in the gap of the plasmonic antenna is leveraged by orders of magnitude due to the enhanced E-field intensity in electromagnetic hot-spot.[30] The emission enhancement mechanism is more complex because multiple factors are involved. Except the quantum yield of the emitter, the optical radiation is governed by the local density of states of the position where the emitter exists.[31] Not only the intensity but also the directivity of the super emitter can be controlled by varying the structure of plasmonic particles. For example, nanoscale Yagi-Uda antenna can be built providing a highly directed radiation.[32] In the limit of weak coupling, Purcell factor approximately describes the maximum spontaneous radiative rate enhancement. Such factor demonstrating the influence of environmental effect on quantum emitters located in resonant cavities is known as $F= (3/(4\pi^2))(\lambda_0/n^3)(Q/V)$, where is the wavelength of the incident light, n is the refractive index, Q is the quality factor, and V is the mode volume of the cavity.

The fabrication of plasmonic particle clusters can be accomplished through bottom-up approaches by linking individual units together or by top-down approaches using for instance electron beam lithography. In the former case, polymeric linkers such as DNAs[33-35] or polyethylene glycol chains[26, 36] serve as surface functional groups, forming metal clusters in suspension. These methods are scalable and yield higher yields, but it is more challenging to obtain uniform products. Electron beam lithography and subsequent metal vapor deposition can generate clusters with deterministic geometries, but the method is intrinsically limited to two dimensions..

Another type of artificial nanoparticle construct are nanoarrays created by positioning noble metal particles at defined lattice sites. Since the nano particle within the array will interact coherently, it will perform additional geometry dependent features rather than simple gratings. One of these critical features is the narrow resonance in one or two dimensional nanoparticle arrays, where extremely sharp resonance in extinction can be observed as a result of distant coupling between plasmonic nano particles.[37-38]

The realization of nanoparticle arrays requires nano-scale resolved site-generation and homogeneous unit positioning. The most popular approach is electron beam lithography and metal evaporation as described above, which may create arrays of up to hundreds hundreds by hundreds square micrometer in area with approximately 10 nanometer resolution. Self-assembly methods offer, however, much more freedom in the selection of basic building blocks as the whole range of chemically synthesized nanoparticles are available for array integration. As long as the particles behave in Brownian motion and get uniformly functionalized with particular chemical group, they will tend to fill the array lattice sites spontaneously. Particles with varied size and shape can be anchored into binding sites via either chemical,[26, 36] electrostatic[39] or mechanical[40-42] directed routes. On the other hand, self-assembly strategy is relatively economic compared with pure top-down approaches because the spontaneous binding time are independent from the array size. A promising scheme of producing large area of particle arrays and to overcome the bottle neck of electron beam lithography is to use nano-printing technologies for binding site generation, which can be achieved by instrumental replication. For example, nano-imprinting method is able to duplicate nano arrays with any designed topological patterns down to a resolution of 10nm in a few minutes.[43-44]

1.2 Dielectric nano material

When illuminated with visible incident, single or randomly distributed dielectric nano particles with the subwavelength size follow established Rayleigh scattering mechanism. Researchers are more interested in dielectric nano structures with rational arrangement to obtain wave guiding or refractive index sensing.

A major field involving nano dielectric particle array is two or three dimensional photonics crystal, where these particles forms periodic regularly repeated dielectric function change. This periodic dielectric environment result in optical band gaps in which electromagnetic waves are forbidden irrespective of the propagation direction in such structure.[45-47]

Although microspheres and resonators are beyond ‘nano’ scale, they attracted researchers for their outstanding features especially, the high Q factor,yielding low damping of the optical resonance. One representative example is the dielectric microspheres with light trapped in exhibiting extremely sharp whispering gallery modes (WGM). In the formalism, these resonators are determined by the radius *a* of the microsphere and refractive index contrast $m=m_1/m_0$ where m1 and m0 are the refractive indices of the microsphere and the surrounding medium.

Self-assembly is an efficient technique building up photonic crystals with dielectric nano particles because conventional top-down methods cannot build sufficient periodic dielectric space practically. Spherical dielectric particles will tend to from compact hexagonal close packing (HCP) crystal via self-assembly.[48-49]

1.3 Metallic-dielectric hybrid material

Though metallic and dielectric nano structures embrace the merits as introduced in light-matter interaction, they are also hindered by their intrinsic disadvantages because of material limitation in both far and near field realm.

The former, metallic nano complex especially in polycrystalline metal particles will suffer from inherent dissipative loss because the electronic damping.[4, 50] This damping leads to photothermal effect which can be problematic when the molecule or system of interest is sensitive to temperature. Also, the local heating may cause deformation of some delicate metal geometries if their optical response is highly shape-dependent.[51] On the other hand, as an enhancing antenna for quantum emitters, low Q factors of plasmonic metal nanostructures are compensated by the Purcell effect. The emitter has dissipative losses at optical frequencies and radiative losses limit Q to $< 10^2$ in conventional plasmonic antennas.[52] Dissipative losses also limit the light guiding and storing efficiencies in pure metal plasmonic nanocircuitries.[53] Additional complications for light emission engineering in plasmonic nanocavities arise from an efficient quenching of quantum emitters in close vicinity to the metal surface through increased nonradiative and decreased radiative decay.[54]

Unlike plasmonic particles, dielectric photonic resonators, such as whispering gallery mode (WGM) resonators,[55] photonic crystals[56] and Fabry-Perot type microcavities[57] can provide high Q values without any risk of quenching quantum emitters. However, the mode volumes in these photonic systems are larger and the peak electric field intensity enhancement are much lower than in comparable plasmonic systems. Furthermore, the light trapped in microcavity resonators is confined to the interior of the resonator and interacts with the surrounding predominantly through an evanescent tail. When comparing these properties with those of the noble metal nanostructures above, it is obvious that the electromagnetic properties of photonic and plasmonic resonators are in many respects complementary. This complementarity creates a potential for performance enhancement through hybrid structures in which photonic components are used for light management and plasmonic nanoantennas for light localization.

The overall feasibility of improving the performance of plasmonic nanostructures and photonic resonators and the potential for generating new capabilities in hybrid structures has been experimentally validated in different experimental geometries.[58-64] Independent from the exact geometry, all optoplasmonic approaches share common feature, such as the large size spread between photonic resonators (> micrometer) and plasmonic nanoantennas (tens of nanometers), or the need to combine building blocks of different chemical composition, which can represent significant obstacles towards a rational realization of the materials. Attempts were made by delicate top-down technology such as focused ion beam, to generate intricate plasmonic antenna above photonic templates.[58, 65] These samples were made, however, at the cost of extremely low yield and repetitive manual operation with instruments. An alternative approach has to be developed for massive production of optoplasmonic entieis. Template guided self-assembly strategies have demonstrated great promise for combining metallic and dielectric components into intricate morphologies[16, 66-68] and are, therefore, of significant interest for implementing diverse optoplasmonic geometries. This strategy allows fabrication of metallic-dielectric hybrid array to a significantly expanded scale of micrometer and even milimeter. It overcomes the area yield limit of current top down methods and makes the throughput threshold to be the duplication of templates instead of the positioning of the components.

1.4 Computational methods

Maxwell-Garnett partly explained the scattering effect of small metal particles in 1904 and 1906[69] followed by Mie who quantitatively describe the size dependent optical properties of nanoparticles for the first time in 1908.[70] However, the scientists could hardly move forward into varied shapes of nanoparticles other than spheres due to the limited numerical method and computational cost.

After the reinforcement from electronic computer, people are able to develop multiple computational methods via either analytical or numerical modelling which may excellently reproduce experimental results, especially in recent decades. For example, Purcell and Pennypacker used discrete dipole approximation (DDA), also known as coupled-dipole method (CDA) to simulate more complex systems in nano particles structures by assuming that the particles can be approximately treated as group of polarizable dipolar elements.[71] This method yields solutions of the electromagnetic field subject to an incident electric field in the frequency domain. The polarization of each element is the result of the synergetic interaction with the local electromagnetic field generated by other elements plus the external field.[72] One other example is boundary element method (BEM). The electromagnetic field inside each homogeneous region in a composite material is unambiguously determined by the fields and their derivatives at the boundary of that region, or by a distribution of charges and currents on the boundary. In BEM method, the electromagnetic field scattered by the nanoparticle is expressed in terms of boundary charges and currents. This system is then solved by discretizing the integrals using a set of N representative points distributed at the boundaries. Finally a set of linear algebra techniques will be applied to numerically solve the linear equations.[73] In contrast to BEM and DDA method, the finite difference in the time domain method (FDTD) simulates the propagation of the electromagnetic field defined on a spatial grid through consecutive steps, so the method yields E(r,t) in a direct way.[72, 74] Being a direct time and space solution, it is able to solve the Maxwell equation in complex geometries. The subject including the surrounding medium is treated as grids and the corresponding E-field and H-field functions can be calculated via finite difference method based on Maxwell equation. In 1966, Yee explained the numerical solution using FDTD with boundary conditions appropriate for a perfectly conducting surface where the tangential components of the electric field vanish.[75] In regards to computational cost, FDTD requires a relatively larger parametrization volume which include a region covering both the subject and surrounding environment. On the other hand, the computational demand of FDTD grows only linearly with the number of parametrization points.[72]

One more computational method mentioned in this thesis is multi-sphere T-matrix (MSTM) method which is for calculating the extinction, absorption, and scattering cross sections of clusters of neighboring spheres for both fixed and random orientations. The MSTM employs the superposition formulation for radiative interactions among spheres, in which the total field from the cluster is expressed as a superposition of vector spherical harmonic expansions about each of the spheres in the cluster.[76] The field will be expressed as $E_s = \sum_i^{N_s} E_s^i$, where N_s denotes the number of spheres in the cluster. The vector spherical harmonic expansion of each individual scattered field is written about the sphere origin as $E_s^i = \sum_{n=1}^{\infty} \sum_{m=-n}^{n} [a_{mn}^i N_{mn}^{(3)}(kr^i, \theta^i, \phi^i) + b_{mn}^i M_{mn}^{(3)}(kr^i, \theta^i, \phi^i)]$, where k=2π/λ is the wave number of the incident radiation having wavelength λ, a_{mn}^i and b_{mn}^i are expansion coefficients, and $N_{mn}^{(3)}$ and $M_{mn}^{(3)}$ are vector harmonis.[77] In order to solve a_{mn}^i and b_{mn}^i , a transition matrix T of the cluster of spheres represents the individual scattered fields from each sphere in the cluster, which can be used in formulating the orientation-averaged cross sections of the cluster.[78] The method also allows calculation of the random-orientation scattering properties of a cluster in a fraction of the time required for numerical quadrature.

CHAPTER 2 Self-ASSEMBLED OPTOPLASMONIC CLUSTERS

2.1 Optoplasmonic cluster

2.1.1 Design and simulation

The assembly of atoms into molecules and supramolecular entities generates materials with new physical and chemical properties. A similar gain in functionality results from the arrangement of metal or dielectric nanoparticles (NPs) into deterministic assemblies or arrays with defined morphologies. Although photonic and plasmonic components have been shown to interact synergistically in hybrid photonic-plasmonic crystals,[58, 79-84]they are extended systems and, as such, not suitable as building blocks for nanoscale plasmonic circuitries that can bridge the size gap between electronic and photonic devices.[85] Discrete optoplasmonic atoms and molecules that contain a limited number of metallic and dielectric elements in defined geometric arrangements are more compact hybrid metallo-dielectric systems.[66] Previous work by Reinhard group[66, 86-87] and others[59, 88-90] has shown that the localization of noble metal NPs in the evanescent field of whispering gallery mode (WGM) resonators, facilitates a mode coupling between the plasmonic and photonic resonances, and thus achieves a reshaping of the subwavelength field landscape surrounding the hybrid structures.[86-88] WGM resonators have, however, typical dimensions of a few to tens of μms and are, therefore, still too large as building blocks of subwavelength plasmonic circuits.

In this chapter we develop a rational fabrication approach for optoplasmonic clusters with truly subdiffraction limit dimensions and demonstrate their ability to harness electromagnetic interactions between the building blocks. We will demonstrate that discrete hybrid clusters of defined geometry represent a viable approach not only to increase the enhancement of the electric (E-) field in the hot-spots located between the metallic NPs but also in the surrounding ambient medium. Furthermore, we will demonstrate that optical vortices sustained by the complex phase landscape in hybrid metallo-dielectric clusters facilitate a significant enhancement and redistribution of the magnetic (H-) field.

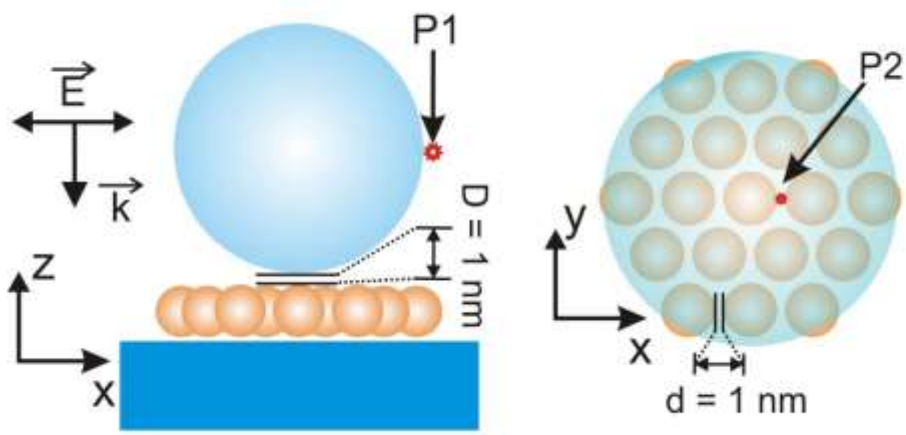

Figure 2.1. Geometry of Au-TiO2 metallo-dielectric hybrid clusters.

A. Side- and top-view of a hybrid cluster comprising a 245 nm diameter TiO2 NP on top of a 330 nm diameter plasmonic cluster assembled from 65 nm diameter Au NPs.

A schematic model of the investigated clusters is shown in Figure 2.1. The metallo-dielectric hybrid structures contain a ~330 nm diameter cluster of strongly coupled Au NPs (average diameter 65 nm ± 5 nm) supporting a high refractive index (n_r = 2.70) TiO_2 dielectric NP (average diameter 245±15nm). Although the chosen TiO_2 NPs have an average diameter of 245±15nm and are too small to exhibit pronounced WGM resonances, they still sustain electromagnetic volume modes. Furthermore, the near-fields associated with individual localized surface plasmon (LSP) modes in the metal NPs induce “image” charges in the dielectric NPs which can enhance the amplitude of the charge density oscillations in the metal NPs and facilitate the intraparticle hybridization of LSP modes with different angular momenta. We quantified the effect of the synergistic TiO_2-Au NP interactions on the E- and H-field intensity distribution in hybrid clusters using three-dimensional electromagnetic finite-difference time-domain (FDTD) simulations.

All FDTD simulations were performed using the Lumerical program package.[91] The data from Johnson and Christy[92] was used for the dielectric function of Au, whereas for TiO_2 and glass constant refractive indices of $n_r = 2.70$ and $n_r = 1.52$ were applied. In the simulations of the near-field maps and spectra of individual (opto)plasmonic clusters, the structures were illuminated from the superstratum with a linearly x-polarized plane wave propagating along the z-axis (as indicated in Figure 2). A mesh size of 0.5 nm was used in all three dimensions, and the perfect matching layer (PML) boundary conditions was applied.

The simulations were performed for a plane wave illumination with the polarization along the x-axis (see Figure 2.1) since this excitation geometry closely corresponds to the epi-illumination applied in the experimental surface enhanced Raman spectroscopy (SERS) studies described below.

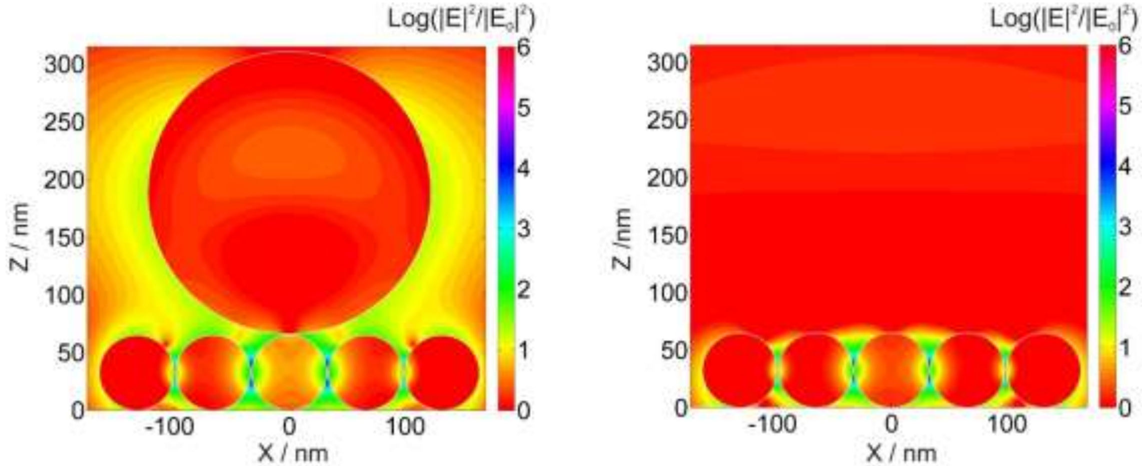

Figure 2.2. FDTD simulated E-field in the x-z plane of the hybrid and Au NP cluster

FDTD simulated E-field in the x-z plane of the hybrid (left) and Au NP (right) cluster at the incident wavelength of λmax = 797 nm, corresponding to the peak E-field intensity in the hybrid cluster.

In Figure 2.2 we compare the E-field intensity distributions in the x-z cross-sectional planes of the metallo-dielectric hybrid (top panel) and Au NP (bottom panel) cluster at the wavelength of peak E-field intensity enhancement (λ_{max} = 797 nm). In the absence of the TiO_2 NP, the E-field intensity enhancement is exclusively located in the junctions between the Au NPs. Upon addition of the TiO_2 NP, the increased E-field intensity surrounding the TiO_2 NP results in a more homogenous field distribution around the entire hybrid cluster.

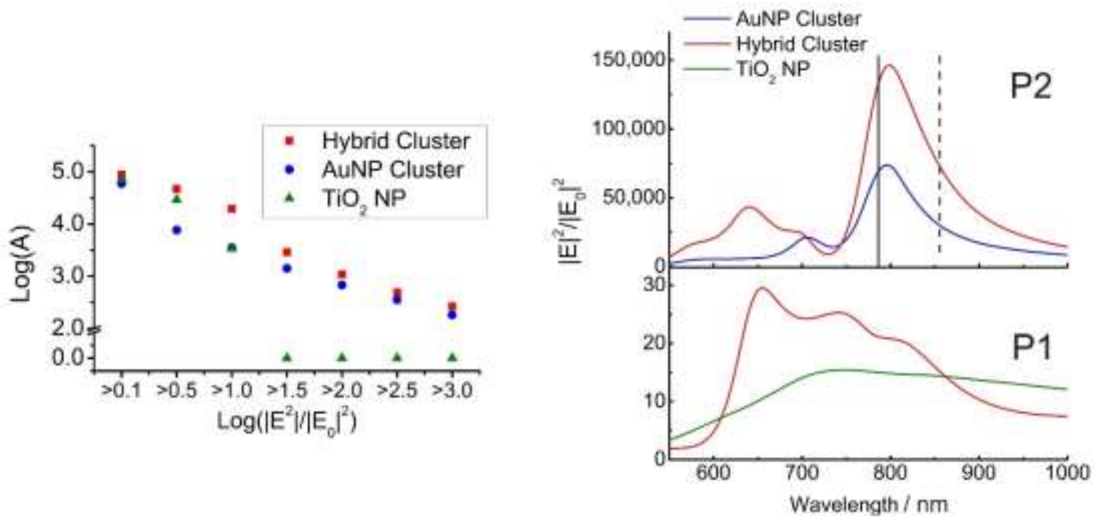

Figure 2.3. E-field intensity $|E|^2/|E_0|^2$ analysis

E-field intensity $|E|^2/|E_0|^2$ enhanced area (A) in the x-z plane of the investigated clusters (left) and comparison of the E-field intensities at the marked locations P1 (1 nm away from TiO_2 NP surface) and P2 (center gap position in equatorial plane of the metal cluster) of the hybrid (red) and Au NP (blue) cluster (right). The spectral position of the 785 nm laser (solid) and corresponding 1077 cm^{-1} Raman band (dashed) are marked with vertical lines.

In the left panel of Figure 2.3 we plot the relative areas in the x-z plane with E-field intensity enhancements above defined threshold values between $10^{0.1}$ and 10^3. The E-field enhanced area is largest for the hybrid system across the entire monitored range. In Figure 2.3 we evaluate the E-field spectrum at two specific locations marked as P1 and P2 in Figure 2.1 in the presence and absence of the TiO_2 NP. The near-field intensities at both P1 and P2 are enhanced in the hybrid system, further confirming that the E-field is enhanced both in the equatorial plane of the TiO_2 NP as well as in the plane of the Au NP cluster.

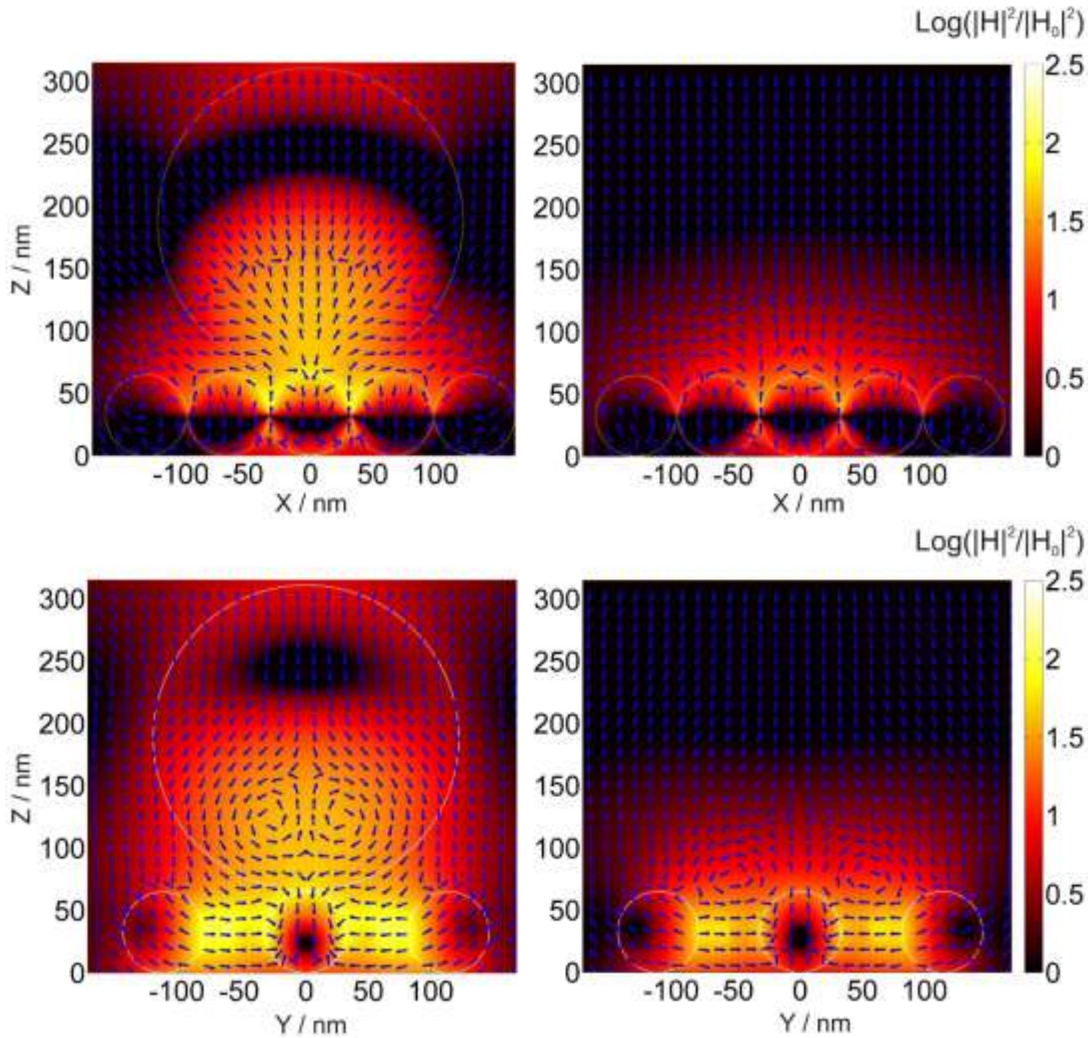

Figure 2.4. Magnetic field distribution

Magnetic field distribution of hybrid (left) and Au NP (right) clusters in x-z plane (top) and y-z plane (bottom), respectively. Normalized Poynting vectors are displayed in blue arrows.

In the next step we evaluated the influence of the dielectric NP on the H-field at λ_{max} = 797 nm. In Figure 2.4 we plot the H-field intensity map in the x-z (top panel) and y-z (bottom panel) plane for both hybrid (left) and metal NP clusters (right). The presence of the TiO_2 NP leads to an increase in the peak H-field intensity and a dramatic redistribution of the H-field into the dielectric NP. The plots also include the Poynting vector ($\mathbf{S} = 1/2\ \mathrm{Re}[\mathbf{E} \times \mathbf{H}^*]$) map to illustrate the optical powerflow in the respective structures. These powerflow maps shows that the H-field intensity within the TiO_2 NP results from the formation of optical vortices (indicated by the circulating nanoscale optical powerflow) in the y-z plane of the TiO_2 NP. Optical vortices arise from stationary phase singularities in the electromagnetic field,[36] and one important advantage of metallo-dielectric systems is that they allow for more complex phase landscapes than conventional plasmonic clusters.[26, 37] In the hybrid clusters under investigation the optical vortices in the dielectric NP generate an efficient enhancement of the magnetic field over a large fraction of the entire structure. The ability to increase the electromagnetic field intensity enhancements in the plane of the Au NPs and its surrounding through addition of the dielectric NP makes metallo-dielectric hybrid clusters interesting materials for a broad range of applications ranging from photovoltaics to biosensing.

2.1.2 Fabrication

The realization of any of these applications requires, however, rational fabrication approaches for these materials. Our approach for their experimental realization is outlined in Figure 2.5. First, NP binding sites with an average diameter of 330 nm are created in a 180 nm thick layer of poly(methyl methacrylate) (PMMA) on a glass substrate using a top-down fabrication method, such as electron-beam lithography (EBL). Meanwhile, Au NPs (British Biocell International, BBI) with an average diameter of 65 nm $\pm$ 5 nm were functionalized with a brush of thiol-EG_7-propionat (EG = ethyleneglycol). The zeta-potential of the NPs was determined as ξ = -51.9 mV. In a second fabrication step, the created binding sites are then positively functionalized with poly-L-lysine (molecular weight 15-30 kDa) to facilitate the assembly of negatively charged colloidal Au NPs into closely packed clusters on the binding sites. TiO_2 NPs are subsequently deposited onto the preassembled clusters using a convective self-assembly approach. 25 mL of a suspension containing 5×10^{11} NPs/mL of spherical, carboxylic-acid functionalized 245 nm $\pm$ 15 nm diameter amorphous TiO_2 NPs (Corpuscular Inc.) were flushed over the patterned substrate containing the NP clusters (mounted at an angle of $\theta = 40^\circ$) at a rate of 10 ml/hour using a syringe pump. The wells created in the photoresist serve as traps for the TiO_2 NPs and facilitate their convenient positioning on top of the self-assembled Au NP clusters at the bottom of the wells. Finally, the PMMA was removed through lift-off in 1-methyl-2-pyrrolidinone, releasing the assembled optoplasmonic nanoclusters.

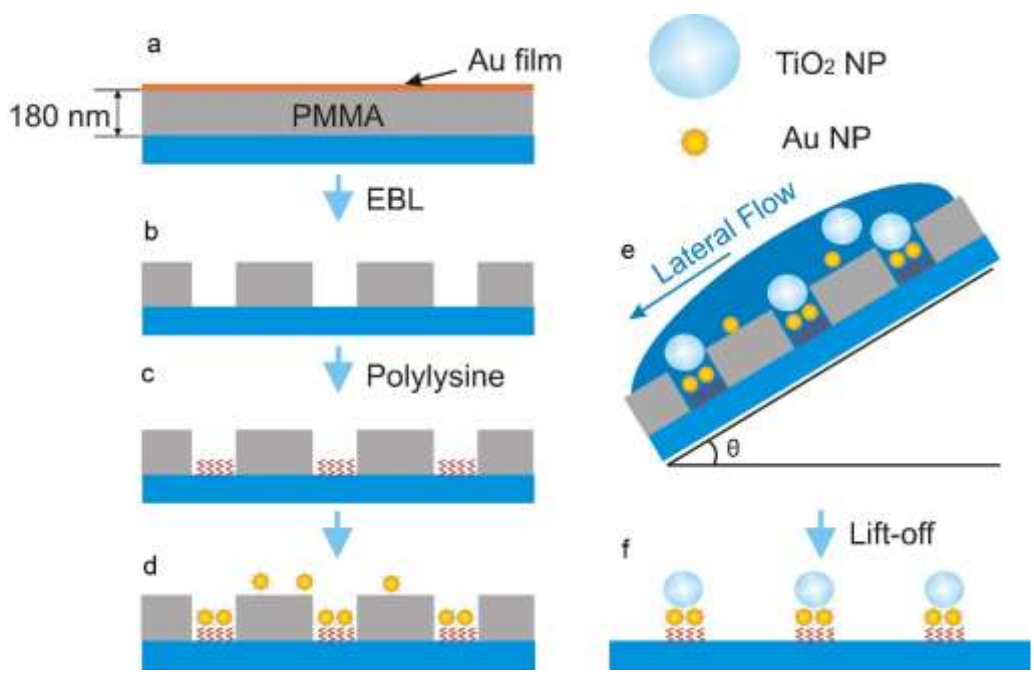

Figure 2.5. Template guided self-assembly of optoplasmonic nanoparticle clusters.

a). Spincoated PMMA (180 nm) film on a quartz substrate containing a thin (10 nm) sputtered Au layer. b). Patterned PMMA mask after electron beam lithography (EBL), etching, and development. c). Polylysine is bound to the exposed binding sites on the substrate. d). Au NP clusters are self-assembled on the polylysine functionalized binding sites. e). Convective assembly of TiO2 NPs on pre-assembled Au NP clusters. The convective assembly is facilitated by tilting the substrate by a fixed angle, θ = 40˚. f). The PMMA matrix is released in a final lift-off, releasing the optoplasmonic clusters.

2.1.3 Characterization

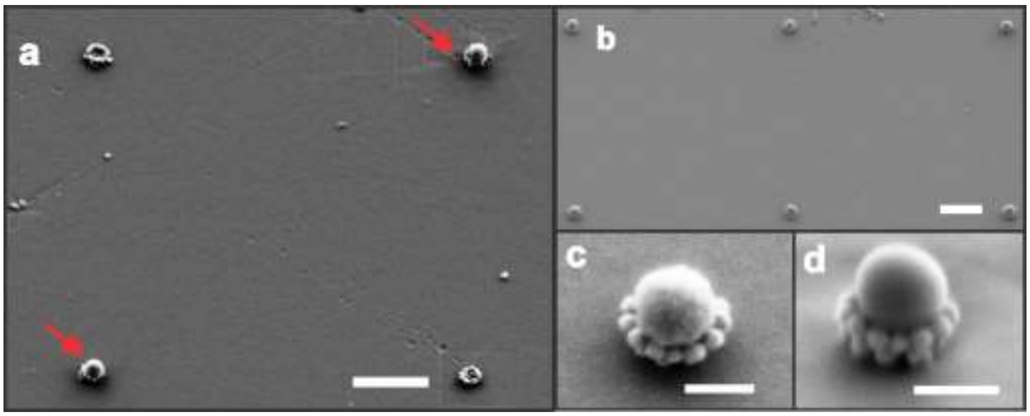

Figure 2.6. SEM images of optoplasmonic nanoparticle clusters.

SEM images of metallo-dielectric clusters. a). Self-assembled array containing metallo-dielectric clusters (marked by arrows) and pure plasmonic Au NP clusters. Scale bar is 1 µm. b). Larger section of a Au-TiO_2 hybrid cluster array. Scale bar is 1 µm. c). and d). Magnified side-views of optoplasmonic clusters. Scale bars are 200nm.(a, b & c 30˚ tilted. d. 60˚ tilted)

Figure 2.6a shows a SEM image of a section of an array that contains both complete hybrid clusters and conventional Au NP clusters. The arrows in Figure 3a mark complete hybrid clusters whereas the nanostructures in the top left and bottom right corner show examples of the self-assembled Au NP cluster base. Figure 2.6b shows a larger area of the array containing complete hybrid clusters and Figures 2.6c & d contain side-views (tilt angles 30˚- 60˚) of individual hybrid clusters at larger magnification. Despite inevitable differences in the geometries of the experimentally assembled hybrid cluster and the simplified model underlying the performed simulations, the FDTD calculations are still in good agreement with the measured elastic scattering spectrum of the self-assembled clusters.

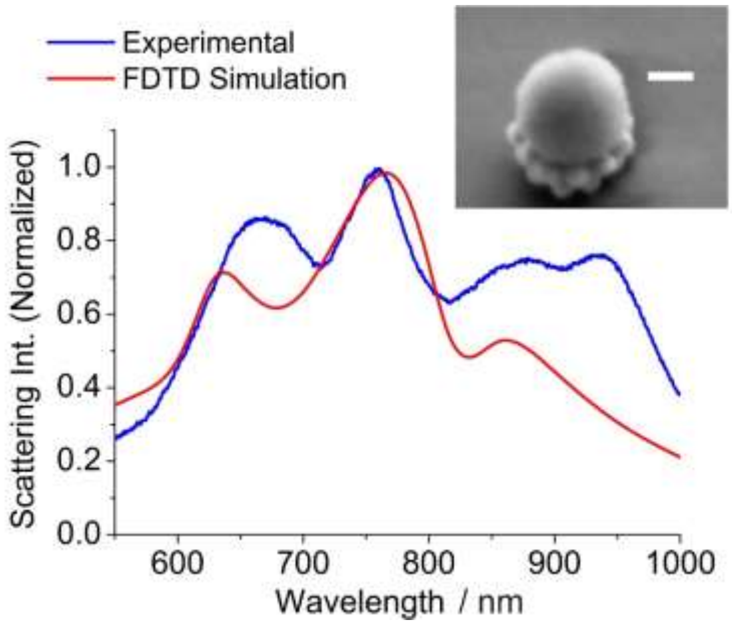

Figure 2.7. Elastic scattering spectra of self-assembled Au-TiO_2 hybrid clusters.

Experimental (blue) and FDTD simulated (red) scattering spectrum for a metallo-dielectric hybrid cluster. The SEM image of the investigated cluster is included in the inset (scale bar is 100 nm). The simulated spectrum refers to the geometry shown in Figure 2.1.

Figure 2.7 contains the darkfield scattering spectrum for the optoplasmonic cluster shown in the inset acquired with light that was linearly polarized in the substrate plane and the simulated forward scattering spectrum for the model system in Figure 2.1. Scattering spectra were acquired in an upright microscope connected to an imaging spectrometer with a 40x air objective (NA = 0.65) under oblique illumination from a 100 W tungsten halogen lamp through a high numerical aperture (NA) oil darkfield condenser (NA = 1.2 – 1.4). To control the polarization of the incident light in the sample plane, we applied the approach introduced by Knight *et al.* and illuminated the darkfield condensor with linearly polarized light through a pinhole. The acquired scattering spectra were backgroud subtracted and corrected for the excitation profile of the tungsten lamp.

The FDTD simulations reproduce the overall shape of the experimentally acquired spectrum, except for the shoulder at 935 nm. The good correspondence of the measured and simulated far-field spectrum confirms that the applied theory adequately describes the electromagnetic interactions in the hybrid system.

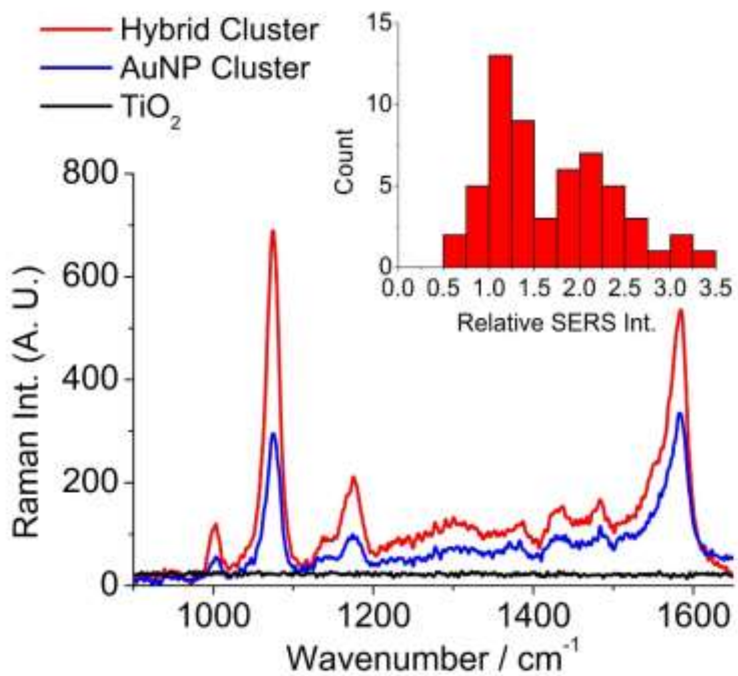

Figure 2.8. Raman spectra of self-assembled Au-TiO_2 hybrid clusters.

Au NP cluster, and TiO_2 NP. The inset displays the distribution of the relative Raman signal intensity (C-S stretch, 1077cm^{-1}) of discrete pairs of hybrid and Au NP clusters (57 spectra each) measured under identical conditions.

To further validate the predicted increase in the E-field intensity in the hybrid cluster (Figure 2.3), we performed SERS measurements of the small molecule para-mercaptoaniline (pMA) chemisorbed onto the structures. After O_2 plasma-cleaning the fabricated samples were incubated with a 10 mM pMA solution in ethanol for 8 hours and then rinsed with copious amounts of ethanol. SERS spectra were taken in a homebuilt Raman microscope in epi-illumination mode using a 785 nm diode laser.

Since the SERS signal enhancement of a molecule scales with the product of the E-field intensities at the pump and Raman emission wavelengths, it encode direct information about the near-field intensities at the laser pump and Raman shifted emission wavelengths (marked as vertical lines in Figure 2.3). Figure 2.8 shows representative pMA SERS spectra from individual hybrid and Au NP clusters, and TiO_2 NPs. The figure also contains the distribution of the relative intensities of the 1077 cm^{-1} C-S stretch mode in individual hybrid and adjacent Au NP clusters as inset. The intensity ratios of approximately 60 cluster pairs were evaluated. While we did not detect any Raman intensity for the TiO_2 NPs, the SERS signal intensities for the hybrid clusters are systematically higher than those of the Au NP clusters, which is consistent with an enhanced light localization and increased evanescent field volume in metallo-dielectric hybrid clusters. The broad distribution of the SERS intensity arises from the morphology dependence of the SERS signal enhancement in plasmonic and optoplasmonic clusters. We anticipate that the performance of the hybrid clusters will be further improved in the future through systematic optimization of the hybrid cluster assembly strategy and the use of structurally better defined building blocks.

2.1.4 Conclusion

In summary, we developed a versatile template assisted self-assembly strategy to integrate dielectric and metallic NPs into discrete metallo-dielectric hybrid clusters. Our combined spectroscopic and theoretical analyses of hybrid clusters comprising TiO_2 NPs located on top of Au NP clusters reveal that the hybrid approach not only creates an additional boost of the peak E-field intensity enhancement in the metallic cluster but also amplifies the E-field in the ambient area surrounding the hybrid system. Furthermore, the clusters show a high degree of flexibility in manipulating the phase landscape of the electromagnetic field and provide, therefore, unique opportunities for controlling the optical powerflow on the nanoscale. We analyzed the optical powerflow in the assembled hybrid clusters through FDTD simulations and found that optical vortices within the hybrid clusters achieve both an enhancement and dramatic redistribution of the H-field. Discrete optoplasmonic clusters represent, therefore, a novel approach to enhance the intrinsically weak magnetic field in the visible range of the electromagnetic spectrum.

2.2 Application in fluorescent enhancement

2.2.1 Design and simulation

As introduced in chapter 1, dipole emission in the vicinity of plasmonic nano particles can be drastically enhanced due to the near field 'hot spot' and spontaneous radiative rate enhancement in the tiny mode volume. On the other hand we have proved that optoplasmonic nano cluster demonstrates higher electric field enhancement magnitude and redistributed energy flow. Based on those facts, we can presume that the optoplasmonic cluster will gain both in emission intensity and directivity.

According to the simplified model in Anger's research on fluorescence enhancement and quenching of single molecule,[30] we start with depict the observed fluorescent emission rate as

$$\gamma_{em} = \gamma_{exc}\left[\frac{\gamma_r}{\gamma}\right] = \gamma_{exc}[1 - (\frac{\gamma_{nr}}{\gamma_0})/(\frac{\gamma}{\gamma_0})],$$

where γ_0 is the free space decay rate of the dipole, $\gamma_{nr} = \gamma - \gamma_r$ is the nonradiative decay rate and $\gamma_{exc} \propto |\boldsymbol{p} \cdot \boldsymbol{E}|^2$is the excitation rate depending on the local excitation field $\boldsymbol{E}(\mathbf{r}_m,\omega)$ and dipole moment $\boldsymbol{p}$. If all parameters are performed in parallel, we can tell the excitation rate ratio in optoplasmonic cluster to the case in plasmonic NP cluster will be $[\boldsymbol{E}_{opto}]^2/[\boldsymbol{E}_{plas}]^2$, where $\boldsymbol{E}_{plas}$ and $\boldsymbol{E}_{opto}$ are electric field in plasmonic NP cluster and optoplasmonic cluster, respectively.

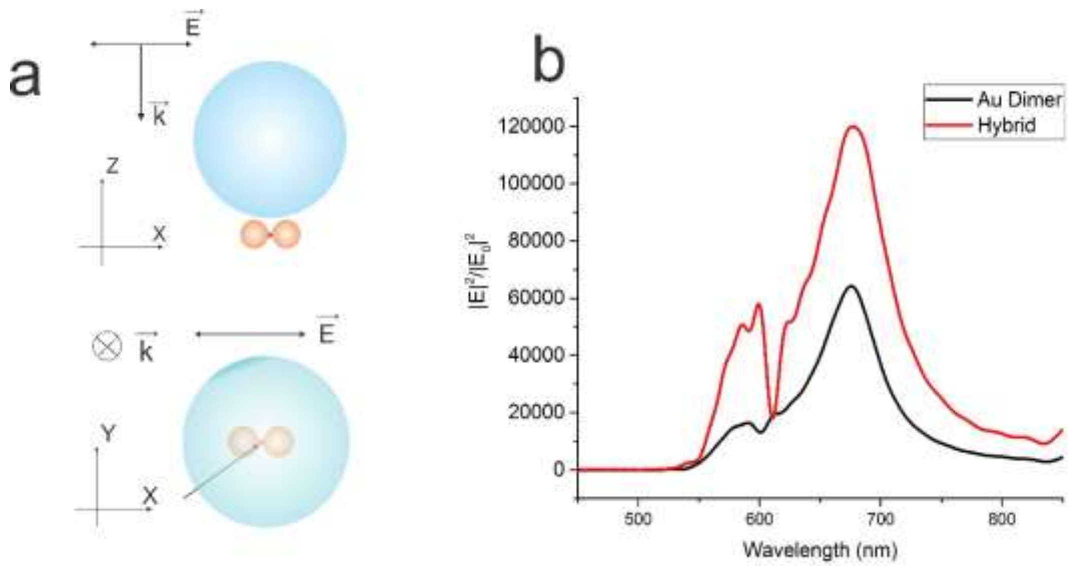

Figure 2.9. FDTD model for excitation analysis

(a) Illustration of simulation model from top view (top) and side view (bottom) showing the optoplasmonic cluster geometry and incident polarization. The TiO_2 NP and Au NP are shown in blue and yellow respectively (b) Electric field enhancement in optoplasmonic cluster and plasmonic dimer. The intensity is monitored at the position shown in red star mark in (a).

For the spontaneous decay process, we know that based on Fermi's golden rule, the spontaneous decay rate can be described as

$$\gamma = \frac{2\omega}{3\hbar\varepsilon_0} |\boldsymbol{p}|^2 \rho(r_m, \omega),$$

where ω is the transition frequency and ρ denotes the electromagnetic density of states. As a result, the ratio of radiative decay process rate of optoplasmonic cluster to plasmonic cluster will be $[\frac{\gamma_r^{opto}}{\gamma^{opto}}]/[\frac{\gamma_r^{plas}}{\gamma^{plas}}] = [1 - \frac{\gamma_{nr}^{opto}}{\gamma^{opto}}]/[1 - \frac{\gamma_{nr}^{plas}}{\gamma^{plas}}]$, where the subscription 'r', 'nr' denotes 'radiative' and 'nonradiative' respectively. Finally, we can approximately estimate the observed emission enhancement of optoplasmonic cluster compared with plasmonic cluster through simply multiplying the excitation and spontaneous decay ratios.

We built a simple model through FDTD examing the excitation and emission process in optoplasmonic clusters separately. As shown in figure 2.9a, we constructed an optoplasmonic cluster be reducing the number of gold nano particles in model in figure 2.1 from 19 to 2. The excitation field intensity enhancement spectra for optoplasmonic cluster and plasmonic cluster are shown in figure 2.9b. Obviously there's a general field enhancement of optoplasmonic cluster to a magnitude of 2 to 3. This is in consistence with the model we have in chapter 2.1.

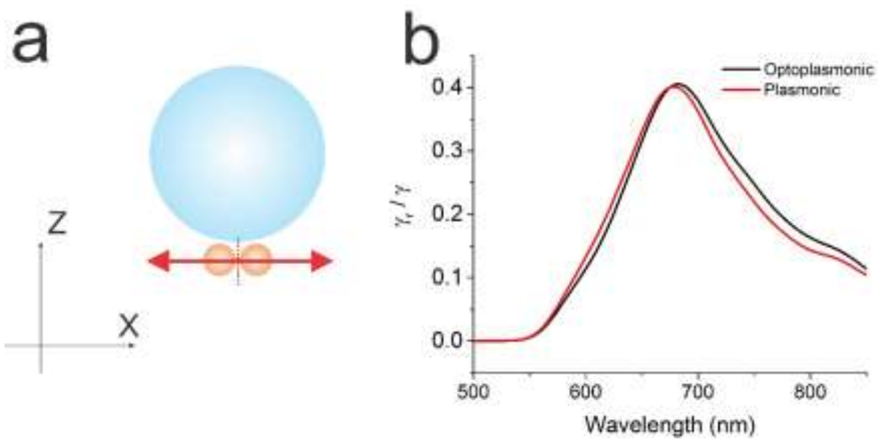

Figure 2.10. FDTD model for parallel dipole emission analysis

(a) Illustration of simulation model top view showing the optoplasmonic cluster geometry and dipole polarization. The TiO_2 NP, Au NP and dipole are shown in blue, yellow, and red arrow respectively (b) Radiative power ratio in optoplasmonic cluster and plasmonic dimer.

Then we tried to monitor the radiative decay rate by removing the plane wave incident in figure 2.1a and place a dipole emitter in the gap of gold dimer (figure 2.10a). In this model, if we only consider the case when the dipole oscillates parallel to the dimer axis, the ratio $[\frac{\gamma_r^{opto}}{\gamma^{opto}}]/\left[\frac{\gamma_r^{plas}}{\gamma^{plas}}\right]$ is almost 1 because the impact of additional TiO_2 NP to local density of states in the dimer gap is almost 0 (figure 2.10b). This is because of almost identical density of states in optoplamonic and plasmonic cluster.

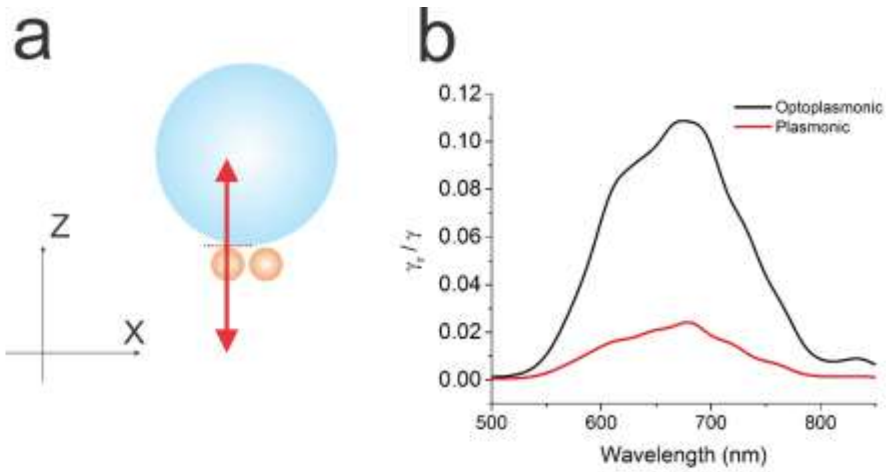

Figure 2.11. FDTD model for vertical dipole emission analysis

(a) Illustration of simulation model top view showing the optoplasmonic cluster geometry and dipole polarization. The TiO_2 NP, Au NP and dipole are shown in blue, yellow, and red arrow respectively (b) Radiative power ratio in optoplasmonic cluster and plasmonic dimer.

We may also consider another case in which the dipole is located at the gap between the TiO_2 NP and gold NP, as shown in figure2.11a. Although the overall radiative power ratio is reduced, in this model we obtain elevated radiative power ratio in the optoplasmonic cluster (figure 2.11b). This phenomenon is due to the raised local density of states when the emitter is brought close to a dielectric particle.

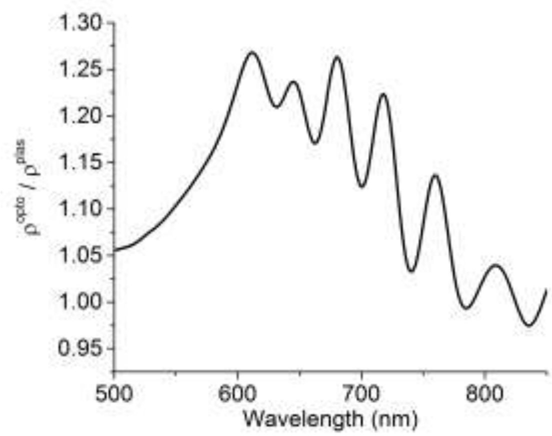

Figure 2.12. Partial local density of states ratio

Curve shows the ratio of partial local density of states in the gap of gold NP dimer in optoplasmonic cluster to the case in plasmonic clusters. The dipole orientation is shown in figure 2.11a.

Another impact from the TiO2 NP is the modification of emission directivity of the plasmonic antenna. Here we plot the radical emission diagram of plasmonic and optoplasmonic model in figure 2.10a, whose emission power is dominant compared with other dipole orientations. In figure 2.13, it is noticeable that emission direction in optoplasmonic model has preferred emission direction generally in the TiO_2 NP side. This effect can be amplified by either scaling up the size of TiO_2 NP or increasing the refractive index. This can be explained by the tendency of light travel to higher refractive index particle close to a dipole. As stressed in chapter 2.1.1, the light flow in figure 2.4 can be reversed and results in an anisotropic emission directivity.

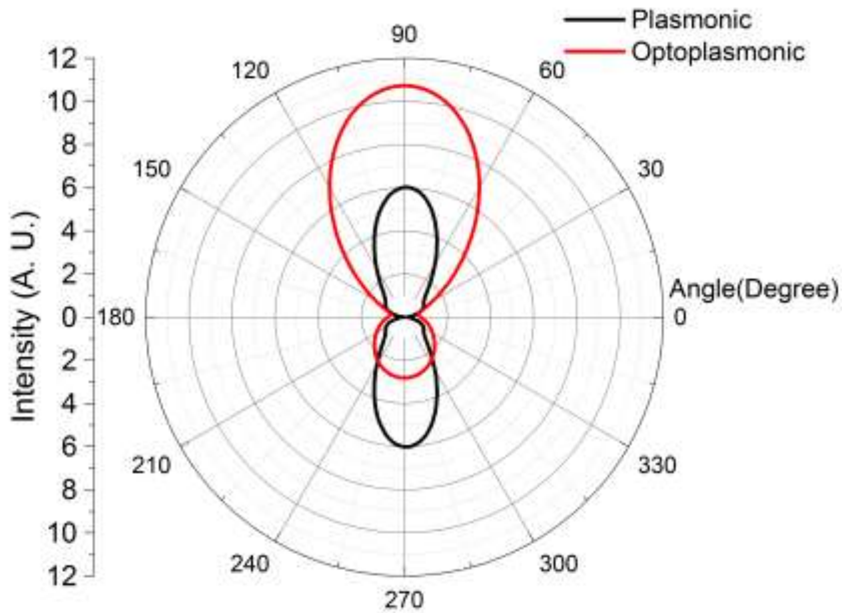

Figure 2.13. Polar diagram of emission intensity in XZ plane

Radiative emission intensity as a function of angle in XZ plane of the model in figure 2.10a. Intensity is scaled to arbitrary units.

All simulations carried out in this section was operated via Lumerical FDTD solutions. In the models, TiO_2 NP is with diameter = 250nm and treated as dielectric particle with refractive index = 2.40. Gold NP is with diameter = 60nm and with dielectric function taken from the data of Johnson and Christy. The gap between AuNPs is 2nm and the gap between AuNP and TiO_2 NP is 4nm. Radiative decay ratio is obtained by dividing the collected radiative power of the structure with input dipole power. Partial density of states is calculated by the formula $\rho_z(r_0, \omega) = \frac{6\omega}{\pi c^2}[Im(Gz(r_0, r_0, \omega))]$ where G_z is the dyadic Green's function in Z direction defined as $G_z = \frac{E_z c^2 \varepsilon_0 \varepsilon_r}{\mu \omega^2}$.

2.2.2 Fabrication

In order to validate the enhanced fluorescence signal in optoplasmonic cluster, a modified scheme from chapter 2.1.2 is conducted. For the gold NP cluster substrate part, the process is similar to the one in chapter 2.1.2, while the PMMA layer thickness is modified to ~400nm. Binding sites were created via EBL with size of 270 nm in diameter and subsequently positively charged by L-polylysine. Then the binding sites sample is incubated with gold NP colloid functionalized with negatively charge group (thiol-EG_7-propionat). After washing the excessive gold NP by DI water, samples are ready for TiO_2 NP positioning. The TiO_2 NPs are functionized with fluorescent dye through consecutive functionalization of BSA-biotin and Neutravidin-Alex647. Here a convective assembly is taken in the method described with detail in chapter 3.3.1. After the lift off of PMMA layer, the optoplasmonic cluster with fluorescent dye is obtained. The control groups were created with the same method but excluding the Au NP binding procedure, resulting in dye-conjugatedTiO_2 NP on substrate.

2.2.3 Characterization.

Since we can obtain optoplasmonic cluster with relatively high yield, we are able to observe the fluorescence performance in experiment to validate the predicted radiative emission enhancement. Samples prepared by the method described in chapter 2.2.2 were characterized by normal fluorescence imaging setup. Samples were illuminated by normal incidence which is the mercury lamp light filtered by 640/10 nm band pass filter and a 662 nm dichroic filter. The emitted fluorescence signal were filtered by a 680/20 nm band pass filter and collected by a CCD camera. The image magnification and collection were through a 60X (NA=0.65) oil objective. Samples were immersed in index matching oil for homogeneous refractive index medium. The samples with optoplasmonic cluster sites were located via dark field scattering microscopy with tungsten light illumination and then measured via the fluorescence channel.

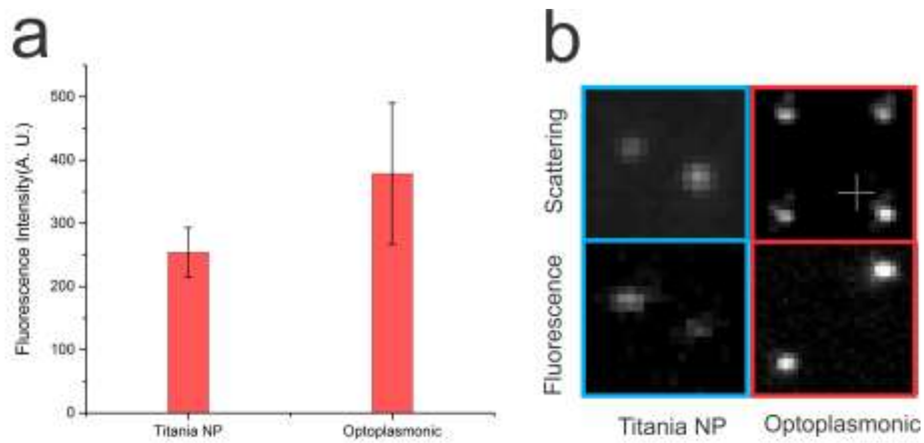

Figure 2.14. Fluorescence intensity of optoplasmonic clusters

(a)Summarized fluorescent intensity of optoplasmonic clusters and single dye-conjugated TiO_2 NP. (b) Dark-field scattering and fluorescent images of TiO_2 NP (left column) and optoplasmonic clusters (right column).

In the optoplasmonic sample, since the binding efficiency of TiO_2 NP onto Au NP cluster is controlled, the sites with significant signal under dark field image mode is either optoplasmonic cluster or Au NP cluster. The two type of cluster are distinguished with ease by comparing their fluorescence image. The optoplasmonic site could be observed both in scattering and fluorescent in the same position. On the contrary, the site visible in scattering image but absent in fluorescent image is Au NP cluster (Figure 2.14b). We summarized the fluorescent intensity of optoplasmonic cluster and Au NP cluster in figure 2.14a. Optoplasmonic cluster generally display higher fluorescent intensity than

Au NP cluster. This is in consistent with the prediction in the former chapter as result of enhanced fluorescent emission and modified emission profile.

2.2.4 Application for Interleukin (IL)-2 detection

Interleukin (IL)-2 is a 133-residue cytokine secreted by T lymphocytes after the activation by antigen or lectin. Human (IL)-2 stimulates growth of T-cell lines.[93-94] In the initial phase of the host–bacterium interaction, either the proteolytic enzymes and cytokines produced by the host's macrophages stimulate multiplication of the bacilli or the bacilli themselves trigger multiplication. Cell-mediated immunity is critical in the early stage of bacterial infection. (IL)-2 is one of the cytokines predominantly associated with cell-mediated immune responses.[95] The production (IL)-2 serves as an indicator of the patient's stage of infection. The conventional approach to monitor the concentration of (IL)-2 in serum is through ELISA, ELISpot and PCR.[96] The ELISA is the most widely used for its universality. However, the binding of the assay components relies on incubation of the solutions which is governed by the molecular diffusion. Here we introduce an alternative strategy modifying the ELISA solution-substrate interaction into particle-molecule interaction in solutions.

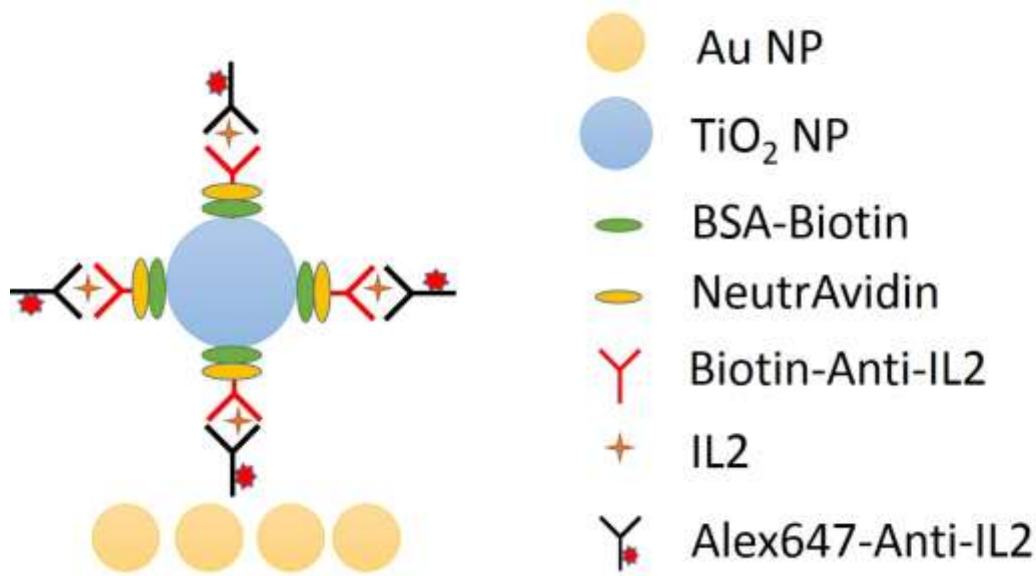

Figure 2.15. Illustration of optoplasmonic cluster assay detecting human (IL)-2

Illustrates the structure of opstoplasmonic cluster assay. Legend on the right shows that the shapes represents components of the assay. The sizes are not scaled.

As shown in figure 2.15, we developed an optoplasmonic cluster assay detecting human (IL)-2 via fluorescent imaging.

The assay is fabricated by following steps. Firstly, a substrate with Au NP cluster is obtained through exactly the same method described in chapter 2.2.2. 270 nm in diameter nano wells are formed by EBL in substrate with 400 nm thick PMMA. The substrate were incubated with 1% polylysine solution for 1 hour. 60 nm Au NP functionalized with thiol-PEG-carboxyl group were concentrated in colloid and incubated with the substrate to form the Au NP cluster. The TiO_2 NP were consecutively incubated with BSA-biotin (2% in PBS, Thermo), neutravidin (10µg/mL, Thermo) and Biotinylated anti-Human IL-2 (100 µg/mL, Thermo) with one hour incubation time for each and 3 times of PBS 1X buffer clearing between each step. Subsequently, human IL-2 with varied concentration is diluted in human serum (Sigma) as a simulated physiological environment for detection.

The antibody functionalized TiO_2 NP was then injected into the (IL)-2 serum solution with the concentration of 8.0×10^9 NPs/mL. The solution were kept in agitating for 20min. The TiO2 NPs were collected and washed through repetitive centrifuge (4000 rpm, 3min, 3 times). The last component, Alex647 conjugated (IL)-2 antibody (3.2×10^{-5} M)is prepared and incubated with the TiO2 NP(8.0×10^9 NPs/mL). Finally, the TiO2 NPs with the fluorescent dye were anchored onto the AuNP cluster through the capillary force assembly introduced in chapter 2.2.2.

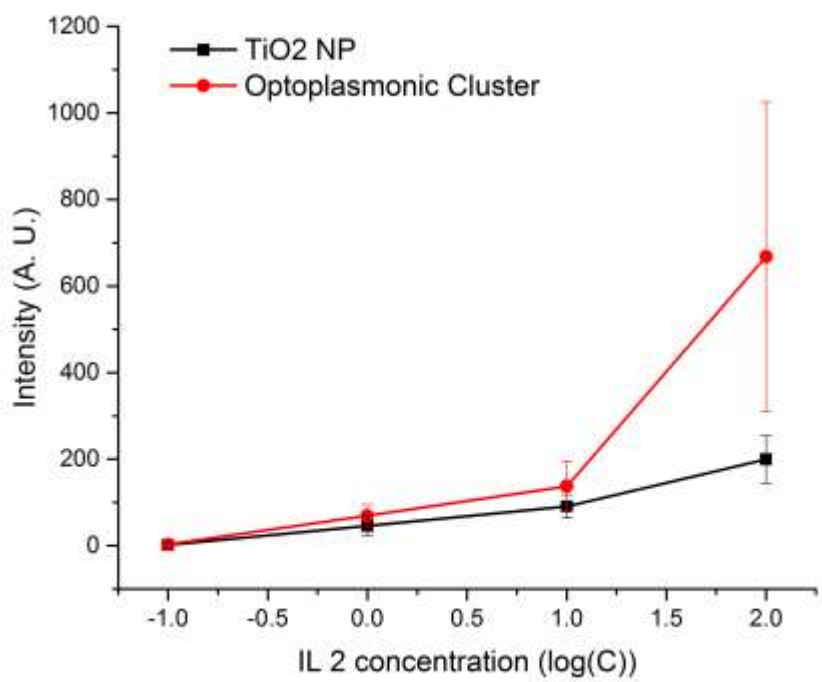

Figure 2.16. Fluorescent intensity as a function of (IL)-2 concentration

Fluorescent intensity as a function of (IL)-2 concentration C ng/mL. The X-axis is in logarithm scale.

The clusters were characterized by fluorescent imaging right after the lift off of the PMMA layer. Samples were illuminated by perpendicular incidence from the mercury lamp light filtered by 640/10 nm band pass filter and a 662 nm dichroic filter. The emitted fluorescence signal were filtered by a 680/20 nm band pass filter and collected by a CCD camera. The image magnification and collection were through a 60X (NA=0.65) oil objective. Samples were immersed in index matching oil for homogeneous refractive index medium. The samples with optoplasmonic cluster sites were located via dark field scattering microscopy with tungsten light illumination and then measured via the fluorescence channel. We collected spot fluorescent intensity both in optoplasmonic cluster and TiO_2 NP with dyes (the latter is obtained by assembling assay TiO_2 NP into pattern without AuNP cluster). As shown in figure 2.16, the optoplasmonic cluster demonstrates generally higher intensity compared with dye-conjugated TiO_2 NP. This also validates proposed enhancing and redirecting mechanism in former chapters.

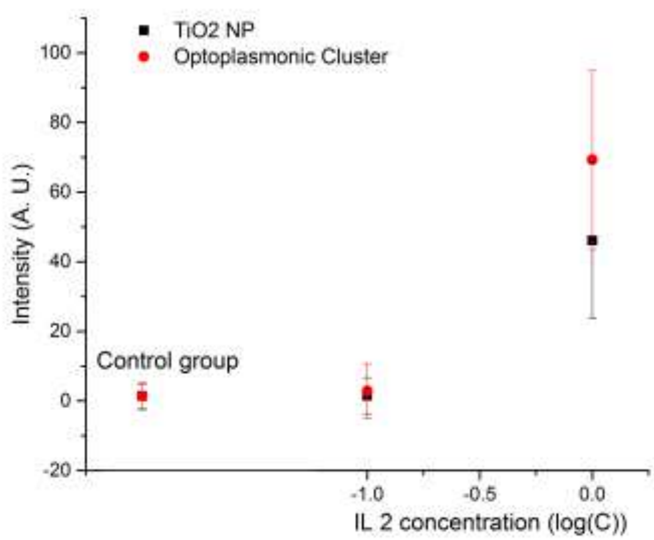

Figure 2.17. Fluorescent intensity as a function of (IL)-2 concentration compared with control group

Fluorescent intensity as a function of (IL)-2 concentration C ng/mL. The X-axis is in logarithm scale. Control group in which TiO2 NP were incubated with serum without human (IL)-2.

On the other hand, we are also able to detect human (IL)-2 in human serum with 20 minutes incubation time to a detection limit of ~1ng/mL. From figure 2.17 we can conclude that when (IL)-2 concentration is 0.1 ng/mL, its fluorescent signal level is not significant in contrast to the control group. This is not superb compared with currently specified ELISA method which can reach the level of 1 pg/mL. While we can expect improved optoplasmonic assay by optimizing TiO2 NP concentration and assembly efficiency.

2.2.5 Conclusion

We have developed optoplasmonic TiO_2 NP – AuNP nano cluster with alternative self-assembly approach. According to the FDTD simulation, the excitation rate in hybrid optoplasmonic cluster is enhanced compared with plasmonic cluster due to the enhanced light focusing by the dielectric particle above. And subsequently, the dielectric particle creates higher ratio of radiative rate because of its modification in the local density of states within the nano cluster volume. In addition, the dye emission redirected to radiate to the dielectric particle side. Finally, in fluorescent experiment, optoplasmonic clusters demonstrate higher fluorescent intensity in contrast to single dye-conjugated TiO_2 NP. The optoplasmonic cluster assay is capable of (IL)-2 detection to the limit of 1 ng/mL in physiological environment

2.3 Self-assembled NCA through nano imprinting

2.3.1 Introduction

We are consistently seeking for more efficient duplication method for nano arrays because the industrial massive production of such delicate structure is the key to its practical application of present booming nano structures.

Nanoimprinting(NIL) is a simple method to fabricate nano structures and it has attracted considerable attentions in many applications for its high resolution, high throughput and low cost of ownership.[97] Based on the material of the stamp, there are two major candidates in market. One includes hot-embossing lithography (HEL) and UV-NIL with grid quartz stamps, as known as hard nanoimprinting.[43, 98-99] The other is UV-NIL with flexible stamps, also called as soft nanoimprinting.[100]

The hard imprinting start with a stamp fabricated with E-beam lithography or photolithography. The positive features protruding out the substrate surface (usually a silicon surface) is obtained through protective mask deposition and reactive ion etching. After the mask is removed, an anti- adhesive polymer layer is deposited to the stamp to prevent the mold from stickiness of the resist. On the other hand, another substrate for pattern duplication is coated with a layer of polymer resist. The mold with feature is and the substrate with resist are then compact together with high pressure under heating and vacuum environment. Pressure as high as 600-1900 psi is necessary because the heating with the temperate above the resist’s glass temperature makes the resist soft to deform (for PMMA, the heating temperature is 140 to 180 °C). The vacuum will prevent the bubble between the mold and resist layer. After the compacting process for 5 minutes, the stamp and resist substrate is separated, leaving concave features in the resist. The residue resist in the feature bottom can be removed through a short reactive ion etching process.[43] The substrate with patterns exposed are finally created, which is equivalent the product generated by EBL.

For soft nano imprinting, a soft stamp made of polydimethylsiloxane(PDMS) is created through am opposite mother hard stamp. The soft stamp is then immersed in base material, for example 3-methacryloxypropyltrimethoxysilane (MPTS) with an imprint pressure of up to 900 mbar.[100] The compacted base is treated with UV exposure (365nm) to proceed the polymerization. The PDMS stamp is detached from the base material leaving the desired feature on substrate.

The crucial property of nanoimprinting is that the efficiency of imprinting will increase linearly with the area of the mother stamp. Once the structure is defined, the imprinting 5 minutes compacting step will be dominating in efficiency compared with EBL. In contrast, EBL is a pure top-down method and the time cost for each chip is always linearly related the area of the pattern.

In the fabrication for optoplasmonic nano structure process, the most time-consuming step is the production of substrate with nano holes. The nano imprinting process can make an alternative route for it with simpler and faster approach. Here we introduce the method developed to create the basis of optoplasmonic cluster, the nano cluster array (NCA) through hard nanoimrping.

2.3.2 Fabrication and discussion

To create the master stamp, we start with a silicon chip with patterns created by conventional EBL method. In our case, arrays of wells with 200 in diameter in varied array spacing parameters are patterned. A 30 nm thick chromium is then deposited into the wells via e-beam evaporation (figure 2.18a). The resist is then removed (figure 2.18b). A reactive ion etching process is applied to etch the whole substrate level down is applied (Ar / SF_6 25/25 sccm, 50mTorr ,200W, 30 seconds) as shown in figure 2.18c. The Cr layer is then removed by wet etchant. The protruding pillars are approximate in height of 200 nm (figure 2.18e). Finally ,the stamp is coated with a layer of anti-adhesive molecule (Heptadecafluoro-1,1,2,2-Tetrahydrodecyl-dimethylchlorosilane, Gelest, Inc.).

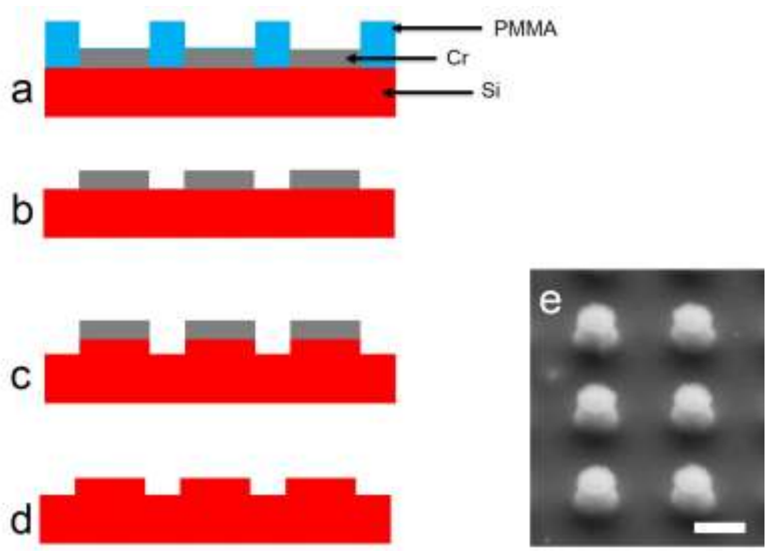

Figure 2.18. Fabrication of stamp for nanoimpring

a) Cr is deposited into wells created by EBL. b) The PMMA is removed. c) The substrate is then processed with reactive ion etching (RIE). d) The Cr mask is etched off. e) SEM image of stamp features in 30 degrees tilted angle. Scale bar = 200 nm.

For the substrate part, we spin-coated the imprinting base resist on silicon substrate (NXR1025 7%, 2000rpm, 45seconds), forming a 250 nm thick layer. The stamp is attached to the substrate facing down to the resist surface. The imprinting process is performed by the Nanonex NX-B200 with heating temperature of 160 °C and imprinting pressure of 400 psi for 90 seconds (figure 2.19b). The residue resist is etched by RIE with O_2/Ar=10/40 sccm, 35mTorr, 30W power for 40s. The dark field image in figure 3.19e display that the imprinted patterns (500nm spacing) are well ordered due to the diffractive blue color.

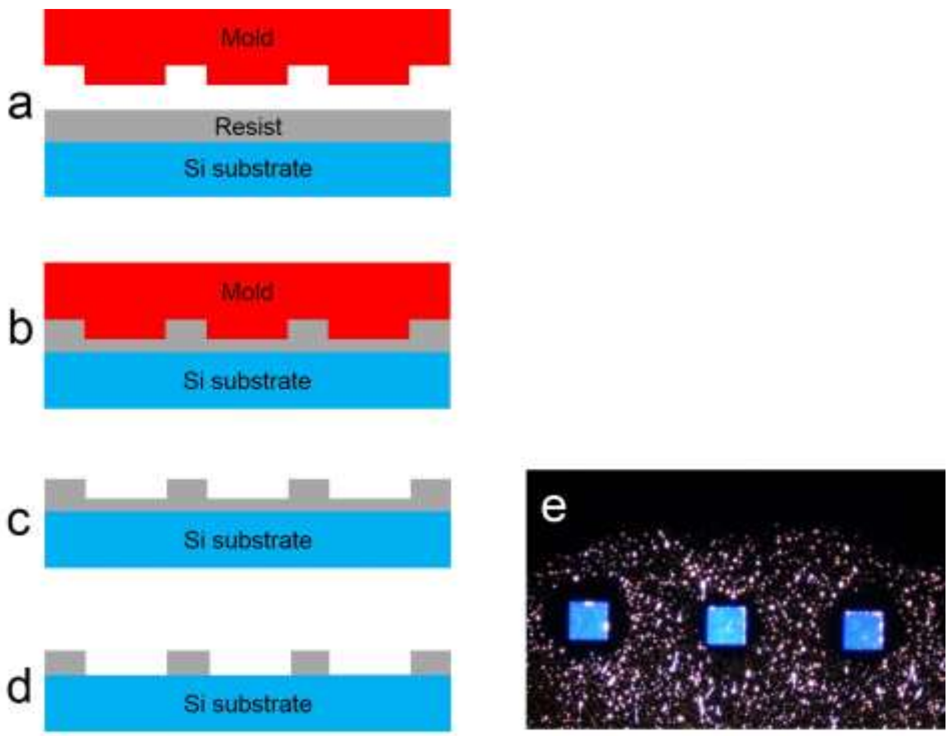

Figure 2.19. Nanoimpring process

a) Stamp is facing down to the resist surface. b) In nanoimprinter, the resist is deformed under pressure and heat. c) The resist is patterns with residue in the feature bottom. d) The residue is removed by reactive ion etching. e) Dark field image of nano imprinted substrate in (d).

Since the structure shown in figure 2.19d is obtained, the following steps are exactly the same as the ones introduce in chapter 2.1.2. After an incubation step with 1% polylysine, the substrate in immersed in 40 nm AuNP colloid functioned with negatively charge carboxyl group. The lift-offed NCA is shown in the SEM image of figure 2.20.

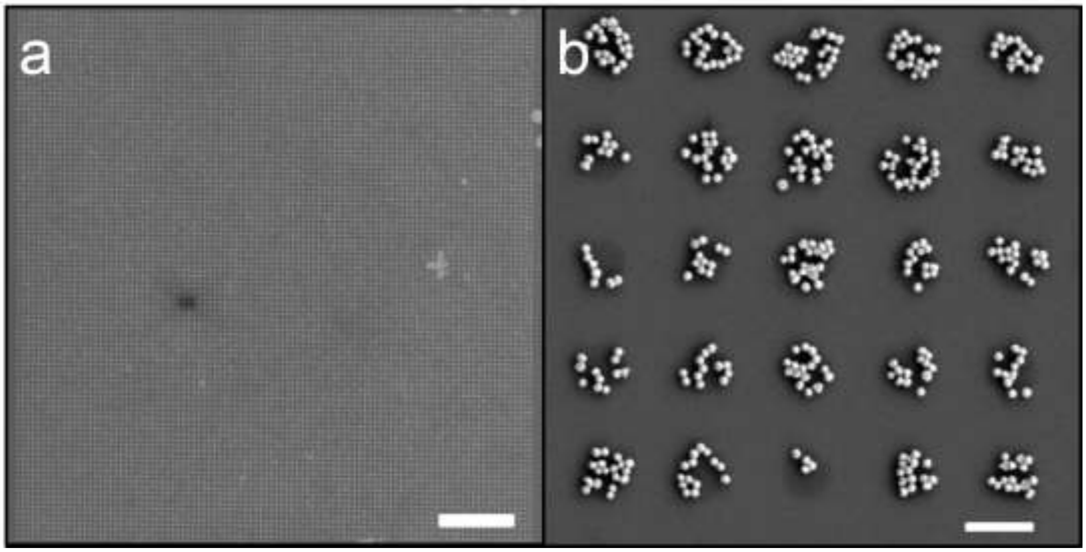

Figure 2.20. SEM image of nanoimprinted NCA

a) 70×70 μm NCA with 200 nm in diametre AuNP cluster and 600 nm array spacing. Scale bar = 10μm b). Magnified SEM imaged of NCA. Scale bar=400nm

From the image we can see that the NCA created by nanoimprinting method resemble the ones proceeded with conventional EBL method. The duplication of multiple 70×70 μm NCA is only 5 minutes imprinting time plus 10 minutes RIE processing time, which is independent from the density of patterns in the same stamp. As long as the stamp is created, any large area NCA pattern is accessible within 15min. The ratio of efficiency comparing nanoimprinting and EBL can be approximately expressed as $\boldsymbol{F}=(nAR_e)/(AR_e+nT_i)$, where A is the area of the pattern, R_e is the rate of EBL writing, T_i is the time per chip for nanoimprinting process and n is the number of chips. Obviously, the n is large in massive production yielding the F to be AR_e/T_i. T_i is constant for about 15 min. The term AR_e, time of EBL writing per chip could be hours even days if the EBL writing density is high and area is large as centimeter scale. As a result, the ratio could be in a magnitude of 10 or even higher if the whole process is automatic in a stream.

To be noticed, the designed cluster area is 200 nm while the SEM image show a cluster of 300 nm in diameter, which is 50% large than the stamp feature. This is due to the RIE etching in the lateral direction. This difference could be reduced by optimizing the resist thickness and RIE process parameters. But we should consider the expansion of features when choose the size parameters.

CHAPTER 3 OPTOPLASMONIC HETERO-NANOPARTICLE-ARRAYS

3.1 Introduction to two-dimensional nano arrays

Two-dimensional (2D) arrays of dielectric nanoparticles (NPs) achieve a regular corrugation of the refractive index and, thus, represent 2D photonic crystals (PCs) that allow for a rational tuning of photonic band-gaps,[101-102] an efficient guiding of light,[103] and a deceleration of the group velocity of light[104] through variation of the PC morphology. The light localization properties of dielectric PCs, and thus the ability to generate high local *E*-field intensities are, however, limited by diffraction. The use of noble metal NPs as building blocks in 2D metal NP arrays offers - in principle - a viable strategy to overcome this limitation. Resonant charge density oscillations, so called localized surface plasmon resonances (LSPRs), can induce an oscillating charge build-up on the surface of the noble metal NPs and a strong localization of electromagnetic fields in deeply subdiffraction limit volumes within the evanescent field of the NPs. Metal NPs re-radiate part of the incident light and, consequently, Au and Ag NPs or NP clusters arranged into arrays with periodic[26, 36, 105-108] or deterministic aperiodic[109-111] morphology efficiently diffract the incident light. Depending on the morphology of the array and the angle of incidence, light of a given wavelength λ is either diffracted into radiating modes or into evanescent modes that propagate along the surface. For specific array geometries the light diffracted into the array plane can resonantly couple to LSPR modes of the NPs to form photonic-plasmonic hybrid modes.[16, 38, 108, 112-117] These geometric resonances are associated with sharp spectral features,[118] an electromagnetic field enhancement[38] and an increase in local density of optical states (LDOS).[112]

While for interparticle separations on the order of the wavelength of light the electromagnetic interactions between individual NPs in the array are limited to diffractive coupling, at shorter interparticle separations, $\Lambda < \frac{1}{k_0} = \frac{\lambda_0}{2\pi}$, where k_0 and λ_0 are the free space wavenumber and wavelength, respectively, a hybridization[11] of plasmon modes becomes possible. Strong quasi-static near-field interactions between individual NPs result in this case in a dramatic increase in *E*-field localization.[119] If clusters of strongly coupled NPs are arranged into extended arrays, the availability of both short- and long-range coupling mechanisms provide additional opportunities for generating a cascaded multiscale *E*-field enhancement.[16] The feasibility of this concept has been validated in regular arrays of Au NP clusters (NCAs)[26] in which the E-field provided by individual clusters is further enhanced by delocalized array modes that couple to the strongly localized cluster modes.[16, 26, 36, 106, 120] Despite the appeal for realizing high *E*-field enhancements in discrete plasmonic structures and extended metal NP arrays, high dissipative losses in metals at optical frequencies set ultimate limits for trapping, storing and guiding the light in metallic structures. These functionalities remain, therefore, largely the domain of dielectric PCs.

There has recently been significant interest in mitigating the respective limitations of photonic and plasmonic materials outlined above by combining both components into metallo-dielectric – or optoplasmonic – hybrid structures.[58, 65-66, 81-84, 89, 121-123] The integration of plasmonic gap antennas into an array of dielectric NPs that generate a landscape of dielectric photonic modes is especially appealing since it promises additional degrees of freedom for tailoring the electromagnetic coupling in the array in both spatial and frequency domain.[58, 66, 68, 87] The practical realization of hybrid arrays with defined optical resonances remains, however, challenging since it requires a high level of control for simultaneously positioning both metallic and dielectric NPs. We demonstrate in this chapter that template-guided self-assembly strategies represent a facile strategy for addressing this fabrication problem. We assemble hybrid arrays that contain TiO_2 NPs and clusters of electromagnetically strongly coupled Au NPs at pre-defined lattice sites and investigate the electromagnetic coupling mechanisms that determine the optical near- and far-field responses of these novel electromagnetic materials in detail. Since the spectral range of interest in this work lies below 2.4 eV and, thus, below the band gap of amorphous TiO_2, we treat the metal oxide as a dielectric with a constant refractive index of $n_r = 1.8$.[124]

3.2 Optoplasmonic NCAs assembly and characterization

3.2.1 Template guided self assembly of optoplasmonic NCAs

Template guided self-assembly strategies[26, 41, 125-127] have two key fabrication steps: the definition of assembly sites through a lithographically fabrication technique (e.g. electron beam lithography, EBL) and the subsequent assembly of colloidal NPs onto the lithographically defined assembly sites. While EBL makes it possible to define the separation, Λ, between individual assembly sites on length scales ranging from ~10 nm to hundreds of nanometers and beyond, the self-assembly step facilitates the creation of clusters of close-packed NPs with interparticle separations of a few nanometers or below. Due to its versatility in creating gap structures over such a broad range, template guided self-assembly is a convenient method for generating multiscale NP arrays.[16, 26, 36] Another - underutilized - advantage of template-guided self-assembly strategies is that the diameter (D) and shape of the assembly sites provide some control over the size of the NPs assembled on that site.[36] We took advantage of this structural control parameter to program the morphology of optoplasmonic arrays that contain individual TiO_2 NPs and clusters of 60 nm Au NPs on separate lattice sites.

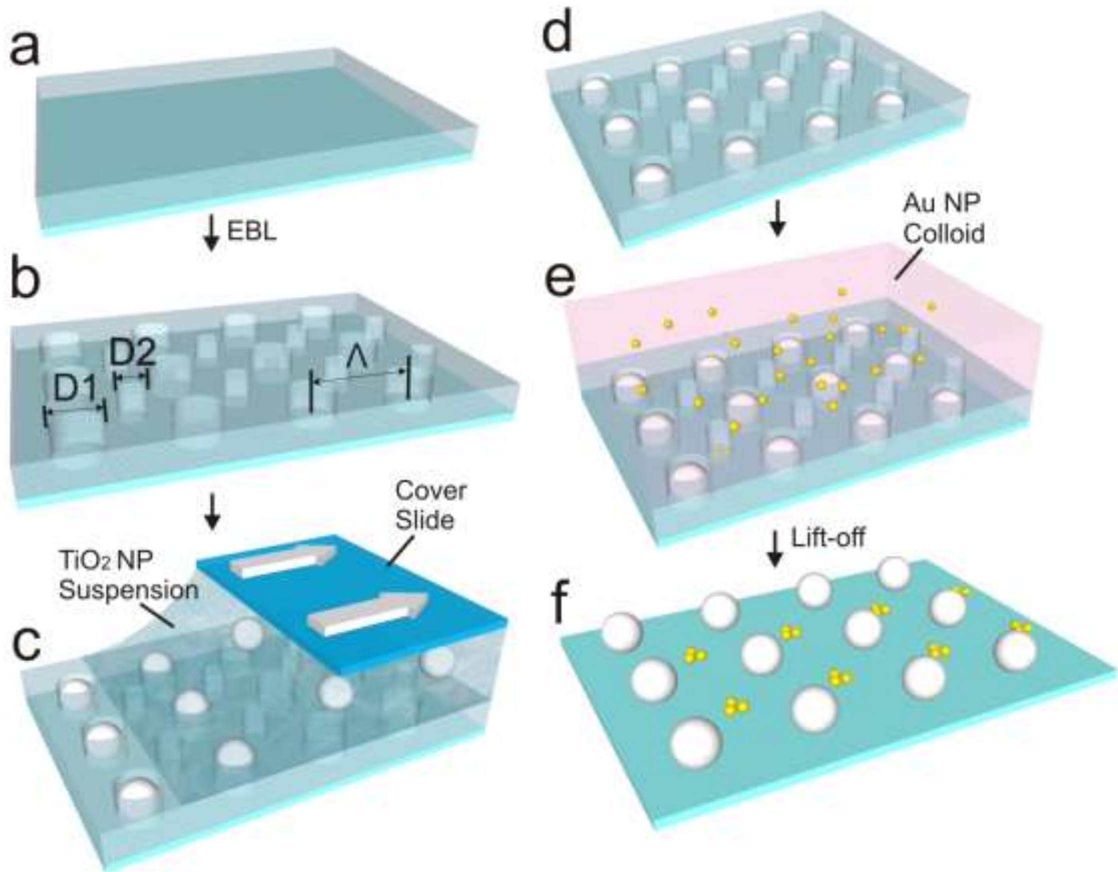

Figure 3.1. Schematic overview of template-guided self-assembly of optoplasmonic arrays.

a). A regular pattern of wells with diameters *D*1 and *D*2 (*D*1 > *D*2) is created through EBL in a PMMA layer to generate. b). a regular mask of assembly sites with two different diameters. The center-to-center separation in the *D*1 and *D*2 sub-arrays is *Λ*. d). Dragging of a suspension of TiO_2 NPs with diameters too large to bind to *D*2 across the surface results d). in an immobilization of TiO_2 NPs onto *D*1 sites. E. Smaller Au NPs are assembled onto vacant *D*2 binding sites from a colloidal solution. f). After PMMA lift-off, the final optoplasmonic array is released.

Our assembly strategy is schematically illustrated in Figure 3.1. In the first step, a lithographically defined template with two different assembly site diameters $D2 < D1$ is generated. This template is exposed to dielectric particles with an average particle diameter $d1$, $D2 < d1 < D1$, which can only bind to the assembly sites with diameter $D1$. In a subsequent second assembly step, noble metal NPs with a diameter $d2$, $d2 < D2$, are then targeted to the vacant D2 array sites. If the ratio of NP and assembly site diameter, ($d2$ / $D2$), is chosen appropriately, the assembly sites can accommodate multiple NPs.

The latter facilitates a controlled formation of NP clusters. In this study we exclusively used $d1 \approx 250$ nm TiO_2 NPs and $d2 \approx 60$ nm Au NPs. The assembly site diameters for our optoplasmonic arrays were chosen as $D1 \approx 140$ nm and D2 ≈ 270 nm.

For detailed scheme description, *A* 300 nm thin poly(methyl methacrylate) (PMMA, molecular weight 950,000, 6% in anisole) was spincoated on top of 1×1 cm glass slides (cleaned by Piranha solution for 30 minutes). The substrates were subsequently soft-baked at 170^{o}C for 15 min and then sputtered with a 10 nm gold film (Figure 3.1a). Periodic arrays of wells with diameters ($D1 = 270$ nm and $D2 = 140$ nm) and separation, Λ, were then patterned through EBL with a SUPRA 40VP SEM equipped with Raith beam blanker and a nanopattern generation system (NPGS). To optimize the binding efficiency, a dynamic ramp of the electron dosage was applied. After chemical etching of the Au film (7s with the etchant Au Etch Type TFA, Transene Co. Inc.) and development in methyl isobutyle ketone (MIBK): Isopropanol = 1:3 solution, regular arrays of wells were obtained as shown in Figure 3.1b. Carboxylic acid functionalized spherical TiO_2 NPs (~250nm diameter, Corpuscular Inc.) were cleaned through centrifugation and resuspension in DI water twice and finally dispersed to a concentration of 1.6×10^{11} NPs/mL. The substrate was treated with short plasma cleaning (3 seconds, 716V DC, 10mA DC, 7.16w, Harrick Plasma) to raise the hydrophility of its surface. The TiO_2 suspension was then pipetted onto the well template and sandwiched between the substrate supported template and a glass cover slide using a 500 μm spacer. The cover slide was translocated across the substrate with a rate of ~5mm/sec, effectively dragging the TiO_2 solution-air interface across the template substrate (Figure 3.1c). Excessive TiO_2

NPs on the PMMA surface were removed via low adhesion tape (Ultratape. #1310). The NP binding process was repeated 2 times. In the next step, the arrays were incubated with L-polylysine (molecular weight 15,000~30,000 1% in water) for 30 minutes (Figure 3.1d). The arrays were subsequently washed with DI water. In parallel, 0.5 mL of a commercial citrate stabilized 60 nm Au colloid (British Biocell International) were incubated with 2.5 μL of a 10 mM thiol-EG_7-propionate (EG = ethylene glycol) for 4 hours at room temperature. After that, the Au NP colloid was washed by centrifugation and resuspension (2 times) in 30 μL 10 mM phosphate buffer (pH = 8.6) containing 40 mM NaCl. The buffered Au NP colloid was pipetted onto the patterned area of the glass slide and incubated for 40 minutes (Figure 3.1e). Excess Au NP colloid was then removed by washing with DI water. After drying in air, the array was contacted with low adhesive tape (Ultratape #1310) to remove NPs bound to the PMMA surface. Finally the PMMA liftoff was performed with 1-methyl-2-pyrrolidinone, releasing the optoplasmonic array after rinsing with acetone (Figure 3.1f). The assembly process of TiO_2 NP arrays or Au NCAs followed similar procedures but all steps related to the immobilization of the other NP species were omitted.

The $d2$ / $D2$ ratio was intended to favor the formation of clusters with ~4 NPs since it was shown before that in self-assembled 2D NP clusters with random configuration the *E*-field enhancement reaches it maximum for cluster sizes $n \approx 4$.[16, 26] The center-to-center separation between adjacent $D1$ or $D2$ binding sites is defined as Λ in all investigated arrays. In the fabricated hybrid arrays the Λ values for the TiO_2 NP and Au NP cluster sub-arrays were identical.

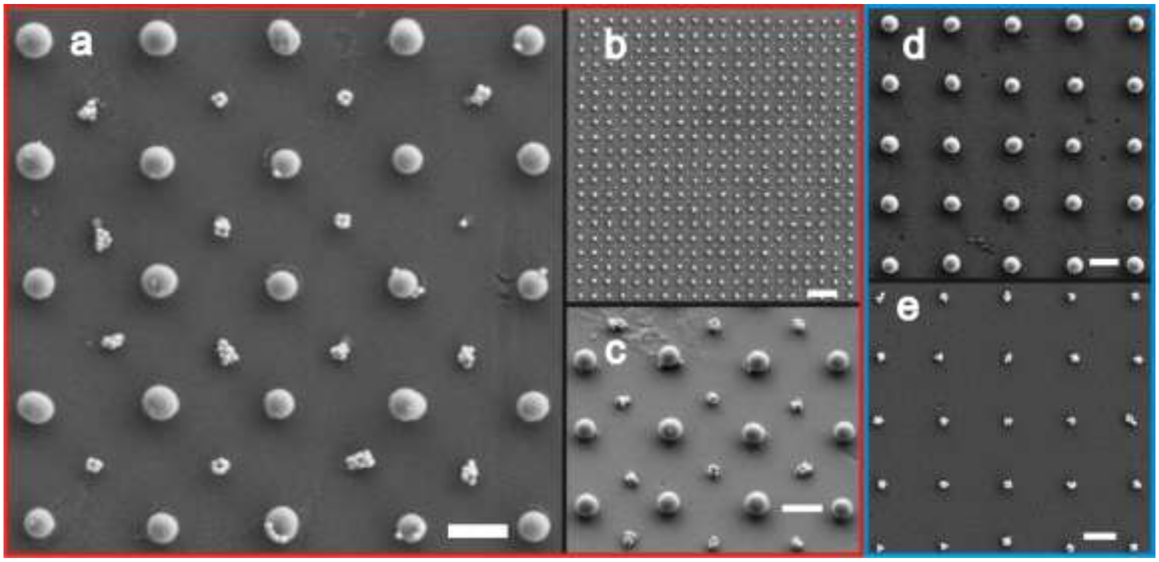

Figure 3.2. SEM images of optoplasmonic arrays.

SEM images of 2D arrays generated through template guided self-assembly of $d1$ = 250nm TiO_2 NPs and $d2$ = 60 nm Au NPs. A. Section of optoplasmonic array. B. Complete optoplasmonic array with 20×20 TiO_2 NPs. C. Side-view (30° tilt angle) of optoplasmonic array section. D. Section of TiO_2 NP array. e) Section of Au NP cluster array (NCA). Λ is 1000 nm in (A) – (E). Scale bars are and 500 nm in (A), (C) – (E) and 2 µm in (B).

Figure 3.2 shows scanning electron microscopy (SEM) images of different array types accessible with the template guided self-assembly process. A magnified sections of an optoplasmonic array is shown in (a), a complete array is shown in (b). The sideview in (c) further illustrates the positioning of discrete Au NP clusters between individual TiO_2 NPs. The images in (d) and (e) contain top views of a TiO_2 NP array and a conventional Au NCA, respectively. Λ was 1000 nm in (a-e). The SEM images in Figure 2 confirm that both TiO_2 and Au NPs can be successfully assembled into regular hybrid arrays. Although the $D1$ assembly sites in the optoplasmonic array show some contamination with additional stacked TiO_2 NPs or metal NPs on top of TiO_2 NPs under our not-yet optimized assembly conditions, the SEM images in (a-c) overall confirm that the different assembly site diameters indeed preferentially guide the TiO_2 and Au NPs to separate lattice sites. We obtained highly regular array geometries in which the TiO_2 NPs are located on the vertices of regular squares, each containing a central Au NP cluster. The average number of Au NPs on the *D*2 sites was 6.2 ± 1.2, and thus acceptably close to design target. In the following we refer to the size of the optoplasmonic arrays by the $i \times j$ TiO_2 assembly sites in the array.

3.2.2 Far-Field Characterization of Optoplasmonic Arrays

As a first step towards unraveling the multiscale electromagnetic interactions that determine the spectral properties of optoplasmonic arrays in the near- and far-field, we analyzed the elastic scattering spectra of the hybrid arrays as well as of their Au NCA and TiO_2 NP sub-arrays. To that end, we fabricated multiple arrays on identical chips with Λ in the range between 700 - 1000 nm in steps of 100 nm. The fabricated arrays contained 20×20 Au NP clusters, 20×20 TiO_2 NPs, or all of these particles combined in case of the hybrid structure. We chose Λ in the range 700-1000 nm, as we anticipated the strongest coupling between photonic and plasmonic modes to occur for grating periods that are close to the plasmon resonance of the individual Au NP clusters. The latter was determined as $\lambda_{plas} \approx 760$ nm (Figure. 3.3).

In this chapter, All computations were performed using the multiple sphere T-matrix code developed by **D. W. Mackowski[47].** We used the Au dielectric function from Johnson and Christy and assumed a constant refractive index $n_r = 1.8$ for TiO_2 NPs. For the ambient medium an effective refractive index of $n_r = 1.24$ was used.. In the far-field simulations, the incident angle was set to $\theta^{inc} = 60^\circ$ for both (1,1) and (1,0) modes, and $\varphi^{inc} = 45^\circ$ and 0° for (1,1) and (1,0) modes, respectively. The scattering angles were $\theta^{det} = 0^\circ$ and $\varphi^{det} = 0^\circ$. Near field simulations were performed for normal incidence onto the array plane. The Au NP clusters were modeled as trimers with 4 nm edge-to-edge gap. The base of the regular trimers was parallel to the x-axis. The step size for E-field intensity profile was 2 nm.

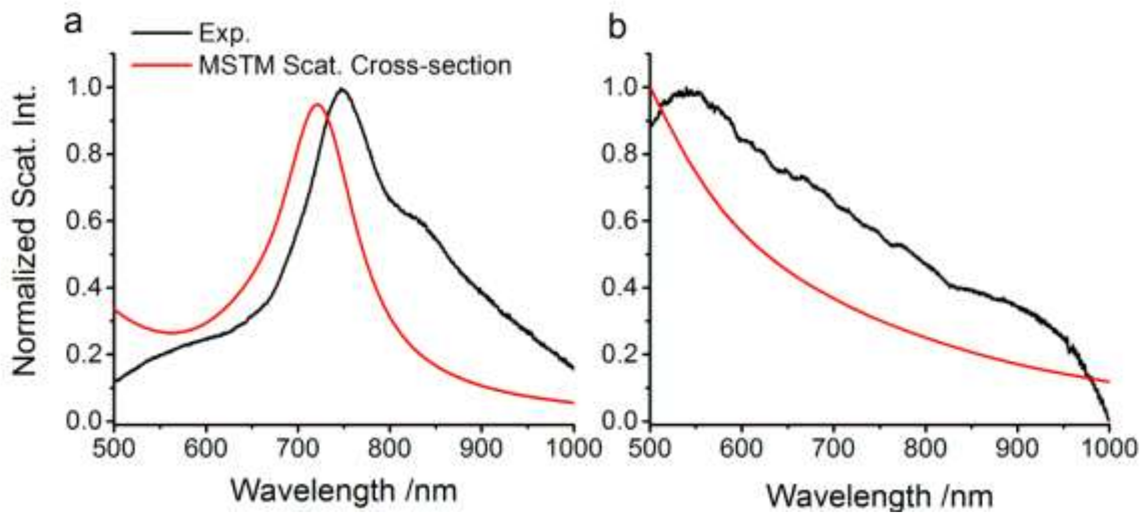

Figure 3.3. Experimental and MSTM-simulated far field spectra of optoplasmonic array components.

a). Spectra of Au clusters. For the MSTM result, a single Au trimer as described in the Methods section was simulated. b). Spectra of TiO_2 NP. The black curve represents the spectrum of an individual TiO_2 NP immobilized on glass substrate. The red curve is the MSTM simulation result for one $n_r = 1.80$ sphere (Diameter = 250nm) embedded in a medium with $n_r = 1.24$.

A systematic scheme of the experimental set-up used for the spectroscopic characterization of the fabricated arrays under oblique illumination is shown in Figure 3.4. The fabricated arrays were illuminated with unpolarized white light through an oil darkfield condenser with a numerical aperture (NA) of 1.2-1.4, corresponding to a range of the incident angle of θ^{inc}= 52-68˚. We limited the incident wave vectors ($\vec{k}^{inc}$) with a variable slit in the entrance port (see Methods) and detected the light scattered normal to the array plane through a 10x air objective with a NA of 0.25.

In the setup, the samples were illuminated through an oil dark field condenser (NA=1.2 ~ 1.4). The entrance plane of the condenser was covered with a non-transparent disk which had an opening slit (3×6 mm) on one side, to define the illumination angle φ^{inc}. An air objective with NA=0.25 was used for signal collection. The spectra were collected through a spectrometer (Andor SR303i) equipped with a CCD camera (Andor DU401-BR-DD). The original spectra were corrected by background subtraction from an adjacent area on the chip and normalized by the excitation profile of the light source.

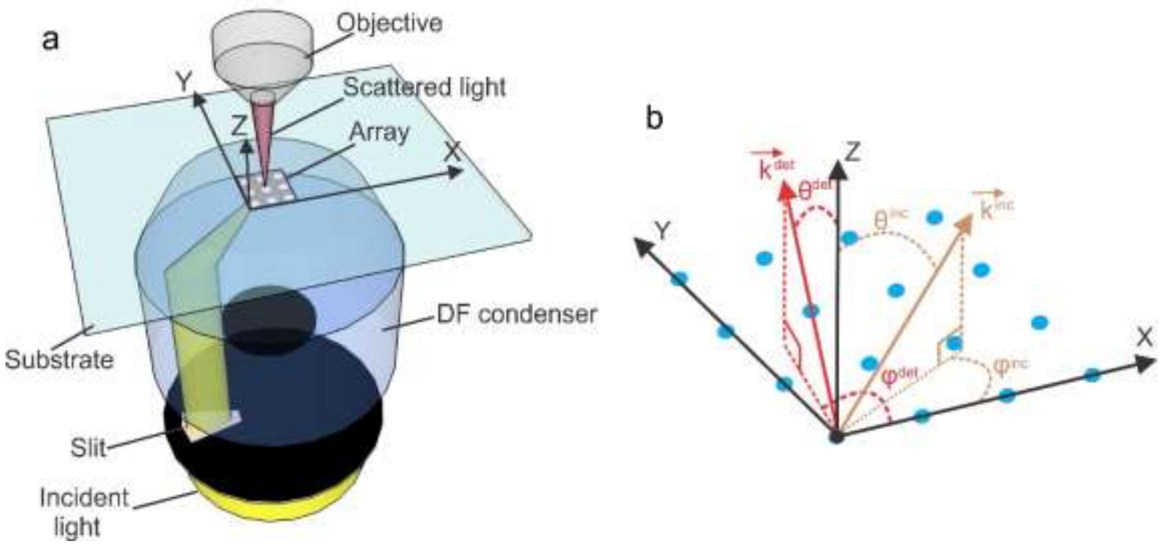

Figure 3.4. Experimental set-up for elastic scattering spectroscopy.

a). Experimental set-up for elastic scattering spectroscopy. The sample is illuminated through a darkfield (DF) condenser whose back aperture is partially blocked. b). Definition of incident ($\vec{k}^{inc}$) and detected scattered ($\vec{k}^{det}$) wave vector and angles $\theta_{m,n}^{det}$ and φ^{det}, θ^{inc}, and φ^{inc}. The position of NPs in the array plane are indicated as blue dots.

The regular 2D NP arrays investigated in this work represent in a first approximation optical gratings, whose diffraction polar angle $\theta_{m,n}^{det}$ for a specific wavelength λ depends on the grating orders *m* and *n*, the array periods along the x-,y-axes (Λ_x and Λ_y), the incident polar angle θ^{inc}, and the azimuth angle φ^{inc}, φ^{det} for incidence and detection, respectively. With a set of 1-dimensional Laue equations

$$\Lambda_x\left(\sin\theta_m^{det}\cos\varphi^{det} - \sin\theta^{inc}\cos\varphi^{inc}\right) = m\frac{\lambda}{n_r} \tag{1}$$

$$\Lambda_y\left(\sin\theta_n^{det}\sin\varphi^{det} - \sin\theta^{inc}\sin\varphi^{inc}\right) = n\frac{\lambda}{n_r} \tag{2}$$

where θ_m^{det} and θ_n^{det} are the detection angles along the *x*- and *y*-direction, the detection angle $\theta_{m,n}^{det}$ for a grating order (*m*,*n*) in the 2-dimensional array is obtained for $\varphi^{det} = 0°$ as:

$$\theta_{m,n}^{det} = \arcsin\left[\begin{array}{c}\left(\sin\theta^{inc}\cos\varphi^{inc} + m\frac{\lambda/n_r}{\Lambda_x}\right)^2 + \\ \left(\sin\theta^{inc}\sin\varphi^{inc} + n\frac{\lambda/n_r}{\Lambda_y}\right)^2\end{array}\right]^{1/2} \tag{3}$$

As we will show in the following, the recorded spectra (Figure 3.5) of all three investigated array types are dominated by two radiating diffraction modes, which can be assigned using equation (3).

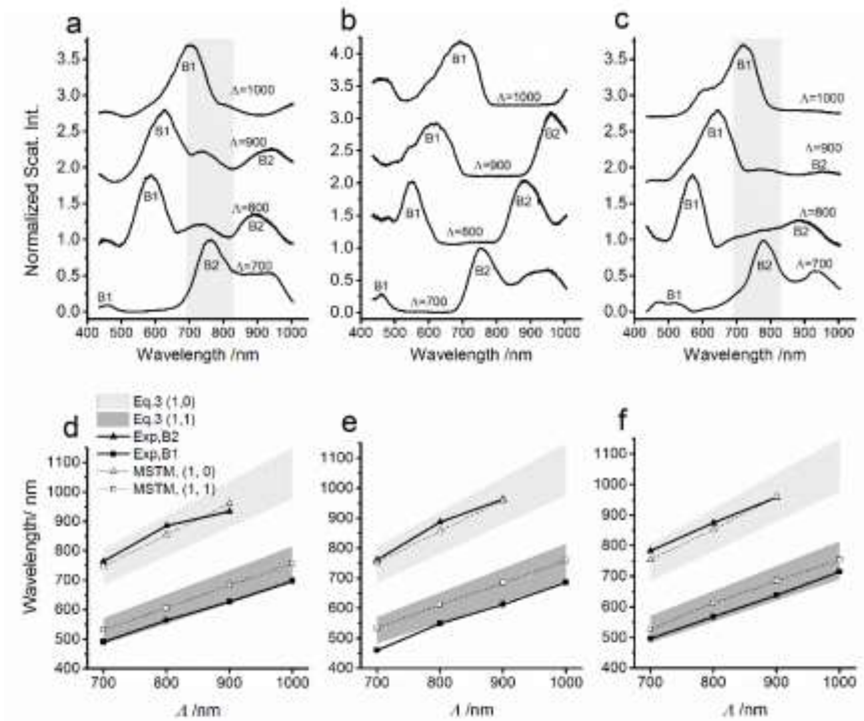

Figure 3.5. Elastic scattering spectra of optoplasmonic hybrid array and control arrays.

Elastic scattering spectra of a) Au NCA, b) TiO2 NP array and c) optoplasmonic hybrid array. The spectra were recorded for arrays with periodicities of Λ = 700 nm, 800 nm, 900 nm, and 1000 nm. All spectra contain the diffractive grating orders (1, 0) (B2) and (1,1) (B1). In A and C the shaded areas mark the spectral position of the plasmon resonance in individual Au NP clusters ($\lambda_{plas} \approx 760$ nm). The fitted peak wavelengths (Exp) of B1 and B2, the spectral range (Eq.3) for (1,1) and (1,0) grating orders for NA = 1.2-1.4 according to equation (3), and MSTM simulated spectral positions (MSTM) for an incident angle of θ^{inc}= 60˚ (φ^{inc}= 45˚ and 0˚ for (1,1) and (1,0) mode, respectively) and n_r = 1.24 as function of Λ are summarized in d) for Au NCAs, in e) for TiO_2 NP arrays, and in f) for optoplasmonic hybrid arrays.

We start our analysis with the Au NCAs plotted in Figure 3.5A. The fitted peak wavelength of the bands marked as B1 and B2 together with the predicted wavelength range of the (1, 1) and (1, 0) grating orders are summarized in (Figure 3.5D). The theoretical predictions are based on the evaluation of equation (3) with azimuthal angles of φ^{inc} = 0 for the (1, 0) mode and φ^{inc} = π/4 for the (1, 1) mode. Furthermore, we assumed that the collecting microscope objective is located in infinity ($\theta^{det}_{m,n}$= 0˚) and we used an effective refractive index of n_r = 1.24 as average between glass substratum and air superstratum. The linear red-shifts of the fitted peak wavelengths of B1 and B2 as function of Λ are in very good agreement with the theoretical predictions and confirm that these spectral features arise from photonic grating modes. In addition to the grating modes, the Au NCA spectra also contain a spectral feature in the range between 690 - 830 nm (vertical grey-shaded areas in Figures 3.5a and c), which we assign to the plasmon resonance of Au NP clusters on the *D*2 assembly sites (see Figure. 3.3). While for Λ = 700 nm the (1, 0) grating mode and plasmon scattering band spectrally coincide, in all other spectra the plasmon band is identifiable as a shoulder or separate peak near $\lambda_{plas} \approx 760$ nm.

The spectra and fitted peak wavelengths for TiO_2 NP arrays are summarized in Figures 3.5b and e. As observed before for the Au NCAs, the spectra contain again a set of bands B1 and B2 whose spectral position shifts linearly with Λ. Although the experimental values of B1 lie slightly below the range predicted by equation (3), the agreement is still very good, given the complexity of the experimental system. Differences in the effective refractive index of the effective array plane, the size mismatch between the TiO_2 and Au NPs (*d1* > *d2*), as well as experimental variations in the grating period can all contribute to the observed discrepancies.

The spectral data of the optoplasmonic arrays are shown in Figures 3.5c and f. In this case the fitted peak positions of B1 and B2 are again in excellent agreement with the predictions for the (1, 0) and (1, 1) diffraction bands according to equation (3). As observed for the conventional Au NCAs, the spectra in Figure 3.5C also contain a distinct feature that arises from the NP cluster plasmon. Interestingly, both Au NCAs and optoplasmonic hybrid arrays have lower relative intensities in the spectral range > 760 nm when compared with the all-dielectric TiO_2 NP array. Direct excitation of plasmons as well as photonic-plasmonic mode coupling can achieve a localization of the optical energy in the form of gap plasmons in the NP clusters. This energy redistribution, together with the unavoidable dissipative losses in metals can account for the reduction in diffracted optical power in this spectral range.

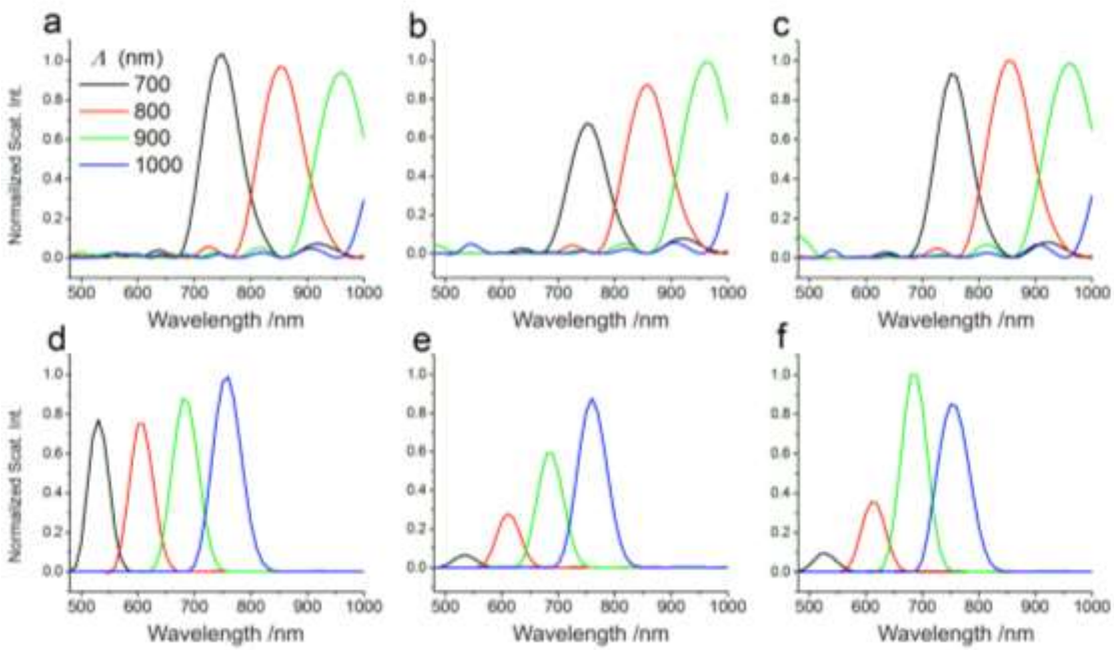

Figure 3.6. MSTM-simulated far-field scattering spectra of optoplasmonic hybrid array and control arrays.

MSTM-simulated far-field scattering spectra of 8×8 arrays with $\theta^{det} = 0^{\circ}$ and $\varphi^{det} = 0^{\circ}$. (a),(d) Au NP cluster array (NCA). (b),(e) TiO_2 NP array. (c),(f) Optoplasmonic array. (a-c) were obtained for $\theta^{inc}= 60^{\circ}$ and $\varphi^{inc}= 0^{\circ}$ to simulate the (1, 0) mode. (d-f) were obtained for $\theta^{inc}= 60$ and $\varphi^{inc}= 45^{\circ}$ to simulate the (1, 1) mode.

The excellent agreement between recorded and predicted spectral positions according to equation (3) confirms a high structural integrity for all three assembled array types. The recorded far-field data also provide a superb testbed for the calibration of electromagnetic multiple sphere T-Matrix (MSTM) simulations (**see Methods section for details**). The spectral positions of the simulated (1, 0), (1, 1) grating orders in model arrays comprising 8×8 Au NP clusters, 8×8 TiO_2 NPs, or both TiO_2 NPs and Au NP clusters for polar angles $\varphi = 0^{\circ}$ and 45°, respectively, are included in Figure 3.5d-f. Some exemplary simulated full spectra are provided in Figure 3.6 together with the spectral assignments. The close concordance between experimental and MSTM-simulated data in Figure 4d-f confirms that the method accurately describes the far-field spectral response of the arrays under investigation.

3.2.3 Near-Field Characterization of Optoplasmonic Arrays

In the next step we applied the calibrated MSTM method to map the interactions of the individual components of the photonic-plasmonic hybrid arrays in the near-field. To that end, we first calculated the near-field spectra at the hottest spots in arrays comprising 20×20 TiO_2 NPs, 20×20 Au NP clusters, and optoplasmonic hybrid arrays of 20×20 TiO_2 NPs and the corresponding number of Au NP clusters as function of Λ. All near-field spectra were calculated for a plane wave with normal incidence since this corresponds most closely to the experimental SERS measurements we performed. We performed these calculations for triangular NP clusters that had one base oriented parallel to the incident E-field for polarization pointing either in the x-direction or rotated by π/4.

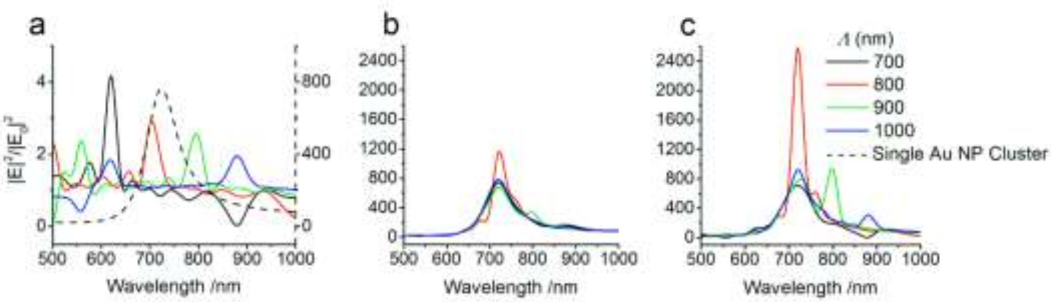

Figure 3.7. MSTM-simulated E-field intensity enhancement.

MSTM-simulated E-field intensity enhancement spectrum at the hottest electromagnetic spot in arrays.a) an array of 20×20 TiO2 NPs; b) a 20×20 Au NCA; and c) the combined optoplasmonic array. The near-field intensity spectrum for an individual NP trimer is included in (a) for comparison. Please note the different E-field intensity scales in (a). The E-field intensity of the photonic modes (solid lines) is plotted to the left scale; the E-field intensity of the NP cluster (dashed line) is plotted to the right scale.

Since both of these simulations provided essentially identical trends and peak *E*-field enhancements, we focus our discussion in the following on the x-polarized incident light.

The obtained near-field spectra are summarized in Figure 3.7. The *E*-field enhancement for the all-dielectric TiO_2 NP array in Figure 5a shows discrete resonances, whose spectral positions red-shift with increasing Λ. The *E*-field enhancements in the dielectric arrays are much lower than that observed in Au NCAs (Figure 3.7b). For the latter the near-field spectra are dominated by the plasmon resonance with a simulated peak wavelength of ~720 nm. The near-field intensity spectrum for an individual Au NP trimer is included for comparison in Figure 3.7a. Interestingly, the combination of TiO_2 NPs and Au NP clusters in optoplasmonic arrays (Figure 3.7c) achieves a further significant boost of the near-field intensities beyond what can be obtained in the NCAs at the wavelengths corresponding to the photonic resonances in the TiO_2 NP array. Light incident on optoplasmonic arrays normal to the surface is efficiently re-radiated into the array plane by the TiO_2 NPs with the exact wavelength of the re-radiated light depending on the periodicity of the diffractively coupled NPs. If the re-radiated light overlaps with the plasmon resonance of the NP clusters, it is efficiently localized through excitation of LSPRs in the NP clusters. According to the MSTM simulations the near-field maxima of the photonic array modes and the LSPRs overlap in optoplasmonic arrays with $\Lambda \approx 800$ nm. In this geometry photonic-plasmonic mode coupling facilitates a cascaded enhancement of the E-field intensity provided by the individual clusters.

We point out that Au NCAs by themselves act as a grating and that photonic-plasmonic mode formation also modulates the *E*-field enhancement in these arrays.[16] Indeed, the *E*-field intensity in Au NCAs is predicted to be Λ–dependent as well and also peaks in arrays with $\Lambda = 800$ nm (Figure 3.7b). The MSTM simulations show, however, clearly that the combination of dielectric and metallic NPs in the optoplasmonic array (Figure 5c) generates a higher peak *E*-field enhancement than the NCAs, The peak enhancement in the optoplasmonic array is by a factor of 2 higher than that in the NCA $\frac{|E|^2_{optoplas}}{|E_0|^2} \approx 2500$ vs. $\frac{|E|^2_{NCA}}{|E_0|^2} \approx 1250$. We attribute this gain in the optoplasmonic arrays to a more efficient in-plane concentration of the incident light through the TiO_2 NP sub-array. We mention in passing that the exact value of the E-field intensity increases with array size.

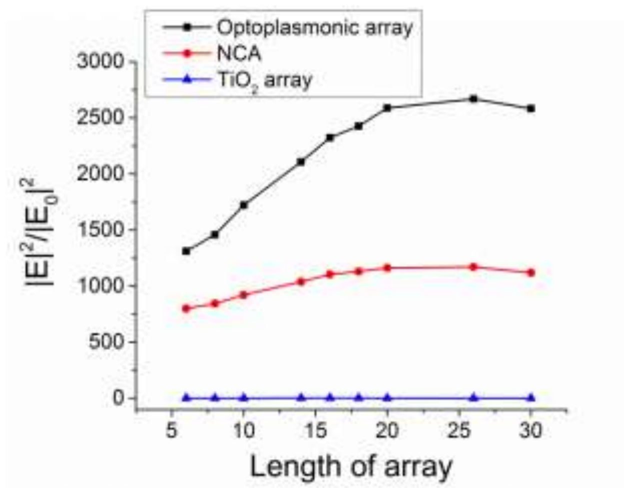

Figure 3.8: MSTM simulated near field intensities vs. length of the arrays.

MSTM simulated near field intensities of the hottest point as a function of array size in an optoplasmonic array (black), 60 nm Au NP trimer NCA (red), and TiO_2 NP array (blue).

We systematically evaluated the *E*-field intensity in the three investigated array types as function of array size (Figure 3.8) and found that the peak *E*-field intensity grows faster in optoplasmonic than in conventional plasmonic arrays and converges at array sizes of approximately 20×20 TiO_2 NPs.

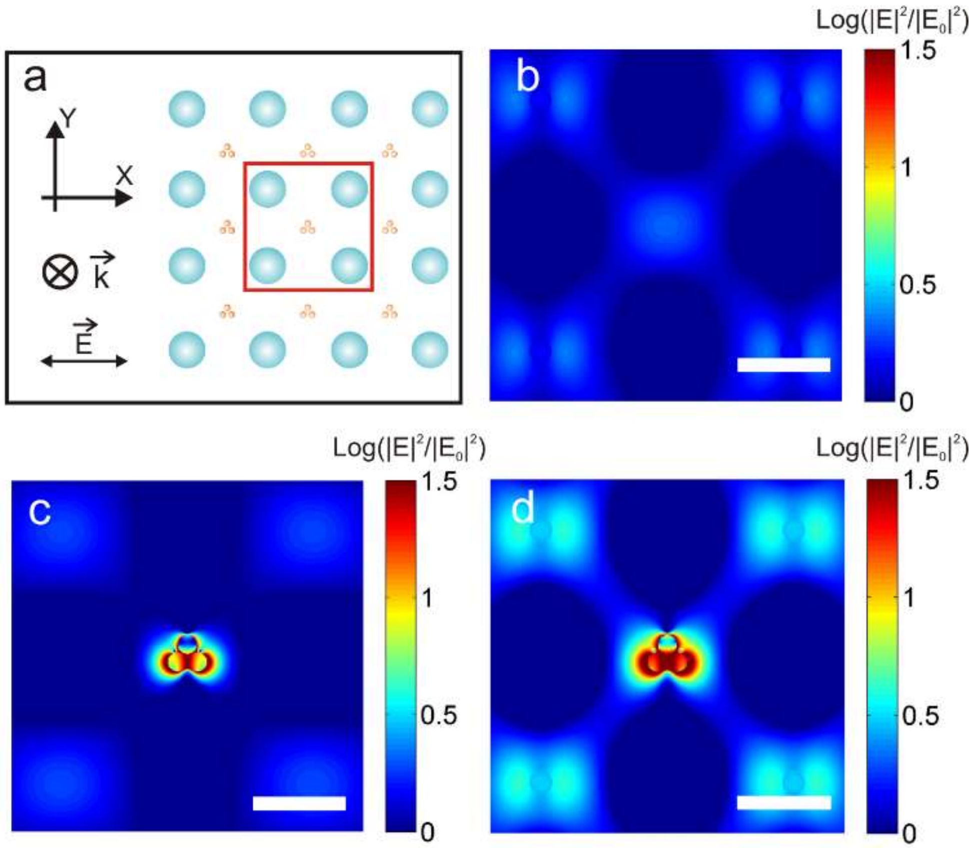

Figure 3.9. MSTM E-field distribution simulation.

(a) Arrays geometry for the optoplasmonic array. Although only the center area (red box, Au NP plane) is plotted in the near-field map, the whole array is considered in the simulations. Near-field intensity enhancement, $|E|^2/|E_0|^2$, maps for (b) an array of 20×20 TiO_2 NPs, (c) a 20×20 Au NCA, and d) the corresponding optoplasmonic array at λ = 720 nm. The combination of metallic and dielectric NPs in (d) boosts the near-field intensity not only in the hot-spots defined by the NP clusters but also at locations in the array that are not in the direct vicinity of a NP cluster. All scale bars are 500 nm.

The synergistic interplay between metallic and dielectric array components is further illustrated in Figure 3.9**,** which contains maps of the spatial *E*-field intensity enhancement distributions in the dielectric, plasmonic, and optoplasmonic arrays with Λ = 800 nm at λ = 720 nm. Consistent with a constructive interference of in-plane radiated light that results in the formation of delocalized photonic modes, the TiO_2 NP array (Figure 3.9b) shows increased *E*-field intensity not only in the direct vicinity of the dielectric NPs but also in the interstitial spaces between the NPs. The *E*-field enhancement is much weaker than in the case of the Au NCA in Figure 6c, where the electromagnetic energy is strongly focused into the junctions between the NP clusters. This enhancement is further amplified if the Au NP clusters are positioned into the focal points of enhanced *E*-field intensity of the TiO_2 NP sub-array (Figure 3.9d), where the Au LSPRs can be excited by the focused *E*-field provided by the dielectric array. Photonic-plasmonic mode[58, 65] formation results in this case in an increased *E*-field enhancement not only around the Au NP clusters but – albeit to a lesser degree – also in the vicinity of the TiO_2 NPs and throughout the array. Both the increase in peak *E*-field intensity as well as the increase in accessible volume with enhanced *E*-field intensity is anticipated to translate into an overall performance advantage of the optoplasmonic array as substrate for surface enhanced Raman spectroscopy (SERS).

3.2.4 Validation of Λ – dependent E-field Intensity Enhancement in Optoplasmonic Arrays through SERS

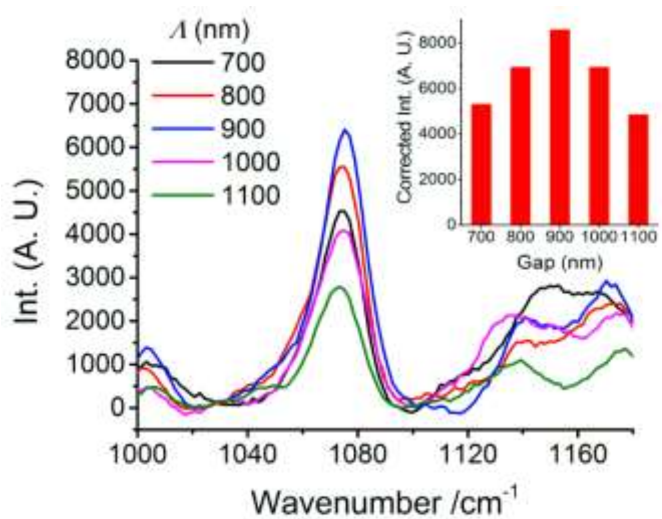

Figure 3.10. SERS spectra from optoplasmonic array

SERS spectra of para-mercaptoaniline (pMA) in the range 980 - 1140 cm^{-1} obtained on optoplasmonic arrays with different Λ values. The inset shows the filling-fraction corrected intensities of the 1077 cm^{-1} C-S stretch mode as function of Λ.

We measured the area-averaged SERS spectra of the small test molecule para-mercaptoaniline (pMA) chemisorbed onto optoplasmonic arrays with array periods between Λ = 700 - 1100 nm. The entire sample was excited with a 785 nm diode laser in epi-illumination configuration, and we collected the signal from a central strip of 4 µm width, as defined by the opening slit of the spectrometer, across the entire array.

All samples were first treated with an oxygen plasma cleaning (300 sccm, 300 w, 10 min). After an incubation in 10 mM para-mercaptoaniline (in ethanol) for 12 hours, the substrates were then rinsed with copious amount of ethanol and dried in a nitrogen flow. The samples were excited via a diode laser (λ=785nm). The total power in the sample was 46.5 mW. A 40x air objective (NA=0.65) was used for SERS signal collection with an acquisition time of 10 s. The SERS spectra were background- and baseline-corrected and the peak height of the 1170cm^{-1} peak was determined as the maximum intensity of a Lorentzian fit.

In Figure 3.10 we plot the background corrected spectra in the spectral range 980-1140 cm^{-1} that contains the C-S stretch mode at 1077 cm^{-1}. The peak intensity of this vibrational transition exhibits a non-linear dependence of the SERS signal intensity on Λ. The SERS signal intensity initially increases with growing Λ and peaks for Λ = 900 nm. If Λ is further increased, the SERS signal decreases again. Both the spectral position of the photonic-plasmonic resonances and the filling fraction (*i.e.* NPs per area) depend on Λ. We accounted for this effect in the filling fraction corrected intensities plotted as inset.

The maximum of the SERS signal intensity remains at Λ = 900 nm after correction for the different number of clusters in the active area.

SERS signal intensities scales as the product of the *E*-field intensities at the pump and Raman scattering wavelengths. Consequently, the observed Λ-dependence of the SERS signal intensity in Figure 3.10 confirms an additional enhancement of the *E*-field intensity in the array plane due to geometry-dependent photonic-plasmonic mode coupling. Although the experimentally determined optimum Λ value is somewhat longer than the predicted value (900 *vs.* 800 nm), this discrepancy is consistent with the shift between the experimentally observed and simulated plasmon resonance wavelengths (780 *vs.* 720 nm). The origin of the differences between simulations and experiments are attributed to the necessary simplifications in the theoretical modeling (effective homogenous ambient refractive index, ideal geometries, etc.).

3.2.5 Conclusion

Dielectric and metallic optical NPs have synergistic electromagnetic properties but their integration into optoplasmonic materials with novel properties requires new fabrication approaches that provide precise control over the location of the individual building blocks. We have demonstrated in this chapter that template guided self-assembly can address this important nanofabrication need since the technique achieves a precise positioning of both colloidal metal and dielectric NPs at separate pre-defined lattice sites. Provided that the ratio of assembly site diameter and NP diameter are adequately chosen, the self-assembly technique can also generate clusters of electromagnetically strongly coupled Au NPs. We took advantage of this versatility to integrate Au NP clusters into a regular landscape of

TiO_2 NPs and generated hetero-NP-arrays that sustain simultaneous electromagnetic interactions on multiple length scales. The few nanometer gap separations within the Au NP clusters give rise to strong direct near-field coupling, whereas the TiO_2 NPs and NP clusters with separations of a few hundreds of nanometers are diffractively coupled. Photonic and plasmonic modes in the array efficiently couple when the photonic modes provided by the TiO_2 NP array overlap resonantly with the LSPRs of the Au NP clusters. This coupling further amplifies the *E*-field enhancement provided by the Au NP clusters and simultaneously increases the *E*-field enhancement in the space between the NPs throughout the array.

The ability to combine NPs of different composition in one array provides additional degrees of freedom for a rational tuning of the complex multiscale electromagnetic interactions in both spatial and frequency domain, as well for controlling the phase landscape[87] that are missing in conventional plasmonic and dielectric arrays. Optoplasmonic arrays offer, therefore, many opportunities for overcoming the limitations of conventional metallic or dielectric arrays in applications that require increased *E*-field intensities, tailored near- and far-field spectra, and/or tunable emission directionality in areas as diverse as biosensing, information processing, cryptography, and photovoltaics.

3.3 Collective photonic-plasmonic resonances in optocplasmonic arrays

3.3.1 Introduction

Localized surface plasmons (LSP) are collective oscillations of conduction band electrons that are responsible for the unique optical properties of noble metal nanostructures.[1, 128-129] Light incident on noble metal nanostructures excites LSP resonances (LSPRs) and the resulting coherent charge density oscillations generate intense oscillating *E*-fields in the vicinity of the nanoparticles (NPs). While individual NPs are already effective nanoscale antennas in the optical range of the electromagnetic spectrum, their performance and functionality can be optimized and extended by integrating multiple NPs into discrete structures or entire arrays.[130-132] Two coupling regimes determine the properties of these higher order noble metal NP structures. Quasistatic near-field interactions on short interparticle separations ($< \lambda/2\pi$) facilitate an efficient localization of the incident *E*-field into electromagnetic hot-spots located in the gap between two NPs. Consequently, nanoscale plasmonic antennas have large antenna apertures.[119, 132-133] At the same time, the high density of local optical states (LDOS) associated with plasmon resonances with intrinsically small mode volumes boosts the radiative rate of quantum emitters.[16, 31, 134-135] NPs separated by longer distances interact *via* far-field diffractive coupling. Rayleigh anomalies that arise in regular NP arrays at the diffraction edge, when a diffraction order radiates at a grazing angle into the array plane, are of particular interest since under these conditions LSPRs and in-plane diffracted photonic modes can interact synergistically.[136] If the photonic mode overlaps with the LSPR, photonic-plasmonic hybrid modes with extraordinarily sharp lineshapes can be generated.[38, 113, 136-137] These collective array resonances are commonly referred to as surface lattice resonances (SLRs).[112, 138] The *E*-field experienced by an individual NP in an array is determined by the sum of the incident *E*-field and the *E*-field re-radiated by all other NPs in the array at the location of the NP. Careful analyses of SLRs in one- and two-dimensional chains of NPs revealed that the narrow lineshapes are determined through wavelength dependent dipolar coupling[37] and that the observed narrow spectral features are the result of a positive singularity in the real part of the dipole sum.[38, 137, 139] Another beneficial aspect of the underlying delocalized modes, besides their sharp spectral linewidth, is an increase of *E*-field intensity and LDOS between the array defining metal NPs. This effect in particular has created interest in collective modes as a design strategy for more homogeneously "hot" plasmonic surfaces.[114-115, 140-143]

Most studies in the area of collective photonic-plasmonic arrays have so far focused on lattices comprising spherical NPs,[16, 38, 144] nanodisks[143, 145-147] or nanorods[112, 138, 140, 148-149] made of gold or silver as building blocks. Some studies also considered nanoholes[150] and nanopillars.[151] Previous studies by Christ *et al.* have demonstrated in multilayer nanowire arrays that near-field coupling is an important additional control parameter in plasmonic lattices.[152] Recent advancements in the area of template guided self-assembly and NP manipulation techniques make it now possible to integrate clusters of electromagnetically strongly coupled NPs into regular arrays[16, 26, 36] or to combine noble metal NP clusters with high refractive index dielectric NPs into mixed metal-dielectric hybrid arrays.[67] The aim of this chapter is to characterize the effect of this additional configurational variability on collective mode formation and to elucidate general design guidelines for photonic-plasmonic resonances with defined near- and far-field responses.

3.3.2 Effect of NP clustering on surface lattice resonances.

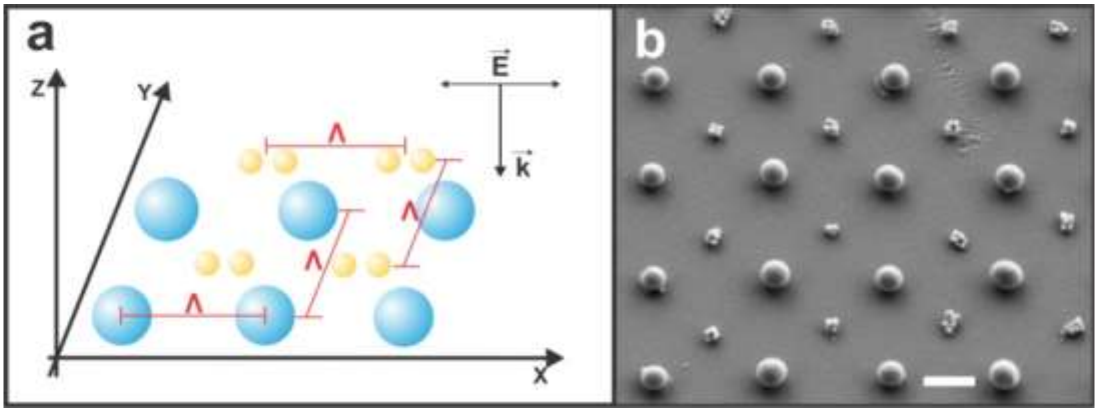

Figure 3.11. Illustration of models

(a) Schematic illustration of a mixed metal-dielectric NP hybrid array. (b) SEM of fabricated array with Λ = 1100nm. Scale bar = 500nm.

We simulated two-dimensional arrays of 60 nm diameter NPs embedded in a homogeneous ambient medium of refractive index n_r = 1.50 through finite difference time domain (FDTD) simulations and using periodic boundary conditions.[91] We used the gold dielectric function by Johnson and Christy.[92] To quantify the effect of NP clustering we replaced the individual NPs with NP dimers, which represent the simplest possible model to capture the essential physics of the electromagnetic coupling in NP clusters. We chose an interparticle separation of s = 4 nm as a conservative estimate of the interparticle spacing in NP cluster arrays (NCAs)[16, 22, 26, 36, 106] obtained through template guided self-assembly.[153] One class of material of interest and our simulation model is presented in Figure. 3.11. We assumed a normal incidence of the light on the sample and we used linearly polarized light. In the case of the dimers, the *E*-vector was oriented along the *x*-axis and pointed parallel to the long dimer axis. We systematically varied the lattice spacing, Λ, in the array and calculated extinction spectra and *E*-field intensity enhancements for different values of Λ. Fig. 2(a) and b contains the extinction spectra as function of the modulus of the lattice vector $k = 2\pi/\Lambda$, $k = 0.79 – 1.79 \times 10^7$ rad/m (corresponding to $\Lambda = 800 – 350$ nm), for square arrays of 60 nm gold NP monomers and dimers, respectively. The plots also contain the diffraction edges, $k'(m, n)$, of the square array as solid lines, which are given by the Bragg diffraction condition as:

$$k'^2 = n^2(\frac{2\pi}{\Lambda}) + m^2(\frac{2\pi}{\Lambda}) \qquad (1)$$

where (n, m) are integers defining the diffraction order along the x- and y-axis, respectively.[154]

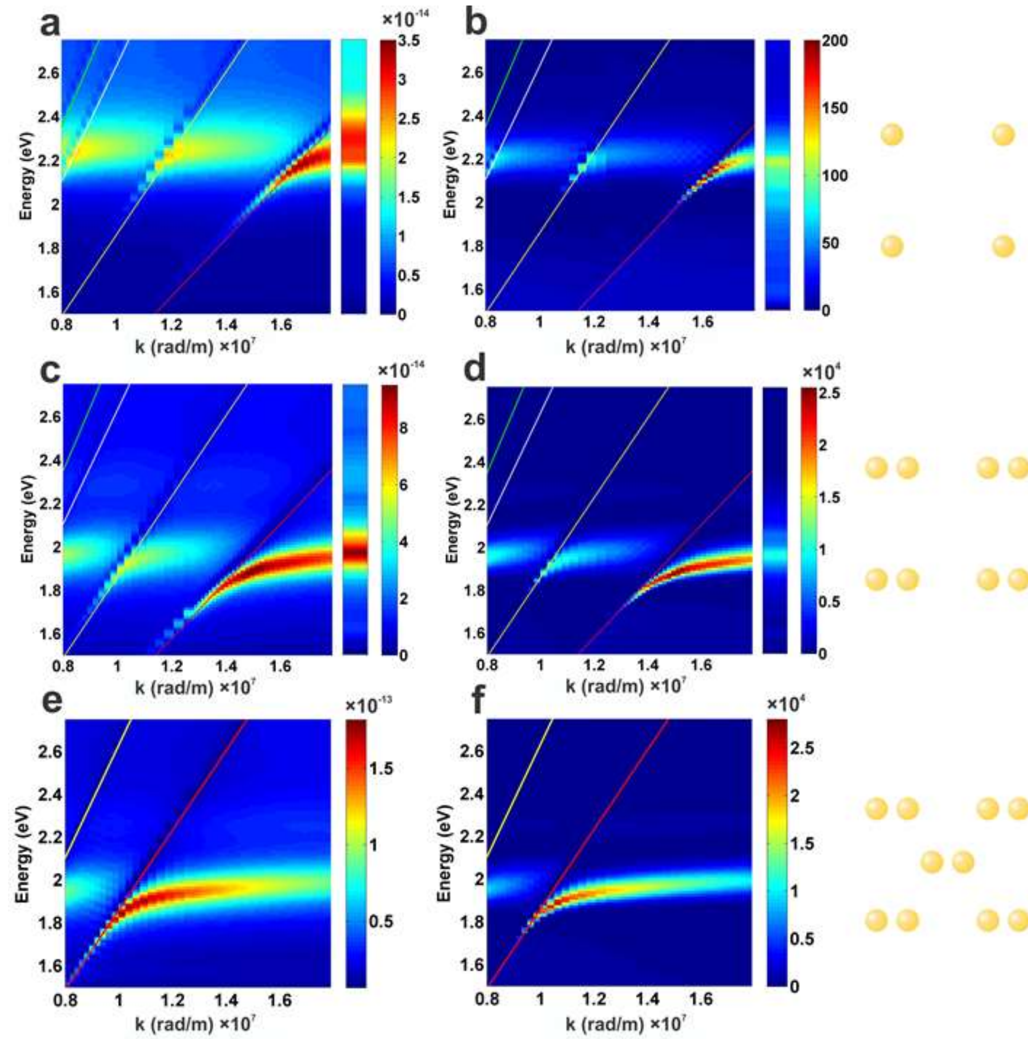

Figure 3.12. Extinction and E-field intensity enhancement diagram of NP arrays.

Extinction (a, c, e) and E-field intensity enhancement (b, d, f) as function of the lattice vector k in gold NP square monomer (a, b), square dimer (c, d), and centered square dimer (e, f) arrays. Spectra of isolated monomers and dimers are added as separate column next to the respective dispersion diagram in (a-d). The isolated monomer spectra in (a) and (c) were scaled by a factor of 1000 and 500, respectively. The extinction was calculated as (1-T)A , where T is the transmission and A is the unit cell area (m2). The E-field intensity for monomers is evaluated 2 nm away from the NP surface along the E-field polarization axis. For the dimer it is evaluated in the center of the gap. The diffraction edges of the (0, 1), (1, 1), (0, 2), (1, 2) modes are included as red, yellow, white, and green lines, respectively. The unit cell geometries of corresponding arrays are shown on the right side of each row.

The LSPR energy of 2.19 eV for the monomer and 1.90 eV for the dimer are indicated in figure 3.12. In the investigated *k*-range the monomer LSPR (figure 3.12 (a)) interacts with the (0, 2), (1, 1), and (0, 1) Rayleigh anomalies. Once an in-plane diffracted order approaches the LSPR, increased extinction along the diffraction edge (below the peak LSPR energy) marks the onset of photonic-plasmonic coupling. The coupling enhances with increasing *k*, but finally the resonance detaches from the diffraction edge to converge against the LSPR wavelength. In case of the (0, 1) SLR, the *E*-field of the incident plane wave and the dipolar LSP mode responsible for the in-plane radiation have a parallel alignment, which results in a particularly efficient SLR excitation. We note in passing that the SLRs exhibit a spectrally sharp character for energies that are red-shifted relative to the LSPR and that the spectra gradually broaden as their energy approaches the LSPR. For energies higher than the LSPR energy, photonic and plasmonic modes cease to couple since for energetic reasons as well as for phase-match considerations (the phase of the plasmon in the individual NP monomer and dimers shifts by π when the frequency is scanned across the resonance), the plasmons do not excite SLRs above the LSPR energy.[113]

The extinction spectra of the dimer square array (figure 3.12(c)) show overall the same trends as the monomer but the longitudinal plasmon resonance is red-shifted to 1.89 eV due to plasmon hybridization.[11-12, 155-157] A noteworthy beneficial aspect of the resonance red-shift is that it is accompanied by a decrease in the imaginary part of the gold dielectric function, which results in a reduction of the dissipative losses in the metal.[131] A second anticipated result of the NP dimerization is a strong increase in the provided *E*-field enhancement due to plasmon coupling between the two NPs of the dimer.[3] The calculated peak *E*-field intensity enhancement spectra for the rectangular monomer (figure 3.12 (b)) and dimer (figure 3.12 (d)) arrays confirm that the *E*-field intensities in the dimer array are 2 orders of magnitude higher than in the monomer array. The simulations in figure 3.12 include the far- and near-field spectra of isolated NPs and dimers. A comparison of the near-field spectra of the isolated building blocks and the resulting peak *E*-field intensity enhancement in the arrays reveals that both collective mode formation and direct near-field coupling contribute to the *E*-field intensity enhancement in the dimer array. The array effect is, however, weaker than the clustering effect, which underlines the value of NP clusters as building block for plasmonic metasurfaces and arrays in which phase, amplitude, and powerflow can be varied through rational design of the array morphology.[14, 16, 22, 36, 119, 158]

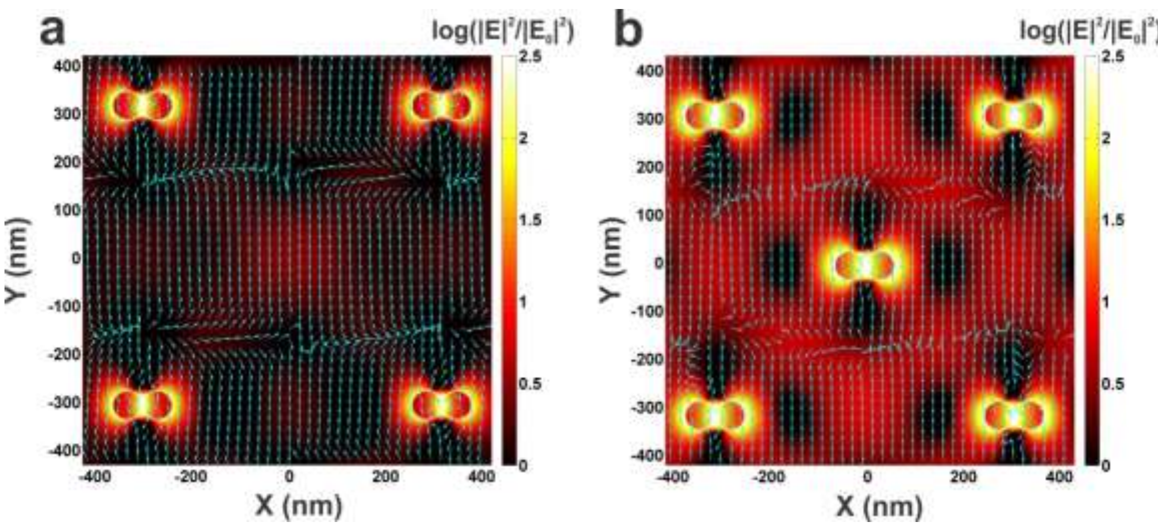

Figure 3.13. Electric field intensity enhancement map for the square array.

Electric field intensity enhancement map for the square array of (a) centered square array (b) of gold NP dimers. Normalized Poynting vectors are included as cyan arrows. All maps are evaluated with Λ = 623nm (k =1.01×10^{7} rad/m) and at an energy of 1.83eV.

In figure 3.13(a) we plot the *E*-field intensity enhancement map for the unit cell of the Λ = 623 nm (k =1.01×10^{7} rad/m) square array at the energy of the highest peak *E*-field enhancement (1.83eV). The *E*-field was evaluated in the equatorial plane of the metal

NPs. For *E*-field intensity enhancement maps at additional energies please refer to figure 3.15. The Bragg grating vector for the (1, 1) SLR in the square array is oriented along the xy-diagonal direction. The maps show that a resonant excitation of this mode creates *E*-field intensity enhancement not only at the location of the NP dimers but also weaker enhancement in the center of the square array unit cell. In the next step, we determined the impact of placing an additional dimer in this central position. Fig. 2(e) and f show the extinction and *E*-field intensity enhancement spectra for the resulting centered square (rhombic) array. The geometric transformation of the square array into a centered square array changes the geometric conditions for in-plane diffraction and the position of the diffraction edges (Fig. 7). In the *k*-range of interest the LSPR couples primarily to the (0, 1) Rayleigh anomaly (solid red line) of the centered square array. The integration of the additional NP dimer achieves an additional enhancement of the peak *E*-field intensity associated with the SLR by a factor of approximately 3. A map of the *E*-field intensity enhancement in the unit cell of the centered square array at 1.83 eV is included in Fig. 3(b). The addition of the new dimer does not only increase the peak *E*-field intensity enhancement in the gap junction between the NPs, but - consistent with the delocalized nature of the SLR - also enhances the *E*-field intensity in the lattice space between the dimers. We will analyze this effect in more details in the subsequent section.

3.3.3 Incorporation of dielectric NPs.

So far, we have limited our analysis to homogeneous arrays in which metal NPs or metal NP clusters provide both LSPRs as well as delocalized photonic modes due to diffractive coupling. The latter is, however, not unique to metal NP arrays. In fact, light trapping in dielectric NPs has less rigid requirements with regard to particle size and geometric array conditions.[159-160] Furthermore, dielectric NPs make it possible to avoid high dissipative losses in metal NPs at optical frequencies. However, dielectric NPs do not achieve the same level of light localization as is possible with metallic nanostructures, in particular, noble metal NP clusters. One approach to overcome this dilemma is to synergistically combine dielectric NPs and noble metallic NPs in one array in which the dielectric NPs define the grating and noble metal NP clusters provide efficient *E*-field localization.

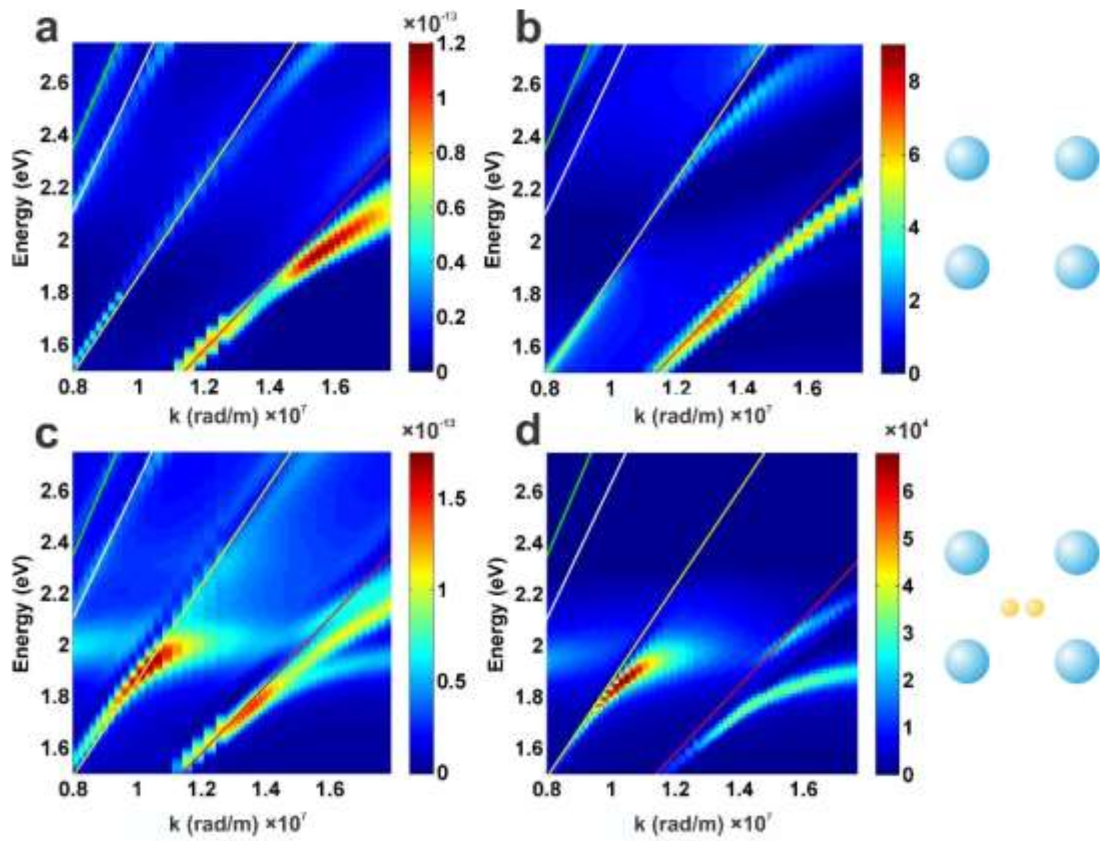

Figure 3.14. Extinction and E-field intensity enhancement diagram of dielectric NPs and hybrid arrays.

Extinction (a, c) and E-field intensity enhancement (b, d) spectra of square arrays of dielectric (n_r = 2.40) NPs (a, b) and metal-dielectric (c, d) hybrid array comprising both gold NP dimers and dielectric NPs. In the hybrid structure the *E*-field intensity was evaluated in the center gold NP dimer gap. In the dielectric array, the *E*-field intensity was evaluated in the center of the unit cell at the same z-coordinate as in the hybrid array. The diffraction edges of the (0, 1), (1, 1), (0, 2), (1, 2) modes are included as red, yellow, white, and green lines, respectively. The unit cell geometries of corresponding arrays are shown on the right side of each row.

We investigated the electromagnetic interactions in a hybrid array formed by a square array of 250 nm diameter dielectric NPs containing dimers of 60 nm gold NPs in the center of the unit cell (Fig. 4(c), (d)). The refractive index of the dielectric NPs was chosen as $n_r = 2.40$ to resemble TiO_2 NPs and the interparticle separation of the gold NPs was again 4 nm. We emphasize that similar geometries have already been experimentally realized through template guided self-assembly strategies.[67]

figure 3.14 contains the simulated extinction spectra for both the dielectric NP (figure 3.14a) and the metal-dielectric hybrid array (figure 3.14c) as function of *k*. The general structure of the dispersion diagram of the hybrid lattice in terms of the number and position of the diffraction edges resembles that of the regular square array. However, while the dielectric NP array exhibit extinction only along the edges of the various diffraction orders, the extinction spectrum of the hybrid array shows the formation of SLRs. Strikingly, the hybrid array contains electromagnetic features from two interdigitated square arrays with two sets of distinct lattice sites. Unlike for the metal NP arrays, the hybrid arrays shows extinction (albeit weaker) along the diffraction edge even for energies that lie above the LSPR energy due to contributions from the dielectric NP sub-array. Several features of the spectra indicate electromagnetic interactions between the metal and dielectric sub-arrays. For instance, in the hybrid array the extinction of the hybrid mode associated with the (1, 1) Rayleigh anomaly has gained in intensity compared to that associated with the (0, 1) Rayleigh anomaly, while in both the square array metal NP dimer (figure 3.12c) and the dielectric NP (figure 3.14a) array the (0, 1) mode is clearly the dominating feature. The propagation direction of the (1, 1) SLR in the hybrid array points along the dielectric – gold NP dimer diagonal, so that the light scattered into the array plane from high refractive index dielectric NPs achieves an effective excitation of the metal NP clusters. Interestingly, the extinction associated with the (0, 1) diffraction edge at energies above the gold LSPR energy is also noticeably higher in the hybrid array than in the corresponding all-dielectric NP array due to increased absorption in the array plane in the presence of the metal NPs.

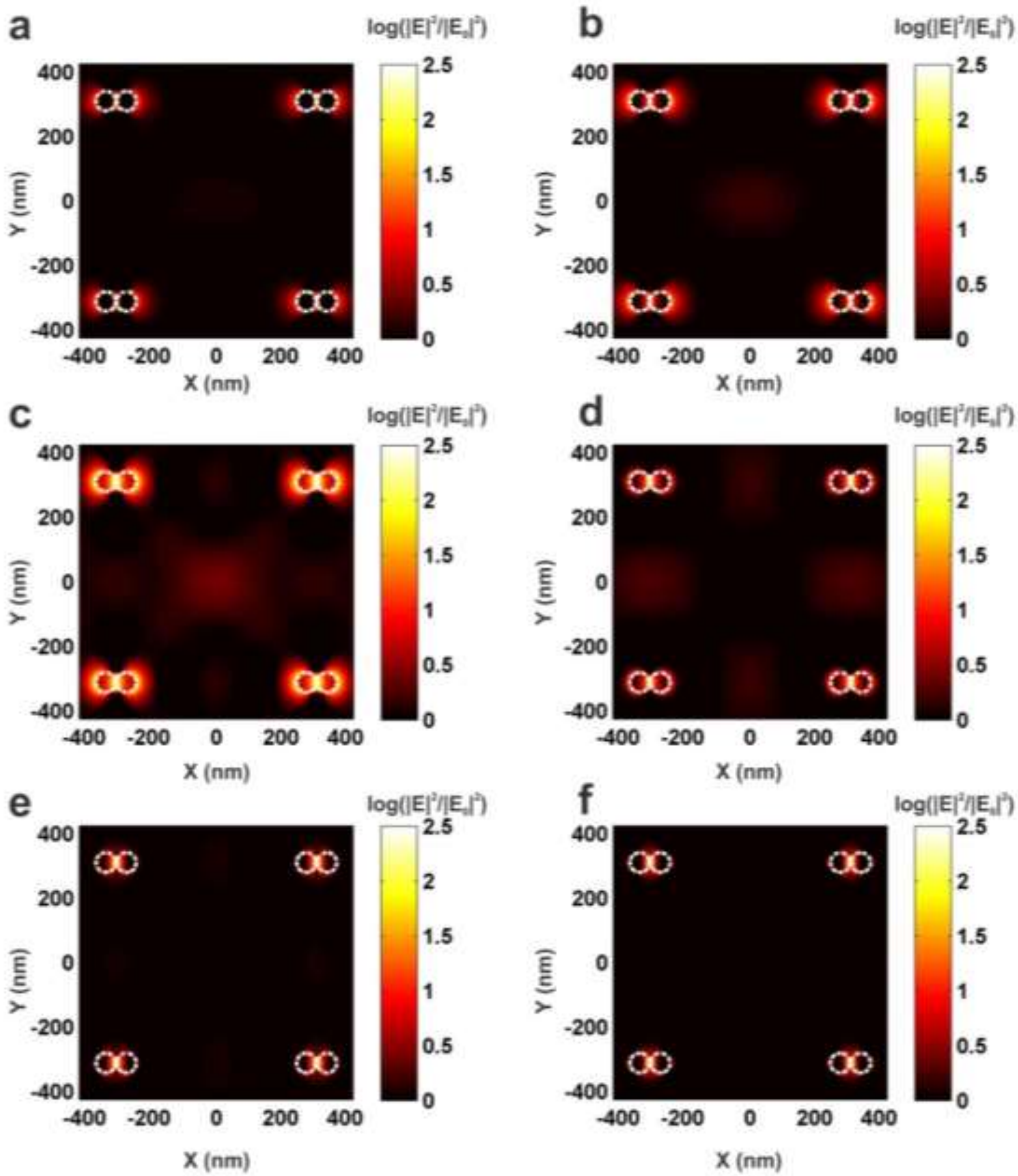

Figure 3.15. Electric field intensity enhancement map for the gold dimer array.

Electric field intensity enhancement map for the gold dimer array evaluated with Λ = 623nm (k =1.01×10^7 rad/m) at energy= (a)2.25eV, (b) 2.07eV, (c) 1.91eV, (d) 1.77eV, (e) 1.65eV, (e) 1.55eV.

In figure 3.14b and d we present the *E*-field intensity enhancement spectra as function of *k* for the dielectric NP square array and for the hybrid array. The photonic modes of the dielectric NP arrays generate only modest *E*-field intensity enhancements. This behavior changes dramatically upon integration of a NP dimer into the unit cell of the dielectric NP square array. The *E*-field intensity enhancement tracks the SLRs and the relative intensities are consistent with the far-field extinction data, in particular, the peak *E*-field intensity enhancement is overall higher for the (1, 1) hybrid mode than for the (0, 1) mode. Interestingly, the peak *E*-field intensity enhancement in the hybrid array is even higher than that of the centered square array of noble metal NP dimers in figure 3.12f. The gain in peak *E*-field enhancement in the hybrid array confirms a synergistic interplay between light trapping in the array plane through the high refractive index dielectric component and *E*-field enhancement provided by the plasmonic clusters.

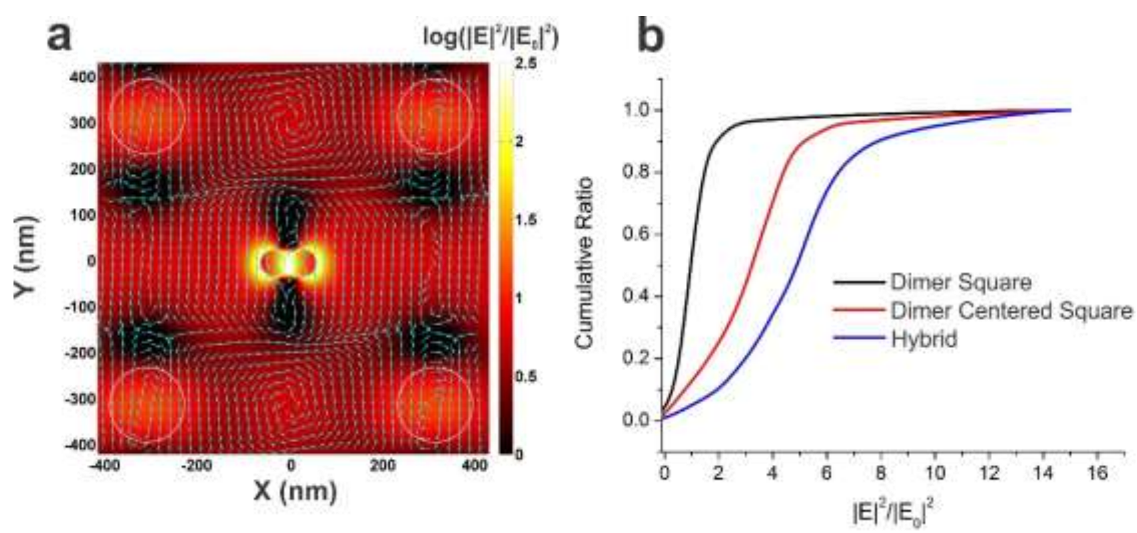

Figure 3.16. Electric field intensity distribution analysis for optoplasmonic array.

(a) Electric field intensity enhancement map and Poynting vector map for hybrid array. (b) Cumulative distribution plots of the E-field intensity in one unit cell for 3 types of array. All Figs. are evaluated with Λ = 623nm (k =1.01×10^7 rad/m) and energy=1.83eV.

Photonic-plasmonic coupling in hybrid arrays has benefits other than boosting the peak *E*-field intensity enhancement. figure 3.16a contains a map of the *E*-field intensity enhancement in the hybrid array unit cell with Λ = 623nm (k = 1.01×10^7 rad/m) at 1.83 eV (maps for additional energies are provided in figure. 3.17). While the peak *E*-field intensity enhancement is confined to the immediate vicinity of the gold NP dimer, the map shows increased enhancement of up to one order of magnitude in the array plane at locations remote from the metal NPs. Maximizing the *E*-field penetration in a large fraction of the ambient medium is highly desirable for many practical applications of plasmonic arrays and metasurfaces. In figure 3.16b we compare the cumulative distribution plots of the *E*-field intensity enhancement for the unit cells of the hybrid array, the NP dimer square array and the dimer centered square array for Λ = 623nm (k =1.01×10^7 rad/m) at 1.83 eV. In all three cases, we did not include the immediate vicinity of the metal NPs since our focus is here not on the hot-spots provided by the metal NPs but on the average *E*-field enhancement in the remaining unit cell. The distribution plots reveal that the average *E*-field enhancement throughout the entire unit cell is systematically higher in the hybrid array than in both gold NP dimer arrays. Considering that the hybrid arrays achieve higher *E*-field enhancement with half as many gold NPs as the centered square array, we conclude that the hybrid array is an effective design approach for boosting the *E*-field intensity in the ambient medium surrounding the integrated metal NPs.

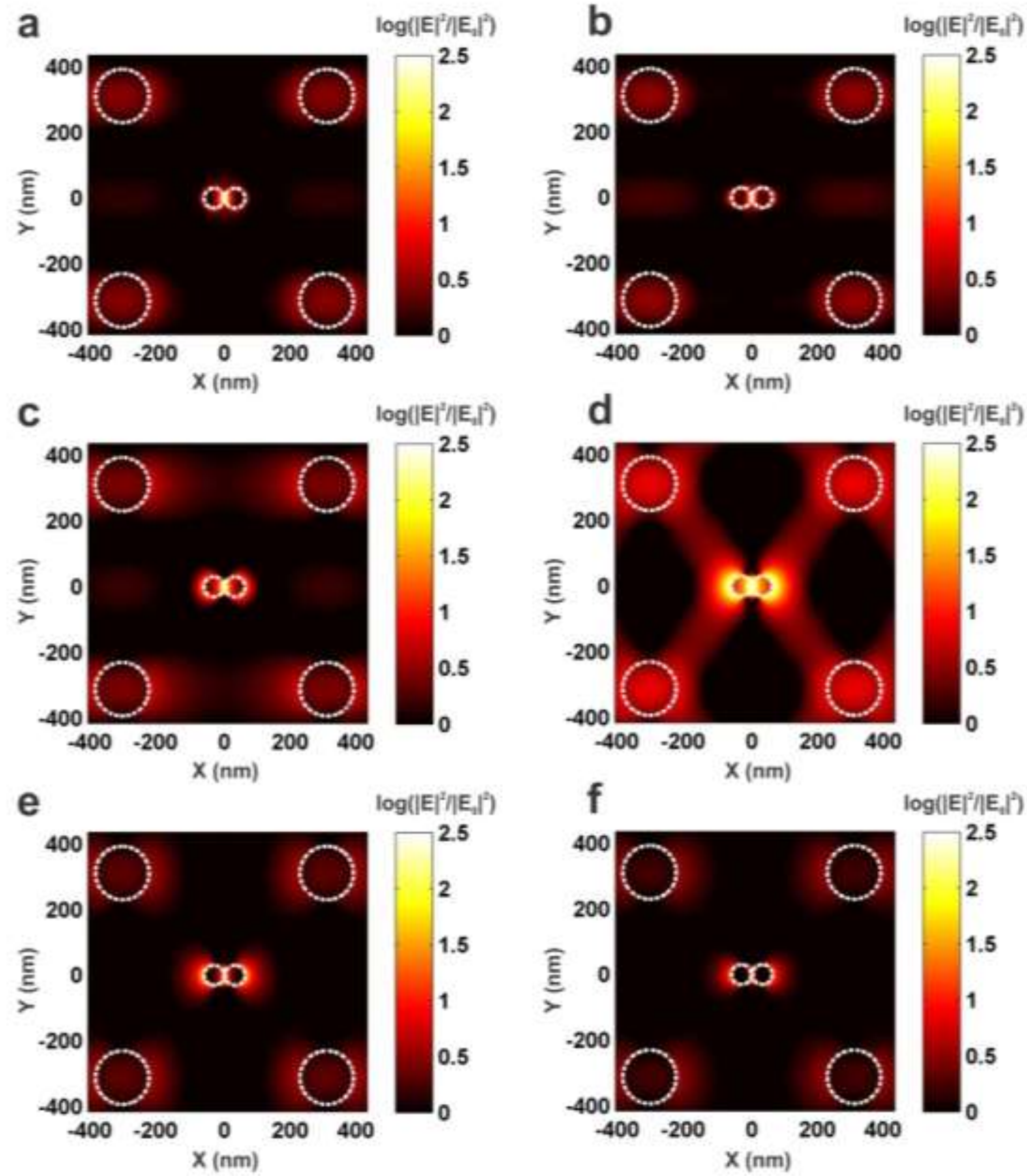

Figure. 3.17. Electric field intensity enhancement map for the hybrid array.

Electric field intensity enhancement map for the hybrid array evaluated with Λ = 623nm (k =1.01×10^{7} rad/m) at energy= (a)2.25eV, (b) 2.07eV, (c) 1.91eV, (d) 1.77eV, (e) 1.65eV, (e) 1.55eV.

3.3.4 Analysis of the energy flow in hybrid arrays.

In conventional metal NP arrays the control over spatial and spectral light intensity relies on interference, which is governed by the relative phase relationships between the different emitters in the array. In a grating of identical metal NPs, the array geometry, which determines the separation between individual particles, is the only parameter available to control phase relationships. Template-guided self-assembly strategies provide now the ability to include individual NPs or NP clusters with red-shifted resonance wavelengths, as well as NPs of different chemical composition (e.g. metal vs. dielectric) at pre-defined locations in one array.[67] The association level and chemical composition of the NPs influence the local resonance condition and, thus, the phase. This is important as the time-averaged Poynting vector $\boldsymbol{S} = \frac{1}{2}\,\mathrm{Re}[\boldsymbol{E} \times \boldsymbol{H}^*]$, which describes the optical powerflow density, is proportional to the phase gradient.[161-162] The impact of a change in the chemical composition on a subset of lattice sites on the optical powerflow is illustrated by comparing the Poynting vector maps for the centered rectangular gold NP dimer array (figure 3.13b) and the hybrid array (figure 3.16a). The Figs contain the Poynting vectors in the xy-plane of the unit cell for one selected grating period (Λ = 623nm, k =1.01×10^7 rad/m) and energy (1.83 eV) corresponding to the peak *E*-field intensity in the hybrid array. The replacement of the gold NP dimers on the edges of the unit cells with high refractive index dielectric NPs in the hybrid array has substantial effects on the Poynting vector map and leads to a much higher degree of topological complexity than observed in the gold NP dimer array. In particular, the hybrid array contains optical vortices around locations of destructive interference where the field intensity is zero and the phase, consequently, undetermined.[87, 163] Analogous locations of two-dimensional circulating optical powerflow are absent in the Poynting vector map of the metal dimer arrays in figure 3.13.

Our simulations show that hybrid NP arrays provide a viable approach for generating a high density of optical vortices with lateral dimensions of < 300 nm. The fact that some of these optical vortices exist outside of the NPs where they can interact with the ambient medium, makes this strategy very appealing for enhancing light-matter interactions through the circulating optical power in the vortex as well as for controlling the spatial distribution of amplitude and phase in the entire plane of the array. This gain in functionality could prove useful in future mixed metal-dielectric ("optoplasmonic") metasurfaces.

3.3.5 Conclusion

The coupling of in-plane diffracted photonic modes and LSPRs in regular arrays of noble metal NPs achieves the formation of photonic-plasmonic SLRs that generate a cascaded *E*-field enhancement in the vicinity of the NPs and – due to the contribution from delocalized photonic modes – an overall enhanced *E*-field intensity throughout the entire array. Different from cascaded *E*-field enhancement in discrete NP clusters,[164] the arrays of NP clusters investigated in this chapter sustain electromagnetic coupling interactions simultaneously on multiple length scales. With the continuing perfection of nanofabrication approaches, the structural complexity of electromagnetic materials continues to increase. It is now possible to integrate NPs of different association level and chemical composition into regular arrays.[16, 22, 36] In this chapter we have systematically investigated the impact of this compositional variability on the SLRs in two dimensional NP arrays assembled i.) from individual 60 nm diameter gold NPs, ii.) from dimers of electromagnetically strongly coupled NPs, and iii.) from both high refractive index dielectric NPs and gold NP dimers at separate lattice locations. Our simulations provide a vivid demonstration of the advantage of NP clusters (plasmonic metamolecules) over individual NPs as building blocks for arrays that maximize both peak and average *E*-field intensity. Interestingly, the combination of quasi loss-less dielectric NPs and gold NP dimers in one array can further enhance the *E*-field intensity at the plasmonic hot-spots and throughout the array. Furthermore, we have demonstrated that the ability to pattern the phase landscape through both the array morphology and the chemical composition at defined lattice sites provides important additional degrees of freedom for controlling the optical energy flow in two-dimensional arrays, which are absent in conventional arrays. We anticipate that the ability to pattern the phase and amplitude of optical fields in mixed metal-dielectric NP arrays will lead to new applications in photonics and plasmonics.

3.4 Directional emission through optoplasmonic arrays

3.4.1 Introduction

In free space, the radiation pattern of a dipole is characterized by a $\sin\theta^2$ distribution, where θ is the angle between the dipole oscillation axis and the observation direction. A donut-shaped radiation pattern is generated. But in practical experiments, emitter is often supported on dielectric interface. The photons emitted by a single molecule can scatter at the interface, thereby altering the molecule's emission pattern. The emission pattern of the emitter on top of a planner substrate is significantly perturbed.[165] For example, a dipole at glass-air interface will display emission lobes with most of the intensity going to the glass side.[166] To acquire the engineered emission pattern of emitters on substrate within nanometer scale, research groups have developed varied approaches. Plasmonic nano antennas [32, 167-168] and photonic crystals [169] are both promising candidates for manipulating the radiation directionality. The former display highly boosted emission via the local field enhancement and Purcell effect within nano cavities. The latter, as well known, can be designed to generate high Q factor in the optical cavity and sustain constructive interference or photonic bandgap guiding the emitted light into specific direction. Furthermore, Langguth [170] and Jun [171] have built up a 'plasmonic crystal' combining the merits of these materials. In their designed and realized structure, line-shaped or hole-shaped arrays were fabricated on the gold film, which will sustain surface plasmon polariton in the metal-dielectric interface. The dipole within the cavity emit and couple to the surface plasmon polariton. In Jun's study, a good fraction of the dipole emission first couples to gap SPPs and then 'spills' onto the surface in the form of planar SPPs. An engineered array of grooves are used to efficiently decouple the planar SPPs to form a beam with a narrow angular divergence. In Langguth's paper, besides an enhancement of local density of states in the central hole caused by Purcell effect, a coherent scattering from the surrounding hexagonal lattice holes drive the fluorescence emisstion pattern to be highly directed normal to the surface caused by the phased array behavior. The research over such antenna structures acts as a central role in many important applications, including optical spectroscopy techniques, biodetection, photochemistry and lighting.

3.4.2 Results and discussion

Inspired by the other established work, we proposed a directed emission in optoplasmonic hybrid array model to achieve an elevated degree of light-matter interaction within small scale. In our model, gold NP clusters serves as nano antennas providing small cavity to enhance the dipole emission. On the other hand, incorporated dielectric TiO_2 NPs (or other dielectric particles with higher refractive index) act as scattering component modifying the phase of emitted light and synergeticly guide the light, if designed appropriately, to collimated beam normal to the substrate surface. Although this phenomenon has already been observed in the structures introduced in former chapter, the pragmatic meaning of this optoplasmonic array is that self-assembly method will massively produce ordered structure with varied type of material under sub wavelength scale.

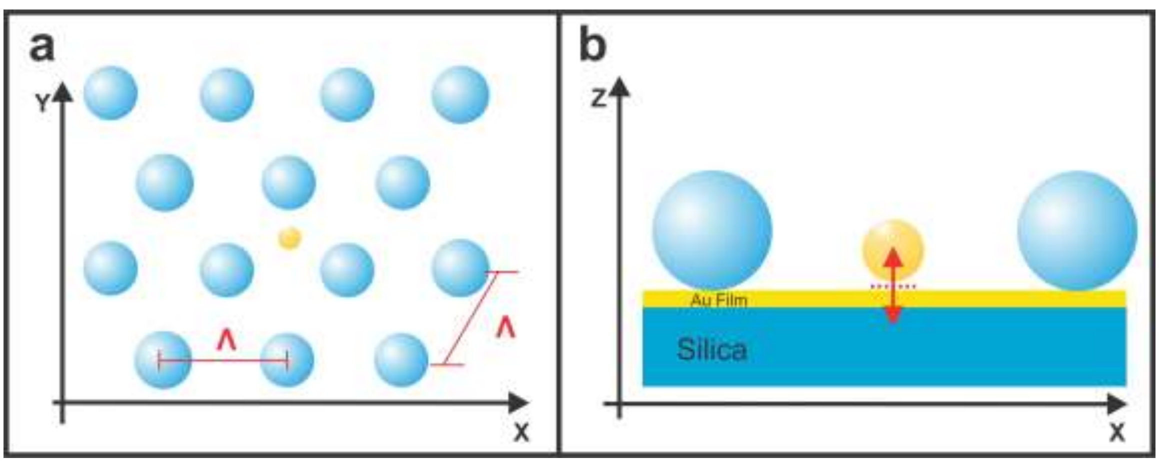

Figure 3.18. Illustration of optoplasmonic array model

(a) Top view of optoplasmonic array model, where blue TiO_2 NP are arranged in hexagonal lattice with spacing Λ. Yellow AuNP is located in the geometric center of surrounding TiO_2 NPs.(b) Side view of model, where red arrow denotes the dipole location and orientation. The Au film is with thickness =30nm.

We proposed a optoplasmonic hybrid array that integrate plasmonic antenna and dielectric NP phased array shown in figure 3.18. As we can see in figure 3.18a, the top view of the model, TiO2 NPs form hexagonal lattice and the gold NP is in the geometric center of three closest surrounding TiO_2 NPs. As shown in the side view in figure 3.18b, we can see that the dipole oscillates perpendicular to the substrate, which is a thin gold film on silica base. We choose this setup because we assume the emitter is excited via total internal reflection (TIF) and the near field enhancement of the dipole mode perpendicular to the plasmonic surface dominates all possible polarizations.[172-173] The orientation perpendicular to the surface increases the local density of state, i.e., the total decay rate to a maximum.[174] As a result, when excited, this model should display distinct emission intensity compared with the others. As well known, the lattice parameter Λ will determine the photonic property of the array when all the other components are determined. We build up models via FDTD computation seeking for lattice spacing with potentially beaming effect frequency matching the NP-film plamonic mode frequency. According to the work performed by Koenderink, an expected dispersion relation where modes cross the Γ-point (in a ω-k band diagram) at both the dye emission and SPP spectrum will be ideal. Also, in a system with finite interaction strength, one expects a red shift of the entire dispersion relation and the opening of a small stop gap at the edge of the Brillouin zone, which pushes the lower band edge further to the red.[170] Therefore, we will aim at the modes in our band diagram to cross in the lower energy side of 650 nm, where our Au NP cluster plasmon resonance lies.

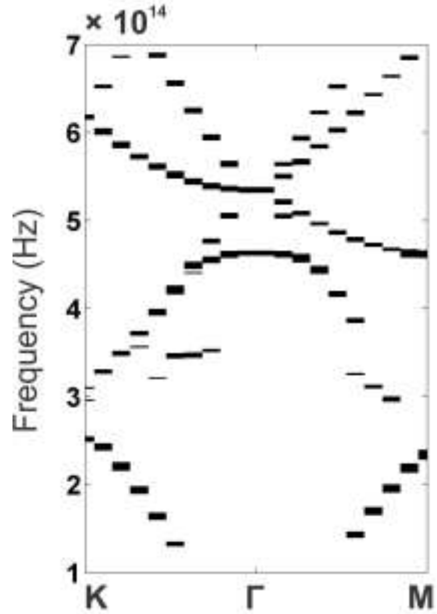

Figure 3.19 Band diagram of dispersion relation of a hexagonal TiO_2 NP 2D lattice with Λ = 650 nm.

Band diagram is obtained through dipole cloud in the photonic array and monitor modes within the structure. The modes crossed at Γ with frequency close to 4.7×10^{14} Hz ≈ 640 nm.

In figure 3.19 we show the dispersion relation of the hexagonal pure TiO_2 NP array. The Au NP is omitted because we are the TiO_2 NP lattice dominates the photonic environment. The modes cross at Γ with frequency close to 4.7×10^{14} Hz ≈ 640 nm, which is the desired range of our proposal. In the next step, we modeled the hybrid lattice by FDTD assuming the dipole is excited as the orientation shown in figure 3.18 and collect the emission profile in the farfield from the air side.

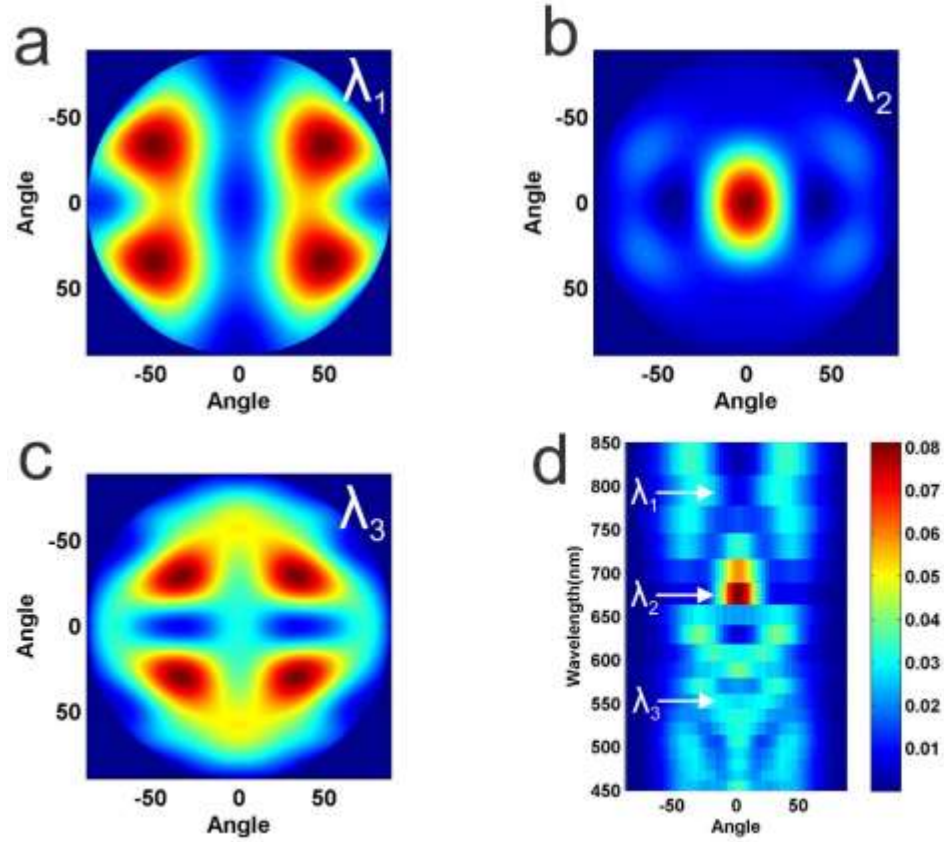

Figure 3.20 Dipole far field projection in the x-y plane of a modeled hexagonal optoplasmonic array with Λ = 650 nm.

Far field projection in the x-y plane of a modeled hexagonal optoplasmonic array with Λ = 650 nm at the wavelength (a)800 nm, (b)680 nm, (c)550 nm. (d)Emission diagram as a function of wavelength and angle. Corresponding wavelength for (a)-(c) are marked by arrow. Intensity are normalized by the sum emitted signal.

The far field projection with Λ = 650 nm at varied frequency is shown in figure 3.20a-c. In these plots, far field projection in x-y plane above the 2D lattice in the air side is mapped as function of polar emission angles. Λ = 650 is selected because the directed emission frequency lies in the range of AuNP-film plasmonic resonance. To simplify and make the plot more illustrative, we convert the x-y plane map into diagram (figure 3.20d) as a function of both emission angle and wavelength by summarizing all intensities with the same polar angle. We notice that at wavelength close to 680nm, the emission direction of the dipole in lattice is almost centered in the projection, i.e., perpendicular to the x-y plane. In contrast, at other wavelengths, such as 800 nm and 550 nm (figure 3.20a, c) signals are spread in the pattern more close to the AuNP-on-film model (figure 3.21). The introduced TiO_2 NP lattice decoupled the SPP propagating in the film and made the constructive interference in the direction of polar angle= 0 degree.

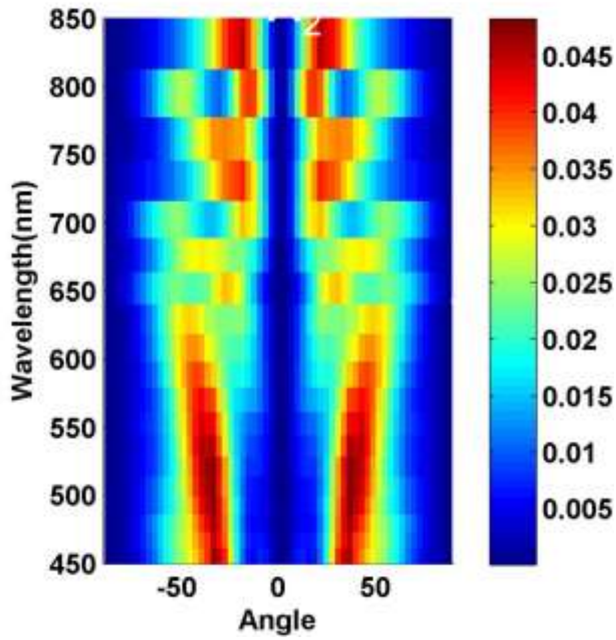

Figure 3.21 Dipole far field projection in the x-y plane of a modeled hexagonal Au NP array with Λ = 650 nm.

Far field emission diagram as a function of wavelength and angle in the x-y plane of a modeled hexagonal Au NP array.

Compared with radiation patterns in pure AuNP-film mode or the mode with same with same frequency but varied spacing parameters, the profile of the condition in figure 3.20b is highly directed. Meanwhile, the emission intensity is enhanced due to the elevated local density of states.

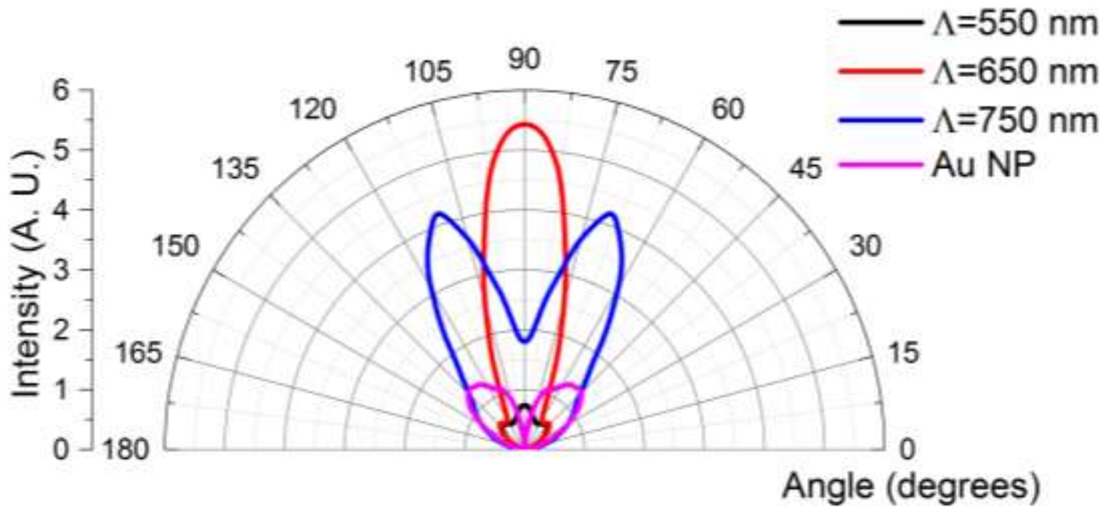

Figure 3.22 Dipole far field projection in the x-y plane of a modeled hexagonal Au NP array with Λ = 650 nm.

Far field emission diagram as a function of wavelength and angle in the x-y plane of a modeled hexagonal Au NP array.

3.4.3 Conclusion

Hybrid optoplasmonic array with phased hexagonal dilelctirc NP cooperating with plasmonic antenna display modified directionality. By adjusting the spacing parameter, we are able to shift the beaming frequency to overlap with plasmonic antenna resonance. The radiative emission rate of the dipole close to the antenna will get amplified because of increased local density of states. The emitted electromagnetic wave propagating along the Au film and scattered by the surrounding dielectric TiO_2 NPs, forming constructive interference in the perpendicular direction. The fabrication of such structure can be achieved utilizing the template guided self-assembly approach introduced in chapter 3, which can relatively create massive volume of optoplasmonic phased array. This directional emission strategy also benefits from additional degrees of freedom in varying the lattice parameters and materials. It’s promising in future nano devices involved in beam shaping. Such system serves as a scaffold for the engineering of spontaneous molecule emission.

APPENDIX

i. Calculation for the shift of diffraction edges

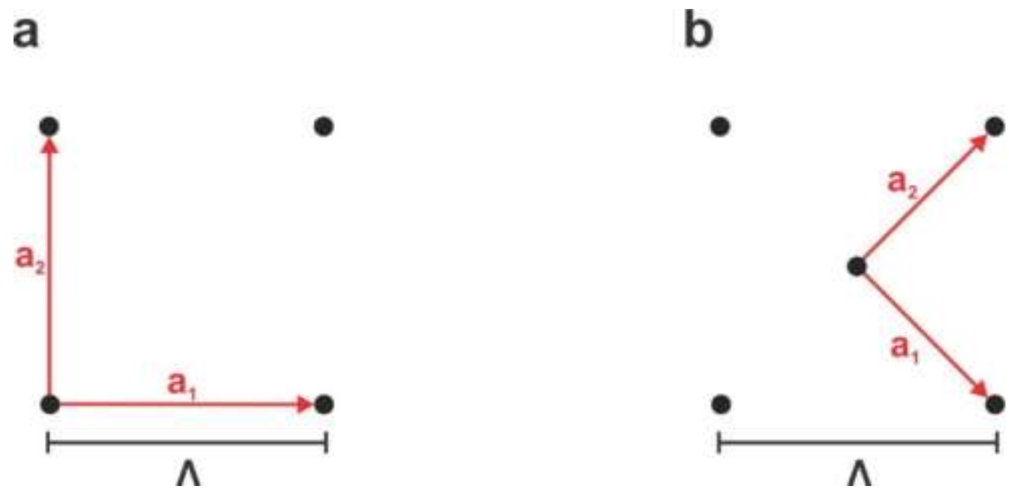

Fig. 7. Schematic real space of (a) square lattice and (b) rhombic lattice.

An in-plane propagation wave vector ***k*** can be written as $\boldsymbol{k} = \boldsymbol{k}_{\|} + \boldsymbol{G}$, where $\boldsymbol{k}_{\|}$ is the in-plane component of the incident wave vector ($\boldsymbol{k}_{\|} = \boldsymbol{k}_0 \sin(\theta)$; θ: incident polar angle). ***G*** is the Bragg grating vector. Because we choose the incident normal to the array plane, we have $\boldsymbol{k} = \boldsymbol{G} = i\boldsymbol{b}_1 + j\boldsymbol{b}_2$, where i, j are integers and $\boldsymbol{b}_1$ and $\boldsymbol{b}_2$ are reciprocal lattice vectors. The square lattice array has primitive lattice vectors $\boldsymbol{a}_1$ and $\boldsymbol{a}_2$ that can be expressed through unit vectors $\boldsymbol{n}_x$ and $\boldsymbol{n}_y$ oriented along the x- and y- axis, respectively.

$$\begin{cases} \boldsymbol{a}_1 = \Lambda \boldsymbol{n}_x \\ \boldsymbol{a}_2 = \Lambda \boldsymbol{n}_y \end{cases} \qquad (2)$$

We obtain the reciprocal lattice vectors $\boldsymbol{b}_1$ and $\boldsymbol{b}_2$ using the relationship $\boldsymbol{a}_i \cdot \boldsymbol{b}_j = 2\pi\delta_{ij}$:

$$\begin{cases} \boldsymbol{b}_1 = \dfrac{2\pi}{\Lambda} \boldsymbol{n}_x \\ \boldsymbol{b}_2 = \dfrac{2\pi}{\Lambda} \boldsymbol{n}_y \end{cases} \qquad (3)$$

As a result, when mode i=0, j=1 or (0, 1) is excited, we get $\boldsymbol{G} = \frac{2\pi}{\Lambda}\boldsymbol{n}_y$, which means that $\boldsymbol{k}$ points along the y-axis. If mode (1, 1) is excited, we get $\boldsymbol{G} = \frac{2\pi}{\Lambda}\boldsymbol{n}_x + \frac{2\pi}{\Lambda}\boldsymbol{n}_y$, which means $\boldsymbol{k}$ points along the xy diagonal.

For the rhombic array in Fig. 7(b), a similar treatment leads to the following expressions:

$$\begin{cases} \boldsymbol{b}_1 = \dfrac{\sqrt{2}\pi}{\Lambda}(\boldsymbol{n}_x - \boldsymbol{n}_y) \\ \boldsymbol{b}_2 = \dfrac{\sqrt{2}\pi}{\Lambda}(\boldsymbol{n}_x + \boldsymbol{n}_y) \end{cases} \qquad (4)$$

As shown in Fig. 7(b), when mode (0, 1) is excited $\boldsymbol{k}$ points along the xy direction with $\boldsymbol{k} = \boldsymbol{G} = \frac{\sqrt{2}\pi}{\Lambda}(\boldsymbol{n}_x + \boldsymbol{n}_y)$. When mode (1, 1) is excited, **k** points along the x axis with $\boldsymbol{k} = \boldsymbol{G} = \frac{2\sqrt{2}\pi}{\Lambda}\boldsymbol{n}_x$.

ii. Matlab code for radiation diagram

```
clear all

close all

widthx=301;

num_plot=20;

n=1;

step=1;% Adjust resolution

nstep=fix(89/step);

np=[1:step:(1+step*nstep),178-step*nstep:step:178];


[FileName,Fpath,Findex] = uigetfile('*.asc','MultiSelect', 'off' );

    temp1=(load(FileName));

    name1=FileName;

    load(name1, '-mat','Far_up','lamb');


 for i=1:num_plot

E2map(:,:,i)=(Far_up(:,:,i,m)+fliplr(Far_up(:,:,i,m)))/2;

 end

for i=1:length(lamb)

    [tempx,tempy]=FF2polar(E2map(:,:,i)); % FF2polar is function to convert

                                          % 2D farfield projection map

                                          % into 1-D curve as a function of
```

```
                                    % polar angle
    ny=sum(tempy);
    smoothx(:,n)= tempx(np(1,:));
    smoothy(:,n)= tempy(np(1,:)+0);
    imageY(:,i)=smoothy(:,n)./1;%unnormalized
    % imageY(:,i)=smoothy(:,n)./sum(smoothy(:,n));  %normalized
end
surface((smoothx(:,1)-pi/2).*180./pi,lamb(:,1)*1e9,imageY');
      shading flat
      colorbar
      colormap(jet)
      axis xy
      xlabel('Angle')
      ylabel('Wavelength(nm)')
      xlim([-90 90])
      ylim([450 850])
clear ('E2map_up','E2map','tempx','tempy');


%%Function FF2Polar


function [xdeg,c_polarY]=FF2polar(PolarMap1)
```

```
sttt=1; % width of angle

PolarY=zeros(178,1);

name1=strcat('angle_coordinates','.mat');   % connect names

load(name1, '-mat');


for i=1:sttt:89

areaArray(i,1)=2*pi*(cos((89.5-i)/180*pi)-cos((90.5-i)/180*pi));

end

for j=2:90

   kc=length(outputangles_posi{j,1});

   temp1=outputangles_posi{j,1};

   temp2=outputangles_nega{j,1};

   z1=0;

   z2=0;

   for i=1:kc

      z1=z1+(PolarMap1(temp1(i,1),temp1(i,2)));

      z2=z2+(PolarMap1(temp2(i,1),temp2(i,2)));

   end

   PolarY(91-j,1)=z1;  %% Polar(1,1) is 1 degree Polar(90,1) is 90 degree

   PolarY(88+j,1)=z2;

end

c_polarY=zeros(178,1);
```

```
c_polarY(1:89,1)=PolarY(1:89,1)./areaArray(1:89,1);
c_polarY(90:178,1)=PolarY(90:178,1)./areaArray(89:-1:1,1);
 for x=1:89  %generate x axis
  xdeg(x,1)= x/180*pi;
  xdeg(x+89,1)= (x+90)/180*pi;
 end
end

%% angle_coordinates.mat

clear all
widthx=301;
widthy=301;
sizehalf=(widthx+1)/2;
widthR=(widthx-1)/2; %radius

 for x=1:1:widthx  %generate x axis
 xdeg(x,1)= asin((x-sizehalf)/(sizehalf-1));
 end

azimuth=zeros(widthx,widthy);
polar=zeros(widthx,widthy);
```

```
r=zeros(widthx,widthy);
for j=1:widthy
   for i=1:widthx
      cart_x=i-(widthx+1)/2;
      cart_y=j-(widthy+1)/2;
    if cart_x*cart_x+cart_y*cart_y>widthR*widthR
        azimuth(i,j)=-1000;
        polar(i,j)=-1000;
        r(i,j)=-1000;
    else
       rr=sqrt(cart_x*cart_x+cart_y*cart_y);

        azimuth(i,j)=atan(cart_x/cart_y)/pi*180;
        polar(i,j)=asin(rr/widthR)/pi*180;  % in degrees
        r(i,j)=rr;
    end
   end
end

%For getting coorinates for specific polar and azi
outputangles_posi=cell(90,1);
outputangles_nega=cell(90,1);
```

```
for j=1:widthy
   for i=1:widthx
        for k=1:90   % separate by polar angle  1 to 90
            if (polar(i,j)>=(k-1.5))&(polar(i,j)<k-0.5)& ((i-(widthx+1)/2)>0)
               outputangles_posi{k,1}=cat(1,outputangles_posi{k,1},[i,j]);
            else if (polar(i,j)>=(k-1.5))&(polar(i,j)<k-0.5)&((i-(widthx+1)/2)<0)
               outputangles_nega{k,1}=cat(1,outputangles_nega{k,1},[i,j]);
               end
            end
        end
   end
end
save('angle_coordinates.mat','outputangles_posi','outputangles_nega','-mat');
```

iii. Matlab code for Poynting-Electric field map with adjustable resolution

```
clear all;
DataNum=1;   % select the frequency for display
lengthx=length(Ax);% X coordinate from Lumerical
lengthy=length(Ay);% Y coordinate from Lumerical
a=15; % step length, Poynting vector resolution
clims=[0 2.5];%Scale of value display
%%Poynting Vector
Px=real(PP(:,:,1,DataNum,1)); % must be reald
Py=real(PP(:,:,1,DataNum,2));
 for i=(1:(lengthx/a)) % sum gird
    for j=(1:(lengthy/a))
        PPx(i,j)=sum(sum(Px((i*a-a+1):(i*a),(j*a-a+1):(j*a))));
        PPy(i,j)=sum(sum(Py((i*a-a+1):(i*a),(j*a-a+1):(j*a))));
    end
end
for i=(1:lengthx/a)  %% normalize;  can be turnned off for unnormalized vecotr
    for j=(1:lengthy/a)
    Pxx(i,j)=PPx(i,j)/sqrt((PPx(i,j)^2+(PPy(i,j))^2));
    Pyy(i,j)=PPy(i,j)/sqrt((PPx(i,j)^2+(PPy(i,j))^2));
    end
end
```

```
for i=(1:lengthx/a) %New mesh grid
        New_x(i,1)=Ax(i*a-a/2+0.5)*1e9;
end
for j=(1:lengthy/a)
        New_y(j,1)=Ay(j*a-a/2+0.5)*1e9;
end

[X_final,Y_final]=meshgrid(New_x(1:lengthx/a,1),New_y(1:lengthy/a,1));
%%Emap
 imagesc(Ax*1e9,Ay*1e9,log10(Emap(:,:,1,DataNum)'),clims);
    axis xy
    set(gca,'DataAspectRatio',[1 1 1]);
    colormap(hot)
    colorbar
    shading interp
    hold on
 h= quiver(X_final,Y_final,Pxx,Pyy,'color','c','linewidth',1,'autoscalefactor',0.8);
    set(h,'MaxHeadSize',50)
    xlabel('X(nm)');
    ylabel('Y(nm)');
```

BIBLIOGRAPHY

(1) Maier, S. A. Plasmonics: Fundamentals and Applications: Fundamentals and Applications. Springer: 2007.

(2) Mayer, K. M.; Hafner, J. H. Localized Surface Plasmon Resonance Sensors. Chemical reviews **2011,** 111, 3828-3857.

(3) Jain, P. K.; El-Sayed, M. A. Plasmonic Coupling in Noble Metal Nanostructures. Chemical Physics Letters **2010,** 487, 153-164.

(4) Baffou, G.; Girard, C.; Quidant, R. Mapping Heat Origin in Plasmonic Structures. Physical Review Letters **2010,** 104, 136805.

(5) Sanchot, A.; Baffou, G.; Marty, R.; Arbouet, A.; Quidant, R.; Girard, C.; Dujardin, E. Plasmonic Nanoparticle Networks for Light and Heat Concentration. ACS Nano **2012,** 6, 3434-3440.

(6) Murphy, C. J.; Sau, T. K.; Gole, A. M.; Orendorff, C. J.; Gao, J.; Gou, L.; Hunyadi, S. E.; Li, T. Anisotropic Metal Nanoparticles: Synthesis, Assembly, and Optical Applications. The Journal of Physical Chemistry B **2005,** 109, 13857-13870.

(7) Lohse, S. E.; Murphy, C. J. The Quest for Shape Control: A History of Gold Nanorod Synthesis. Chemistry of Materials **2013,** 25, 1250-1261.

(8) Wang, H.; Brandl, D. W.; Le, F.; Nordlander, P.; Halas, N. J. Nanorice: A Hybrid Plasmonic Nanostructure. Nano Letters **2006,** 6, 827-832.

(9) Cobley, C. M.; Skrabalak, S. E.; Campbell, D. J.; Xia, Y. Shape-Controlled Synthesis of Silver Nanoparticles for Plasmonic and Sensing Applications. Plasmonics **2009,** 4, 171-179.

(10) Gunnarsson, L.; Rindzevicius, T.; Prikulis, J.; Kasemo, B.; Käll, M.; Zou, S.; Schatz, G. C. Confined Plasmons in Nanofabricated Single Silver Particle Pairs: Experimental Observations of Strong Interparticle Interactions. The Journal of Physical Chemistry B **2005,** 109, 1079-1087.

(11) Nordlander, P.; Oubre, C.; Prodan, E.; Li, K.; Stockman, M. Plasmon Hybridization in Nanoparticle Dimers. Nano Letters **2004,** 4, 899-903.

(12) Jain, P. K.; Huang, W. Y.; El-Sayed, M. A. On the Universal Scaling Behavior of the Distance Decay of Plasmon Coupling in Metal Nanoparticle Pairs: A Plasmon Ruler Equation. Nano Letters **2007,** 7, 2080-2088.

(13) Funston, A. M.; Novo, C.; Davis, T. J.; Mulvaney, P. Plasmon Coupling of Gold Nanorods at Short Distances and in Different Geometries. Nano Letters **2009,** 9, 1651-1658.

(14) Fan, J. A.; Wu, C.; Bao, K.; Bao, J.; Bardhan, R.; Halas, N. J.; Manoharan, V. N.; Nordlander, P.; Shvets, G.; Capasso, F. Self-Assembled Plasmonic Nanoparticle Clusters. Science **2010,** 328, 1135-1138.

(15) Storhoff, J. J.; Lazarides, A. A.; Mucic, R. C.; Mirkin, C. A.; Letsinger, R. L.; Schatz, G. C. What Controls the Optical Properties of DNA-Linked Gold Nanoparticle Assemblies? Journal of the American Chemical Society **2000,** 122, 4640-4650.

(16) Yan, B.; Boriskina, S. V.; Reinhard, B. M. Design and Implementation of Noble Metal Nanoparticle Cluster Arrays for Plasmon Enhanced Biosensing. Journal of Physical Chemistry C **2011,** 115, 24437-24453.

(17) Shegai, T.; Chen, S.; Miljković, V. D.; Zengin, G.; Johansson, P.; Käll, M. A Bimetallic Nanoantenna for Directional Colour Routing. Nature communications **2011,** 2, 481.

(18) Shegai, T.; Li, Z.; Dadosh, T.; Zhang, Z.; Xu, H.; Haran, G. Managing Light Polarization Via Plasmon–Molecule Interactions within an Asymmetric Metal Nanoparticle Trimer. Proceedings of the National Academy of Sciences **2008,** 105, 16448-16453.

(19) Koechlin, C.; Bouchon, P.; Pardo, F.; Jaeck, J.; Lafosse, X.; Pelouard, J.-L.; Haïdar, R. Total Routing and Absorption of Photons in Dual Color Plasmonic Antennas. Applied Physics Letters **2011,** 99, 241104.

(20) Hao, E.; Schatz, G. C. Electromagnetic Fields around Silver Nanoparticles and Dimers. The Journal of chemical physics **2004,** 120, 357-366.

(21) Lal, S.; Grady, N. K.; Goodrich, G. P.; Halas, N. J. Profiling the near Field of a Plasmonic Nanoparticle with Raman-Based Molecular Rulers. Nano Letters **2006,** 6, 2338-2343.

(22) Yan, B.; Boriskina, S. V.; Reinhard, B. M. Optimizing Gold Nanoparticle Cluster Configurations (N≤7) for Array Applications. The Journal of Physical Chemistry C **2011,** 115, 4578-4583.

(23) Schnell, M.; Garcia-Etxarri, A.; Huber, A.; Crozier, K.; Aizpurua, J.; Hillenbrand, R. Controlling the near-Field Oscillations of Loaded Plasmonic Nanoantennas. Nature Photonics **2009,** 3, 287-291.

(24) Prasad, J.; Zins, I.; Branscheid, R.; Becker, J.; Koch, A. H.; Fytas, G.; Kolb, U.; Sönnichsen, C. Plasmonic Core–Satellite Assemblies as Highly Sensitive Refractive Index Sensors. The Journal of Physical Chemistry C **2015,** 119, 5577-5582.

(25) König, T.; Kodiyath, R.; Combs, Z. A.; Mahmoud, M.; El‐Sayed, M. A.; Tsukruk, V. V. Silver Nanocube Aggregates in Cylindrical Pores for Higher Refractive Index Plasmonic Sensing. Particle & Particle Systems Characterization **2014,** 31, 274-283.

(26) Yan, B.; Thubagere, A.; Premasiri, W. R.; Ziegler, L. D.; Dal Negro, L.; Reinhard, B. M. Engineered Sers Substrates with Multiscale Signal Enhancement: Nanoparticle Cluster Arrays. ACS Nano **2009,** 3, 1190-1202.

(27) Ye, J.; Wen, F.; Sobhani, H.; Lassiter, J. B.; Dorpe, P. V.; Nordlander, P.; Halas, N. J. Plasmonic Nanoclusters: Near Field Properties of the Fano Resonance Interrogated with Sers. Nano Letters **2012,** 12, 1660-1667.

(28) Pazos‐Perez, N.; Wagner, C. S.; Romo‐Herrera, J. M.; Liz‐Marzán, L. M.; García de Abajo, F. J.; Wittemann, A.; Fery, A.; Alvarez‐Puebla, R. A. Organized Plasmonic Clusters with High Coordination Number and Extraordinary Enhancement in Surface‐Enhanced Raman Scattering (Sers). Angewandte Chemie International Edition **2012,** 51, 12688-12693.

(29) Farahani, J. N.; Pohl, D. W.; Eisler, H.-J.; Hecht, B. Single Quantum Dot Coupled to a Scanning Optical Antenna: A Tunable Superemitter. Physical Review Letters **2005,** 95, 017402.

(30) Anger, P.; Bharadwaj, P.; Novotny, L. Enhancement and Quenching of Single-Molecule Fluorescence. Physical Review Letters **2006,** 96, 113002.

(31) Muskens, O. L.; Giannini, V.; Sanchez-Gil, J. A.; Gomez Rivas, J. Strong Enhancement of the Radiative Decay Rate of Emitters by Single Plasmonic Nanoantennas. Nano Letters **2007,** 7, 2871-2875.

(32) Curto, A. G.; Volpe, G.; Taminiau, T. H.; Kreuzer, M. P.; Quidant, R.; van Hulst, N. F. Unidirectional Emission of a Quantum Dot Coupled to a Nanoantenna. Science **2010,** 329, 930-933.

(33) Mastroianni, A. J.; Claridge, S. A.; Alivisatos, A. P. Pyramidal and Chiral Groupings of Gold Nanocrystals Assembled Using DNA Scaffolds. Journal of the American Chemical Society **2009,** 131, 8455-8459.

(34) Kim, J.-Y.; Lee, J.-S. Synthesis and Thermally Reversible Assembly of DNA−Gold Nanoparticle Cluster Conjugates. Nano Letters **2009,** 9, 4564-4569.

(35) Tian, Y.; Wang, T.; Liu, W.; Xin, H. L.; Li, H.; Ke, Y.; Shih, W. M.; Gang, O. Prescribed Nanoparticle Cluster Architectures and Low-Dimensional Arrays Built Using Octahedral DNA Origami Frames. Nature nanotechnology **2015**.

(36) Yang, L.; Yan, B.; Premasiri, R. W.; Ziegler, L. D.; Dal Negro, L.; Reinhard, B. M. Engineering Nanoparticle Cluster Arrays for Bacterial Biosensing: The Role of the Building Block in Multiscale Sers Substrates. Advanced Functional Materials **2010,** 20, 2619-2628.

(37) Zou, S.; Schatz, G. C. Narrow Plasmonic/Photonic Extinction and Scattering Line Shapes for One and Two Dimensional Silver Nanoparticle Arrays. The Journal of chemical physics **2004,** 121, 12606-12612.

(38) Zou, S.; Janel, N.; Schatz, G. C. Silver Nanoparticle Array Structures That Produce Remarkably Narrow Plasmon Lineshapes. The Journal of chemical physics **2004,** 120, 10871-10875.

(39) Winkleman, A.; Gates, B. D.; McCarty, L. S.; Whitesides, G. M. Directed Self‐Assembly of Spherical Particles on Patterned Electrodes by an Applied Electric Field. Advanced Materials **2005,** 17, 1507-1511.

(40) Yin, Y.; Lu, Y.; Gates, B.; Xia, Y. Template-Assisted Self-Assembly: A Practical Route to Complex Aggregates of Monodispersed Colloids with Well-Defined Sizes, Shapes, and Structures. Journal of the American Chemical Society **2001,** 123, 8718-8729.

(41) Xia, Y.; Yin, Y.; Lu, Y.; McLellan, J. Template-Assisted Self-Assembly of Spherical Colloids into Complex and Controllable Structures. Advanced Functional Materials **2003,** 13, 907-918.

(42) Zhang, J.; Li, Y.; Zhang, X.; Yang, B. Colloidal Self‐Assembly Meets Nanofabrication: From Two‐Dimensional Colloidal Crystals to Nanostructure Arrays. Advanced Materials **2010,** 22, 4249-4269.

(43) Chou, S. Y.; Krauss, P. R.; Renstrom, P. J. Nanoimprint Lithography. Journal of Vacuum Science & Technology B **1996,** 14, 4129-4133.

(44) Chou, S. Y.; Krauss, P. R. Imprint Lithography with Sub-10 Nm Feature Size and High Throughput. Microelectronic Engineering **1997,** 35, 237-240.

(45) Yablonovitch, E. Photonic Band-Gap Structures. JOSA B **1993,** 10, 283-295.

(46) Velikov, K. P.; Moroz, A.; van Blaaderen, A. Photonic Crystals of Core-Shell Colloidal Particles. Applied Physics Letters **2002,** 80, 49-51.

(47) Joannopoulos, J. D.; Johnson, S. G.; Winn, J. N.; Meade, R. D. Photonic Crystals: Molding the Flow of Light. Princeton university press: 2011.

(48) Ye, Y.-H.; LeBlanc, F.; Haché, A.; Truong, V.-V. Self-Assembling Three-Dimensional Colloidal Photonic Crystal Structure with High Crystalline Quality. Applied Physics Letters **2001,** 78, 52-54.

(49) Vlasov, Y. A.; Bo, X.-Z.; Sturm, J. C.; Norris, D. J. On-Chip Natural Assembly of Silicon Photonic Bandgap Crystals. Nature **2001,** 414, 289-293.

(50) Baffou, G.; Quidant, R.; Girard, C. Heat Generation in Plasmonic Nanostructures: Influence of Morphology. Applied Physics Letters **2009,** 94, 153109.

(51) Ou, J.-Y.; Plum, E.; Zhang, J.; Zheludev, N. I. In Controlling Light with Light in a Plasmonic Nanooptomechanical Metamaterial, CLEO: Science and Innovations, Optical Society of America: 2014; p SF1M. 1.

(52) Koenderink, A. F. On the Use of Purcell Factors for Plasmon Antennas. Optics Letters **2010,** 35, 4208-4210.

(53) Gramotnev, D. K.; Bozhevolnyi, S. I. Plasmonics Beyond the Diffraction Limit. Nature Photonics **2010,** 4, 83-91.

(54) Dulkeith, E.; Morteani, A.; Niedereichholz, T.; Klar, T.; Feldmann, J.; Levi, S.; Van Veggel, F.; Reinhoudt, D.; Möller, M.; Gittins, D. Fluorescence Quenching of Dye Molecules near Gold Nanoparticles: Radiative and Nonradiative Effects. Physical Review Letters **2002,** 89, 203002.

(55) Zhu, J.; Ozdemir, S. K.; Xiao, Y.-F.; Li, L.; He, L.; Chen, D.-R.; Yang, L. On-Chip Single Nanoparticle Detection and Sizing by Mode Splitting in an Ultrahigh-Q Microresonator. Nature Photonics **2010,** 4, 46-49.

(56) Noda, S.; Chutinan, A.; Imada, M. Trapping and Emission of Photons by a Single Defect in a Photonic Bandgap Structure. Nature **2000,** 407, 608-610.

(57) Hood, C.; Lynn, T.; Doherty, A.; Parkins, A.; Kimble, H. The Atom-Cavity Microscope: Single Atoms Bound in Orbit by Single Photons. Science **2000,** 287, 1447-1453.

(58) Barth, M.; Schietinger, S.; Fischer, S.; Becker, J.; Nusse, N.; Aichele, T.; Lochel, B.; Sonnichsen, C.; Benson, O. Nanoassembled Plasmonic-Photonic Hybrid Cavity for Tailored Light-Matter Coupling. Nano Letters **2010,** 10, 891-895.

(59) Shopova, S. I.; Rajmangal, R.; Holler, S.; Arnold, S. Plasmonic Enhancement of a Whispering-Gallery-Mode Biosensor for Single Nanoparticle Detection. Applied Physics Letters **2011,** 98, 243104-3.

(60) Santiago-Cordoba, M. A.; Boriskina, S. V.; Vollmer, F.; Demirel, M. C. Nanoparticle-Based Protein Detection by Optical Shift of a Resonant Microcavity. Applied Physics Letters **2011,** 99, 073701-3.

(61) Murai, S.; Verschuuren, M.; Lozano, G.; Pirruccio, G.; Rodriguez, S.; Rivas, J. G. Hybrid Plasmonic-Photonic Modes in Diffractive Arrays of Nanoparticles Coupled to Light-Emitting Optical Waveguides. Optics Express **2013,** 21, 4250-4262.

(62) Frimmer, M.; Koenderink, A. F. Spontaneous Emission Control in a Tunable Hybrid Photonic System. Physical Review Letters **2013,** 110, 217405.

(63) De Angelis, F.; Patrini, M.; Das, G.; Maksymov, I.; Galli, M.; Businaro, L.; Andreani, L. C.; Di Fabrizio, E. A Hybrid Plasmonic− Photonic Nanodevice for Label-Free Detection of a Few Molecules. Nano Letters **2008,** 8, 2321-2327.

(64) Gartia, M. R.; Seo, S.; Kim, J.; Chang, T.-W.; Bahl, G.; Lu, M.; Liu, G. L.; Eden, J. G. Injection-Seeded Optoplasmonic Amplifier in the Visible. Scientific reports **2014,** 4.

(65) Mukherjee, I.; Hajisalem, G.; Gordon, R. One-Step Integration of Metal Nanoparticle in Photonic Crystal Nanobeam Cavity. Optics Express **2011,** 19, 22462-22469.

(66) Ahn, W.; Boriskina, S. V.; Hong, Y.; Reinhard, B. M. Photonic–Plasmonic Mode Coupling in on-Chip Integrated Optoplasmonic Molecules. ACS Nano **2012,** 6, 951-960.

(67) Hong, Y.; Qiu, Y.; Chen, T.; Reinhard, B. M. Rational Assembly of Optoplasmonic Hetero‐Nanoparticle Arrays with Tunable Photonic‐Plasmonic Resonances. Advanced Functional Materials **2014,** 24, 739-746.

(68) Hong, Y.; Pourmand, M.; Boriskina, S. V.; Reinhard, B. M. Enhanced Light Focusing in Self-Assembled Optoplasmonic Clusters with Subwavelength Dimensions. Advanced Materials **2013,** 25, 115-119.

(69) Garnett, J. M. Colours in Metal Glasses, in Metallic Films, and in Metallic Solutions. Ii. Philosophical Transactions of the Royal Society of London. Series A, Containing Papers of a Mathematical or Physical Character **1906**, 237-288.

(70) Mie, G. Beiträge Zur Optik Trüber Medien, Speziell Kolloidaler Metallösungen. Annalen der physik **1908,** 330, 377-445.

(71) Purcell, E. M.; Pennypacker, C. R. Scattering and Absorption of Light by Nonspherical Dielectric Grains. The Astrophysical Journal **1973,** 186, 705-714.

(72) Myroshnychenko, V.; Rodríguez-Fernández, J.; Pastoriza-Santos, I.; Funston, A. M.; Novo, C.; Mulvaney, P.; Liz-Marzán, L. M.; de Abajo, F. J. G. Modelling the Optical Response of Gold Nanoparticles. Chemical Society Reviews **2008,** 37, 1792-1805.

(73) de Abajo, F. G.; Howie, A. Relativistic Electron Energy Loss and Electron-Induced Photon Emission in Inhomogeneous Dielectrics. Physical Review Letters **1998,** 80, 5180.

(74) Taflove, A.; Hagness, S. C. Computational Electrodynamics: The Finite-Difference Time-Domain Method. Norwood, 2nd Edition, MA: Artech House, l995 **1995**.

(75) Yee, K. S. Numerical Solution of Initial Boundary Value Problems Involving Maxwell's Equations in Isotropic Media. IEEE Trans. Antennas Propag **1966,** 14, 302-307.

(76) Mackowski, D. W. Calculation of Total Cross Sections of Multiple-Sphere Clusters. JOSA A **1994,** 11, 2851-2861.

(77) Bohren, C. F.; Huffman, D. R. Absorption and Scattering of Light by Small Particles. John Wiley & Sons: 2008.

(78) Mackowski, D. W.; Mishchenko, M. I. Calculation of the T Matrix and the Scattering Matrix for Ensembles of Spheres. JOSA A **1996,** 13, 2266-2278.

(79) Grandidier, J.; Callahan, D. M.; Munday, J. N.; Atwater, H. A. Light Absorption Enhancement in Thin-Film Solar Cells Using Whispering Gallery Modes in Dielectric Nanospheres. Advanced Materials **2011,** 23, 1272-1276.

(80) Cole, R.; Sugawara, Y.; Baumberg, J.; Mahajan, S.; Abdelsalam, M.; Bartlett, P. Easily Coupled Whispering Gallery Plasmons in Dielectric Nanospheres Embedded in Gold Films. Physical Review Letters **2006,** 97, 137401.

(81) Romanov, S. G.; Korovin, A. V.; Regensburger, A.; Peschel, U. Hybrid Colloidal Plasmonic-Photonic Crystals. Advanced Materials **2011,** 23, 2515-2533.

(82) Galisteo-Lopez, J. F.; Lopez-Garcia, M.; Lopez, C.; Garcia-Martin, A. Intrinsic Losses in Self-Assembled Hybrid Metallodielectric Systems. Applied Physics Letters **2011,** 99, 083302-3.

(83) Benson, O. Assembly of Hybrid Photonic Architectures from Nanophotonic Constituents. Nature **2011,** 480, 193-199.

(84) Yang, X.; Ishikawa, A.; Yin, X.; Zhang, X. Hybrid Photonic−Plasmonic Crystal Nanocavities. ACS Nano **2011,** 5, 2831-2838.

(85) Ozbay, E. Plasmonics: Merging Photonics and Electronics at Nanoscale Dimensions. Science **2006,** 311, 189-193.

(86) Boriskina, S. V.; Reinhard, B. M. Spectrally and Spatially Configurable Superlenses for Optoplasmonic Nanocircuits. Proceedings of the National Academy of Sciences of the United States of America **2011,** 108, 3147-3151.

(87) Boriskina, S. V.; Reinhard, B. M. Adaptive on-Chip Control of Nano-Optical Fields with Optoplasmonic Vortex Nanogates. Optics Express **2011,** 19, 22305-22315.

(88) Haddadpour, A.; Yi, Y. Metallic Nanoparticle on Micro Ring Resonator for Bio Optical Detection and Sensing. Biomedical Optics Express **2010,** 1, 378-384.

(89) Devilez, A.; Stout, B.; Bonod, N. Compact Metallo-Dielectric Optical Antenna for Ultra Directional and Enhanced Radiative Emission. ACS Nano **2010,** 4, 3390-3396.

(90) Xiao, Y.-F.; Liu, Y.-C.; Li, B.-B.; Chen, Y.-L.; Li, Y.; Gong, Q. Strongly Enhanced Light-Matter Interaction in a Hybrid Photonic-Plasmonic Resonator. Physical Review A **2012,** 85, 031805.

(91) Lumerical Solutions, Inc. *Http://Www.Lumerical.Com/*.

(92) Johnson, P. B.; Christy, R. W. Optical Constants of the Noble Metals. Physical Review B **1972,** 6, 4370-4379.

(93) Yokota, T.; ARAi, N.; Lee, F.; Rennick, D.; Mosmann, T.; Arai, K.-I. Use of a Cdna Expression Vector for Isolation of Mouse Interleukin 2 Cdna Clones: Expression of T-Cell Growth-Factor Activity after Transfection of Monkey Cells. Proceedings of the National Academy of Sciences **1985,** 82, 68-72.

(94) Mott, H. R.; Driscoll, P. C.; Boyd, J.; Cooke, R. M.; Weir, M. P.; Campbell, I. D. Secondary Structure of Human Interleukin 2 from 3d Heteronuclear Nmr Experiments. Biochemistry **1992,** 31, 7741-7744.

(95) Berktas, M.; Guducuoglu, H.; Bozkurt, H.; Onbasi, K.; Kurtoglu, M.; Andic, S. Change in Serum Concentrations of Interleukin-2 and Interferon-Γ During Treatment of Tuberculosis. Journal of international medical research **2004,** 32, 324-330.

(96) Zelnickova, P.; Faldyna, M.; Stepanova, H.; Ondracek, J.; Kovaru, F. Intracellular Cytokine Detection by Flow Cytometry in Pigs: Fixation, Permeabilization and Cell Surface Staining. Journal of immunological methods **2007,** 327, 18-29.

(97) Ji, R.; Hornung, M.; Verschuuren, M. A.; van de Laar, R.; van Eekelen, J.; Plachetka, U.; Moeller, M.; Moormann, C. Uv Enhanced Substrate Conformal Imprint Lithography (Uv-Scil) Technique for Photonic Crystals Patterning in Led Manufacturing. Microelectronic Engineering **2010,** 87, 963-967.

(98) Chou, S. Y.; Krauss, P. R.; Renstrom, P. J. Imprint of Sub‐25 Nm Vias and Trenches in Polymers. Applied Physics Letters **1995,** 67, 3114-3116.

(99) Bender, M.; Otto, M.; Hadam, B.; Vratzov, B.; Spangenberg, B.; Kurz, H. Fabrication of Nanostructures Using a Uv-Based Imprint Technique. Microelectronic Engineering **2000,** 53, 233-236.

(100) Bender, M.; Plachetka, U.; Ran, J.; Fuchs, A.; Vratzov, B.; Kurz, H.; Glinsner, T.; Lindner, F. High Resolution Lithography with Pdms Molds. Journal of Vacuum Science & Technology B **2004,** 22, 3229-3232.

(101) Wen, F.; David, S.; Checoury, X.; El Kurdi, M.; Boucaud, P. Two-Dimensional Photonic Crystals with Large Complete Photonic Band Gaps in Both Te and Tm Polarizations. Optics Express **2008,** 16, 12278-12289.

(102) Kao, C.; Osher, S.; Yablonovitch, E. Maximizing Band Gaps in Two-Dimensional Photonic Crystals by Using Level Set Methods. Applied Physics B **2005,** 81, 235-244.

(103) Mekis, A.; Chen, J.; Kurland, I.; Fan, S.; Villeneuve, P. R.; Joannopoulos, J. High Transmission through Sharp Bends in Photonic Crystal Waveguides. Physical Review Letters **1996,** 77, 3787.

(104) Soljačić, M.; Johnson, S. G.; Fan, S.; Ibanescu, M.; Ippen, E.; Joannopoulos, J. Photonic-Crystal Slow-Light Enhancement of Nonlinear Phase Sensitivity. JOSA B **2002,** 19, 2052-2059.

(105) García-Cámara, B.; Moreno, F.; González, F.; Martin, O. J. Light Scattering by an Array of Electric and Magnetic Nanoparticles. Optics Express **2010,** 18, 10001-10015.

(106) Wang, J.; Yang, L.; Boriskina, S.; Yan, B.; Reinhard, B. M. Spectroscopic Ultra-Trace Detection of Nitroaromatic Gas Vapor on Rationally Designed Two-Dimensional Nanoparticle Cluster Arrays. Analytical Chemistry **2011,** 83, 2243-2249.

(107) Lamprecht, B.; Schider, G.; Lechner, R.; Ditlbacher, H.; Krenn, J.; Leitner, A.; Aussenegg, F. Metal Nanoparticle Gratings: Influence of Dipolar Particle Interaction on the Plasmon Resonance. Physical Review Letters **2000,** 84, 4721.

(108) Alaeian, H.; Dionne, J. A. Plasmon Nanoparticle Superlattices as Optical-Frequency Magnetic Metamaterials. Optics Express **2012,** 20, 15781-15796.

(109) Gopinath, A.; Boriskina, S. V.; Feng, N.-N.; Reinhard, B. r. M.; Negro, L. D. Photonic-Plasmonic Scattering Resonances in Deterministic Aperiodic Structures. Nano Letters **2008,** 8, 2423-2431.

(110) Dallapiccola, R.; Gopinath, A.; Stellacci, F.; Dal Negro, L. Quasi-Periodic Distribution of Plasmon Modes in Two-Dimensional Fibonacci Arrays of Metal Nanoparticles. Optics Express **2008,** 16, 5544-5555.

(111) Poddubny, A. Wood Anomalies in Resonant Photonic Quasicrystals. Physical Review B **2011,** 83, 075106.

(112) Vecchi, G.; Giannini, V.; Rivas, J. G. Shaping the Fluorescent Emission by Lattice Resonances in Plasmonic Crystals of Nanoantennas. Physical Review Letters **2009,** 102, 146807.

(113) Auguie, B.; Barnes, W. L. Collective Resonances in Gold Nanoparticle Arrays. Physical Review Letters **2008,** 101, 143902.

(114) Nikitin, A. G.; Kabashin, A. V.; Dallaporta, H. Plasmonic Resonances in Diffractive Arrays of Gold Nanoantennas: Near and Far Field Effects. Optics Express **2012,** 20, 27941-27952.

(115) De Abajo, F. G. Colloquium: Light Scattering by Particle and Hole Arrays. Reviews of Modern Physics **2007,** 79, 1267.

(116) Félidj, N.; Laurent, G.; Aubard, J.; Lévi, G.; Hohenau, A.; Krenn, J.; Aussenegg, F. Grating-Induced Plasmon Mode in Gold Nanoparticle Arrays. The Journal of chemical physics **2005,** 123, 221103.

(117) Felidj, N.; Aubard, J.; Levi, G.; Krenn, J.; Hohenau, A.; Schider, G.; Leitner, A.; Aussenegg, F. Optimized Surface-Enhanced Raman Scattering on Gold Nanoparticle Arrays. Applied Physics Letters **2003,** 82, 3095-3097.

(118) Hicks, E. M.; Zou, S.; Schatz, G. C.; Spears, K. G.; Van Duyne, R. P.; Gunnarsson, L.; Rindzevicius, T.; Kasemo, B.; Käll, M. Controlling Plasmon Line Shapes through Diffractive Coupling in Linear Arrays of Cylindrical Nanoparticles Fabricated by Electron Beam Lithography. Nano Letters **2005,** 5, 1065-1070.

(119) Halas, N. J.; Lal, S.; Chang, W.-S.; Link, S.; Nordlander, P. Plasmons in Strongly Coupled Metallic Nanostructures. Chemical reviews **2011,** 111, 3913-3961.

(120) Zhou, W.; Odom, T. W. Tunable Subradiant Lattice Plasmons by out-of-Plane Dipolar Interactions. Nature nanotechnology **2011,** 6, 423-427.

(121) Galisteo-López, J.; López-García, M.; Blanco, A.; López, C. Studying Light Propagation in Self-Assembled Hybrid Photonic–Plasmonic Crystals by Fourier Microscopy. Langmuir **2012,** 28, 9174-9179.

(122) Ahn, W.; Hong, Y.; Boriskina, S. V.; Reinhard, B. M. Demonstration of Efficient on-Chip Photon Transfer in Self-Assembled Optoplasmonic Networks. ACS Nano **2013,** 7, 4470-4478.

(123) Tanemura, T.; Balram, K. C.; Ly-Gagnon, D.-S.; Wahl, P.; White, J. S.; Brongersma, M. L.; Miller, D. A. Multiple-Wavelength Focusing of Surface Plasmons with a Nonperiodic Nanoslit Coupler. Nano Letters **2011,** 11, 2693-2698.

(124) Umebayashi, T.; Yamaki, T.; Itoh, H.; Asai, K. Band Gap Narrowing of Titanium Dioxide by Sulfur Doping. Applied Physics Letters **2002,** 81, 454-456.

(125) Liu, S.; Maoz, R.; Sagiv, J. Planned Nanostructures of Colloidal Gold Via Self-Assembly on Hierarchically Assembled Organic Bilayer Template Patterns with in-Situ Generated Terminal Amino Functionality. Nano Letters **2004,** 4, 845-851.

(126) Cui, Y.; Björk, M. T.; Liddle, J. A.; Sönnichsen, C.; Boussert, B.; Alivisatos, A. P. Integration of Colloidal Nanocrystals into Lithographically Patterned Devices. Nano Letters **2004,** 4, 1093-1098.

(127) Lalander, C. H.; Zheng, Y.; Dhuey, S.; Cabrini, S.; Bach, U. DNA-Directed Self-Assembly of Gold Nanoparticles onto Nanopatterned Surfaces: Controlled Placement of Individual Nanoparticles into Regular Arrays. ACS Nano **2010,** 4, 6153-6161.

(128) Willets, K. A.; Van Duyne, R. P. Localized Surface Plasmon Resonance Spectroscopy and Sensing. Annu. Rev. Phys. Chem. **2007,** 58, 267-297.

(129) Tame, M.; McEnery, K.; Özdemir, Ş.; Lee, J.; Maier, S.; Kim, M. Quantum Plasmonics. Nature Physics **2013,** 9, 329-340.

(130) Maksymov, I. S.; Miroshnichenko, A. E. Active Control over Nanofocusing with Nanorod Plasmonic Antennas. Optics Express **2011,** 19, 5888-5894.

(131) Li, Z.; Butun, S.; Aydin, K. Touching Gold Nanoparticle Chain Based Plasmonic Antenna Arrays and Optical Metamaterials. ACS Photonics **2014,** 1, 228-234.

(132) Novotny, L.; van Hulst, N. Antennas for Light. Nature Photonics **2011,** 5, 83-90.

(133) Mühlschlegel, P.; Eisler, H.-J.; Martin, O.; Hecht, B.; Pohl, D. Resonant Optical Antennas. Science **2005,** 308, 1607-1609.

(134) Schuller, J. A.; Barnard, E. S.; Cai, W.; Jun, Y. C.; White, J. S.; Brongersma, M. L. Plasmonics for Extreme Light Concentration and Manipulation. Nature Materials **2010,** 9, 193-204.

(135) Radko, I. P.; Volkov, V. S.; Beermann, J.; Evlyukhin, A. B.; Søndergaard, T.; Boltasseva, A.; Bozhevolnyi, S. I. Plasmonic Metasurfaces for Waveguiding and Field Enhancement. Laser & Photonics Reviews **2009,** 3, 575-590.

(136) Meier, M.; Liao, P.; Wokaun, A. Enhanced Fields on Rough Surfaces: Dipolar Interactions among Particles of Sizes Exceeding the Rayleigh Limit. JOSA B **1985,** 2, 931-949.

(137) Markel, V. A. Comment on "Silver Nanoparticle Array Structures That Produce Remarkably Narrow Plasmon Line Shapes"[J. Chem. Phys. 120, 10871 (2004)]. The Journal of chemical physics **2005,** 122, 097101.

(138) Vecchi, G.; Giannini, V.; Rivas, J. G. Surface Modes in Plasmonic Crystals Induced by Diffractive Coupling of Nanoantennas. Physical Review B **2009,** 80, 201401.

(139) Zou, S.; Schatz, G. C. Response to "Comment on 'Silver Nanoparticle Array Structures That Produce Remarkable Narrow Plasmon Line Shapes' " [J. Chem. Phys.120, 10871 (2004)]. The Journal of chemical physics **2005,** 122, -.

(140) Rodriguez, S. R. K.; Abass, A.; Maes, B.; Janssen, O. T.; Vecchi, G.; Rivas, J. G. Coupling Bright and Dark Plasmonic Lattice Resonances. Physical Review X **2011,** 1, 021019.

(141) Rodriguez, S.; Rivas, J. G. Surface Lattice Resonances Strongly Coupled to Rhodamine 6g Excitons: Tuning the Plasmon-Exciton-Polariton Mass and Composition. Optics Express **2013,** 21, 27411-27421.

(142) Henson, J.; DiMaria, J.; Dimakis, E.; Moustakas, T. D.; Paiella, R. Plasmon-Enhanced Light Emission Based on Lattice Resonances of Silver Nanocylinder Arrays. Optics Letters **2012,** 37, 79-81.

(143) Väkeväinen, A.; Moerland, R. J.; Rekola, H. T.; Eskelinen, A.-P.; Martikainen, J.-P.; Kim, D.-H.; Törmä, P. Plasmonic Surface Lattice Resonances at the Strong Coupling Regime. Nano Letters **2013,** 14, 1721-1727.

(144) Khlebtsov, B. N.; Khanadeyev, V. A.; Ye, J.; Mackowski, D. W.; Borghs, G.; Khlebtsov, N. G. Coupled Plasmon Resonances in Monolayers of Metal Nanoparticles and Nanoshells. Physical Review B **2008,** 77, 035440.

(145) Bendaña, X. M.; Lozano, G.; Pirruccio, G.; Gómez Rivas, J.; García de Abajo, F. J. Excitation of Confined Modes on Particle Arrays. Optics Express **2013,** 21, 5636-5642.

(146) Chu, Y.; Schonbrun, E.; Yang, T.; Crozier, K. B. Experimental Observation of Narrow Surface Plasmon Resonances in Gold Nanoparticle Arrays. Applied Physics Letters **2008,** 93, 181108.

(147) Blake, P.; Kühne, S.; Forcherio, G. T.; Roper, D. K. Diffraction in Nanoparticle Lattices Increases Sensitivity of Localized Surface Plasmon Resonance to Refractive Index Changes. Journal of Nanophotonics **2014,** 8, 083084-083084.

(148) Jiang, Y.-W.; Tzuang, L. D.; Ye, Y.-H.; Wu, Y.-T.; Tsai, M.-W.; Chen, C.-Y.; Lee, S.-C. Effect of Wood’s Anomalies on the Profile of Extraordinary Transmission Spectra through Metal Periodic Arrays of Rectangular Subwavelength Holes with Different Aspect Ratio. Optics Express **2009,** 17, 2631-2637.

(149) Rodriguez, S.; Lozano, G.; Verschuuren, M.; Gomes, R.; Lambert, K.; De Geyter, B.; Hassinen, A.; Van Thourhout, D.; Hens, Z.; Rivas, J. G. Quantum Rod Emission Coupled to Plasmonic Lattice Resonances: A Collective Directional Source of Polarized Light. Applied Physics Letters **2012,** 100, 111103.

(150) Gao, H.; McMahon, J.; Lee, M.; Henzie, J.; Gray, S.; Schatz, G.; Odom, T. Rayleigh Anomaly-Surface Plasmon Polariton Resonances in Palladium and Gold Subwavelength Hole Arrays. Optics Express **2009,** 17, 2334-2340.

(151) Lin, L.; Yi, Y. Lattice Plasmon Resonance in Core-Shell Sio< Sub> 2</Sub>/Au Nanocylinder Arrays. Optics Letters **2014,** 39, 4823-4826.

(152) Christ, A.; Ekinci, Y.; Solak, H.; Gippius, N.; Tikhodeev, S.; Martin, O. Controlling the Fano Interference in a Plasmonic Lattice. Physical Review B **2007,** 76, 201405.

(153) Chen, T.; Pourmand, M.; Feizpour, A.; Cushman, B.; Reinhard, B. M. Tailoring Plasmon Coupling in Self-Assembled One-Dimensional Au Nanoparticle Chains through Simultaneous Control of Size and Gap Separation. The Journal of Physical Chemistry Letters **2013,** 4, 2147-2152.

(154) Omar, M. A. Elementary Solid State Physics: Principles and Applications. Addison-Wesley Reading, MA, USA:: 1975; Vol. 157.

(155) Reinhard, B. M.; Siu, M.; Agarwal, H.; Alivisatos, A. P.; Liphardt, J. Calibration of Dynamic Molecular Rule Based on Plasmon Coupling between Gold Nanoparticles. Nano Letters **2005,** 5, 2246 - 2252.

(156) Rechberger, W.; Hohenau, A.; Leitner, A.; Krenn, J. R.; Lamprecht, B.; Aussenegg, F. R. Optical Properties of Two Interacting Gold Nanoparticles. Optics Communications **2003,** 220, 137-141.

(157) Su, K. H.; Wei, Q. H.; Zhang, X.; Mock, J. J.; Smith, D. R.; Schultz, S. Interparticle Coupling Effects on Plasmon Resonances of Nanogold Particles. Nano Letters **2003,** 3, 1087-1090.

(158) Romo-Herrera, J. M.; Alvarez-Puebla, R. A.; Liz-Marzán, L. M. Controlled Assembly of Plasmonic Colloidal Nanoparticle Clusters. Nanoscale **2011,** 3, 1304-1315.

(159) Mokkapati, S.; Catchpole, K. Nanophotonic Light Trapping in Solar Cells. Journal of Applied Physics **2012,** 112, 101101.

(160) Yu, Y.; Ferry, V. E.; Alivisatos, A. P.; Cao, L. Dielectric Core–Shell Optical Antennas for Strong Solar Absorption Enhancement. Nano Letters **2012,** 12, 3674-3681.

(161) Boriskina, S. V.; Reinhard, B. M. Molding the Flow of Light on the Nanoscale: From Vortex Nanogears to Phase-Operated Plasmonic Machinery. Nanoscale **2012,** 4, 76-90.

(162) Bekshaev, A.; Bliokh, K. Y.; Soskin, M. Internal Flows and Energy Circulation in Light Beams. Journal of Optics **2011,** 13, 053001.

(163) Ahn, W.; Boriskina, S. V.; Hong, Y.; Reinhard, B. M. Electromagnetic Field Enhancement and Spectrum Shaping through Plasmonically Integrated Optical Vortices. Nano Letters **2011,** 12, 219-227.

(164) Li, K.; Stockman, M. I.; Bergman, D. J. Self-Similar Chain of Metal Nanospheres as an Efficient Nanolens. Physical Review Letters **2003,** 91, 227402.

(165) Lieb, M. A.; Zavislan, J. M.; Novotny, L. Single-Molecule Orientations Determined by Direct Emission Pattern Imaging. JOSA B **2004,** 21, 1210-1215.

(166) Novotny, L.; Hecht, B. Principles of Nano-Optics. Cambridge university press: 2012.

(167) Ureña, E. B.; Kreuzer, M. P.; Itzhakov, S.; Rigneault, H.; Quidant, R.; Oron, D.; Wenger, J. Excitation Enhancement of a Quantum Dot Coupled to a Plasmonic Antenna. Advanced Materials **2012,** 24, OP314-OP320.

(168) Aouani, H.; Mahboub, O.; Devaux, E.; Rigneault, H.; Ebbesen, T. W.; Wenger, J. Plasmonic Antennas for Directional Sorting of Fluorescence Emission. Nano Letters **2011,** 11, 2400-2406.

(169) Enoch, S.; Gralak, B.; Tayeb, G. Enhanced Emission with Angular Confinement from Photonic Crystals. Applied Physics Letters **2002,** 81, 1588-1590.

(170) Langguth, L.; Punj, D.; Wenger, J. r. m.; Koenderink, A. F. Plasmonic Band Structure Controls Single-Molecule Fluorescence. ACS Nano **2013,** 7, 8840-8848.

(171) Jun, Y. C.; Huang, K. C.; Brongersma, M. L. Plasmonic Beaming and Active Control over Fluorescent Emission. Nature communications **2011,** 2, 283.

(172) Hill, R. T.; Kozek, K. M.; Hucknall, A.; Smith, D. R.; Chilkoti, A. Nanoparticle–Film Plasmon Ruler Interrogated with Transmission Visible Spectroscopy. ACS Photonics **2014,** 1, 974-984.

(173) Mock, J. J.; Hill, R. T.; Degiron, A.; Zauscher, S.; Chilkoti, A.; Smith, D. R. Distance-Dependent Plasmon Resonant Coupling between a Gold Nanoparticle and Gold Film. Nano Letters **2008,** 8, 2245-2252.

(174) Chowdhury, M. H.; Pond, J.; Gray, S. K.; Lakowicz, J. R. Systematic Computational Study of the Effect of Silver Nanoparticle Dimers on the Coupled Emission from Nearby Fluorophores. The Journal of Physical Chemistry C **2008,** 112, 11236-11249.

CURRICULUM VITAE

[redacted]

[redacted]

[redacted]

[redacted]